Modelling of the dynamical and ozone interactions in the polar stratosphere with ICON-ART

Zur Erlangung des akademischen Grades eines

DOKTORS DER NATURWISSENSCHAFTEN

von der KIT-Fakultät für Physik des

Karlsruher Instituts für Technologie (KIT)

genehmigte

DISSERTATION

von

Shaoyin Wang

aus Luzhou

Referent:	Prof. Dr. Peter Braesicke
Korreferent:	Prof. Dr. Joaquim Pinto
Tag der mündlichen Prüfung:	25.10.2019

Abstract

Models with a well-represented stratosphere have been shown to increase the predictability on weather and climate scales through stratosphere-troposphere coupling. However, stratospheric phenomena, such as the Quasi-biennial Oscillation (QBO) or stratospheric ozone, are still poorly represented in current atmospheric models. This study characterizes and improves stratospheric simulations with the next generation weather/climate model ICON-ART, and gives insights into the dynamical and chemical (stratospheric ozone) interactions in the polar stratosphere.

The climatology of a low resolution version of ICON-ART is examined and validated against ERA-Interim data. The sub-grid scale orographic (SSO) gravity wave drag is found unconstrained in the upper stratosphere, leading to warm biases in the Northern Hemisphere (NH) winter polar stratosphere. After reducing the SSO gravity wave drag, the modelled NH polar stratosphere has a more realistic mean state. At a low resolution, the model also fails to simulate the QBO-like oscillation that is observed in the equatorial zonal wind and is dominated by easterlies.

In order to explore dynamical interactions between the stratospheric zonal winds in the tropics and the polar stratosphere, a QBO-like oscillation is imposed in ICON by relaxation using ERA-Interim winds (QBO-relaxation). Then, the Holton-Tan relationship, a phenomenon in which equatorial zonal winds synchronize with the NH winter polar stratosphere, is generally reproduced in the QBO-relaxation simulations. Based on idealized experiments, I found that the polar stratosphere is sensitive to the QBO phases and to relaxation height ranges. When the modelled equatorial zonal wind in the upper stratosphere is relaxed towards ERA-Interim, it results in (1) a colder NH polar stratosphere, for which the modulation of planetary wave meridional propagation is responsible, and (2) a Holton-Tan relationship where the timing depends on the relaxation depth.

Furthermore, two stratospheric ozone representations in ICON-ART are compared: (1) interactive-ozone considers ozone-meteorology coupling and (2) non-interactive-ozone uses the climatological ozone of the interactive-ozone simulation. Climatological ozone is a default in many climate models. When ozone is calculated interactively, the model simulated a colder

polar stratosphere with a delayed polar vortex breakup in the Southern Hemisphere. Depending on the background zonal wind, planetary waves are found to feedback onto the changes in the polar stratospheric temperature either negatively or positively.

Contents

List of Figures

List of Tables

List of Abbreviations

ICON-ART	ICOsahedral Non-hydrostatic [weather and climate model] - Aerosols and Reactive Trace gases
BDC	Brewer-Dobson Circulation
TEM	Transformed Eulerian Mean
QBO	Quasi-biennial Oscillation
SSW	Sudden Stratospheric Warming
SAO	Semi-annual Oscillation
AMIP	Atmospheric Model Intercomparison Project
ERA-I	ERA-Interim
ECMWF	European Centre for Medium-Range Weather Forecasts
EPFD	Eliassem-Palm flux divergence
GWD	gravity wave drag
SSO	Subgrid-scale orographic
NONGWD	non-orographic gravity wave drag
ZMZW	zonal mean zonal wind
ENSO	El Niño and Southern Oscillation
HT relationship	Holton-Tan relationship
Linoz	Linearized ozone scheme
Fz	Vertical component of Eliassen-Palm flux
Fy or Fphi	Meridional component of Eliassen-Palm flux

Chapter 1 Introduction

The stratosphere is a layer above the tropopause that only contains approximately 20% of the atmospheric mass. Now, it is widely accepted that the stratosphere is dynamically coupled with the troposphere, which provides an important additional source of predictability for weather and climate simulation. Thus, it is important to understand the variability in the stratosphere. Figure 1.1 highlights some important factors and processes that are relevant to stratospheric variability and coupling between the stratosphere and the troposphere, including the tropical quasi-biennial oscillation (QBO) and semi-annual oscillation (SAO), stratospheric ozone, polar vortex dynamics, planetary-scale Rossby waves (hereafter, in short planetary waves and PWs) and gravity waves (GWs). The role of polar stratosphere is mostly emphasized on the coupling between the stratosphere and the troposphere in the extra-tropics (Figure 1.1, green area).

1.1 Variability in the polar stratosphere

During the winter, due to a lack of sunlight in the polar stratosphere, the temperature contrast between the midlatitudes and the pole is very large, which leads to a strong westerly polar vortex. When the sunlight returns during the spring, the polar vortex gradually breaks up and the westerly winds become weak easterlies (Waugh et al. 2016). The polar vortex has large variability on a range of timescales. An extreme case of variability is a sudden stratospheric warming (SSW) with rapid temperature increases by 10–50 K within a few days, which can be initiated by vertically propagating planetary waves. The SSW, accompanied by polar vortex displacement or split, can link down to the surface, subsequently leading to strong cold air outbreaks (Mitchell et al. 2013). Therefore, a better understanding of the variability in the polar stratosphere is enormously helpful not only for medium-range weather forecasts, but also for long-term climate change projections (Kidston et al. 2015).

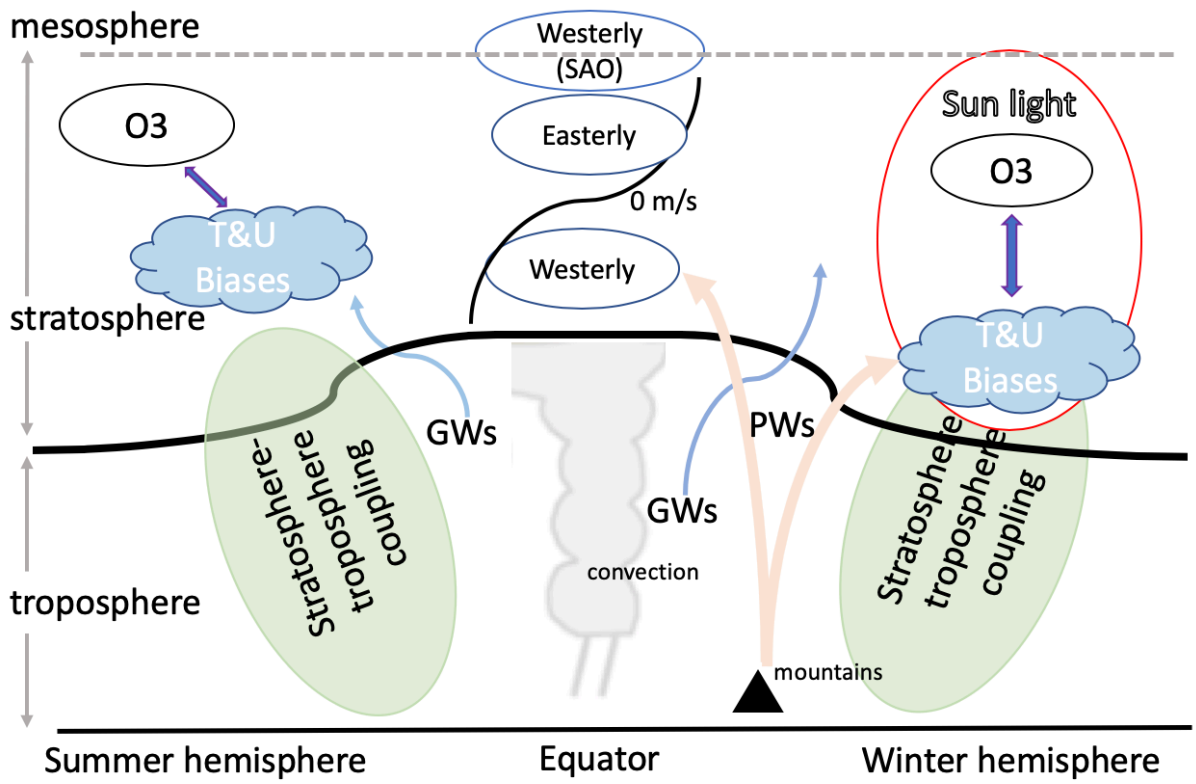

Figure 1.1– Schematic illustrating the factors and processes that are important for polar stratospheric variability (a particular phase of SAO and QBO is shown). The term GWs denote gravity waves; PWs denote planetary waves; SAO denotes semi-annual oscillation. The zero-wind line related to the QBO phase services as a waveguide of PWs (presuming westerly phase of QBO in the lower stratosphere). Because GWs play a key role in the middle atmosphere through wave dissipation and deposition, how GWs are represented in the climate models is relevant to the model bias. Another important factor is stratospheric ozone, which is coupled to meteorology. Furthermore, the variability in the polar stratosphere has a significant impact on the surface weather and climate via stratosphere-troposphere coupling (Kidston et al. 2015).

As shown in Figure 1.1, variability in the polar stratosphere is influenced by various factors and processes in the climate system. Here, several factors and pathways are listed below.

1. The tropospheric PWs, which vertically propagate into the stratosphere and break (wave forcing), largely drive the variability in the stratosphere (Figure 1.1, brown vector). The Northern Hemisphere (NH) has more planetary wave activities than the Southern Hemisphere (SH), because of the larger topographic and land-sea contrast in the NH. As a consequence, the NH polar vortex exhibits far stronger variability than its SH counterpart. This also includes more SSW events in the NH than the SH (on average once every two years vs. only once, in September 2002) (Waugh et al. 2016).

2. Tropical variability (QBO and SAO) – alternating persistent (zonal mean zonal wind) wind regimes – are important for planetary waves propagation and thus for the dynamics of the polar stratosphere. Planetary waves propagate upward and either equatorward or poleward. Prevailing winds can act like a switch to guide the wave propagation (Figure 1.1, 0 m/s), thus influencing the temporal behaviour of the spectrum of variability.
3. Stratospheric ozone determines important aspects of the vertical temperature structure of the atmosphere. The stratospheric ozone is coupled with the atmospheric dynamics by radiative and chemical processes (Figure 1.1, red circle).
4. GWs are small-scale atmospheric waves and generated by different sources (e.g., mountains and convection). As the waves propagate upward and dissipate, they force the atmospheric circulation at the level of the stratosphere and the mesosphere (Figure 1.1, blue vector).

1.2 Research tasks

The atmospheric circulation is extraordinarily complex, comprising many interactions and feedback processes (Figure 1.1). General circulation models (GCMs) provide essential tools to understand different interactions and feedback processes. Basically, the GCMs use finite numerical discrete method to approximate the continuous governing differential equations (i.e., Navier-Stokes equations), and are supplemented by subgrid-scale parameterizations. However, the models are often biased in mean state or variability, especially for stratospheric (or middle) circulations. For example, only few models can simulate QBO-like oscillation. Therefore, we develop and apply atmospheric models of ever-increasing complexity. The inclusion of the complexity may lead to a prominent improvement of weather forecasts and climate predictions. Here, a particular model (ICON/ICON-ART) is investigated to assess its potential for improvements. This model provides a seamless framework for forecasts on weather (weather: initial value problem) and climate scales as well (climate: boundary value problem).

In this study, I will focus on the potential role of stratospheric phenomena and stratospheric ozone as some elements that are important for seasonal forecasts, and examine systematic weaknesses and offer potential fixes for stratospheric simulation in ICON/ICON-ART.

1.3 Structure of the thesis

The thesis uses the chemistry-climate model ICON/ICON-ART to investigate how the tropical stratospheric zonal winds and stratospheric ozone interact with the polar stratosphere. The research tasks include: 1), characterization and rectification of model biases, especially in the stratosphere; 2), the influence of tropical variability (QBO and SAO) on the polar stratosphere; 3), the influence of ozone-meteorology coupling on the polar stratosphere.

In Chapter 2, I briefly describe the basic atmospheric structure and dynamics that are relevant to the (polar) stratosphere.

In Chapter 3, I present the model description for ICON/ICON-ART and the experimental integration strategies.

In Chapter 4, model biases in ICON/ICON-ART are characterized and rectified.

In Chapter 5, using ICON/ICON-ART, dynamical interactions between low latitudes and high latitudes are investigated (limited to the QBO).

In Chapter 6, using ICON/ICON-ART, the influence of stratospheric ozone-meteorology coupling on regional and global circulations are investigated.

Finally, in Chapter 7, major findings are summarized and plans for future work are presented.

Chapter 2 Research background

As shown previously in Figure 1.1, the polar stratosphere is dynamically and chemically coupled with various factors and processes. A better understanding of the complex interactions may improve our simulation of the polar stratospheric variability and finally contribute to improving forecasts of surface weather and climate.

This chapter will provide an overview of the coupling processes associated with the stratosphere and how these processes are presented in atmospheric models. In this regard, firstly, I will describe the general structure of the atmosphere in Section 2.1. Afterwards elements of the variability, in particular the interannual variability, are explained. This will be followed by a description of wave phenomena and their linkages to the atmospheric variability on different time scales in Section 2.2. Finally, since a chemistry-climate model (ICON/ICON-ART) is used to investigate the coupling processes in the stratosphere, the existing challenges of stratospheric modelling are introduced in Section 2.3.

2.1 Overview of atmospheric structure and stratospheric circulation

2.1.1 Vertical structure

The atmosphere is divided into several layers according to temperature profile (Figure 2.1). The troposphere is characterized by temperatures decreasing with height, whereas temperatures are increasing with height in the stratosphere. The temperature increase with height in the stratosphere is due to the absorption of solar radiation by stratospheric ozone. Generally, the stratosphere is dynamically more stable than the troposphere, where weather processes prevail. However, the atmospheric waves (e.g., gravity waves) that vertically propagate from the

troposphere into the stratosphere largely drive the stratospheric circulation out of radiative equilibrium.

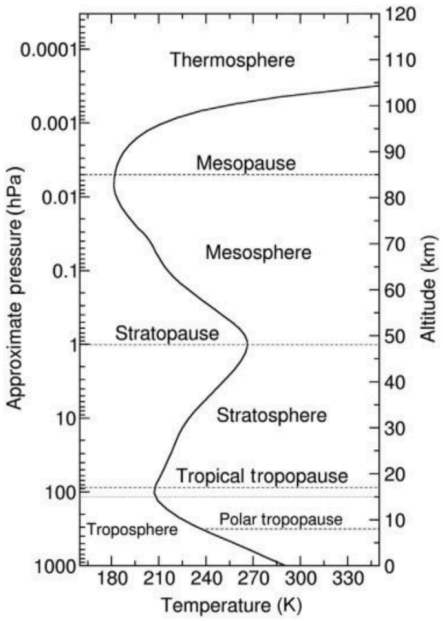

Figure 2.1– Atmospheric layers: temperature profile as a function of pressure/altitude (from North et al. (2014, vol. 4, P. 50)). The tropopause height varies with the latitude.

2.1.2 Seasonal and zonal mean structure

Figure 2.2 shows the summertime (June–August) and wintertime (December–February) zonal mean zonal wind and temperature cross-section. Two strong westerly jets characterize the winter hemisphere: (a) a tropospheric jet at subtropical regions, which is just below the stratosphere and (b) a polar stratospheric westerly jet. A weaker tropospheric westerly jet and a strong stratospheric easterly jet characterize the summer hemisphere. The stratospheric westerly jet is coherent with the seasonal temperature changes. With the onset of winter, the Sun light moves away from the polar stratosphere, which creates strong temperature gradient between the polar-latitudes and tropical-latitudes. According to the thermal wind equation, this results in westerly acceleration with height. The thermal wind equation is formulated as follows,

$$\frac{\partial u_g}{\partial \ln p} = \frac{R}{f}\left(\frac{\partial T}{\partial y}\right) \text{ and } \frac{\partial v_g}{\partial \ln p} = -\frac{R}{f}\left(\frac{\partial T}{\partial x}\right),$$

where u_g and v_g are the geostrophic wind; R, f and p are gas constant, Coriolis parameter and pressure. From the thermal wind equation, the vertical shear of large-scale zonal wind is directly proportional to a meridional temperature gradient. Figure 2.3 (zonal mean temperature, June–August) clearly illustrates the strong temperature contrast between the cold polar stratosphere and warm tropical stratosphere, which leads to the strong polar night jet during June–August. Due to the larger orographic (e.g., the Himalayas and the Rockies) effect and land-sea contrast in the NH, stronger stationary wave activities are found in the NH, leading to a weaker polar stratospheric westerly jet in the NH than its SH counterpart (Figure 2.2 first row); and a warmer polar stratosphere as well (Figure 2.2 second row).

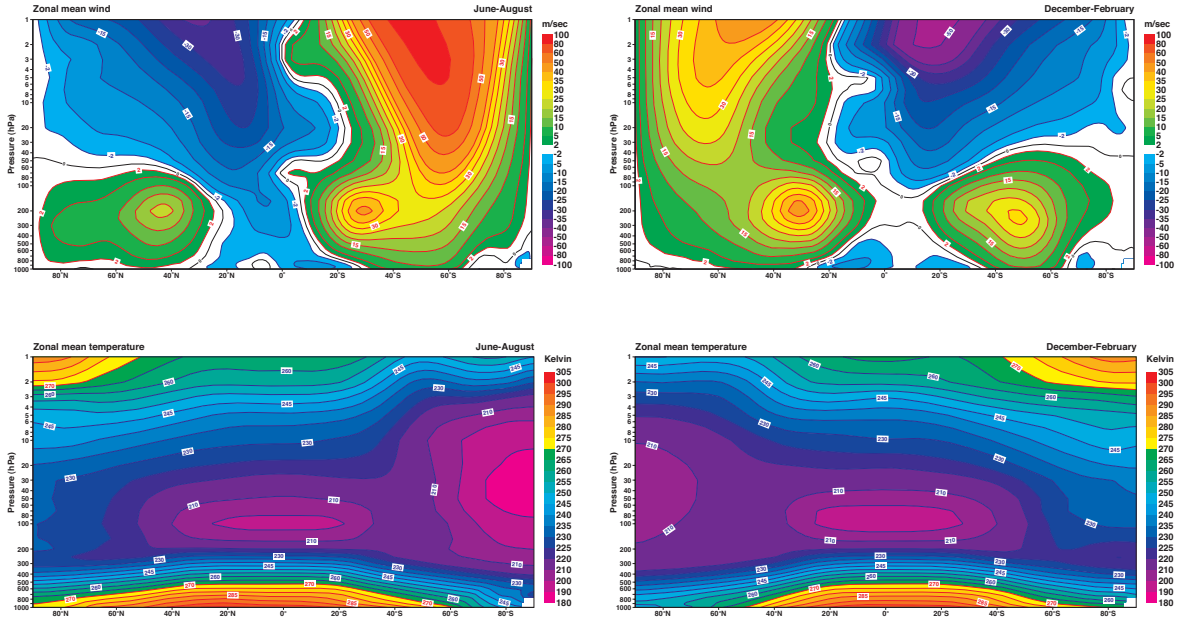

Figure 2.2– Zonal mean zonal wind and zonal mean temperature climatology for summer (June–August) and winter (December–February) (source from https://software.ecmwf.int/static/ERA-40_Atlas/docs/index.html). The left panel is June–August average; the right panel is December–February average.

2.1.3 Tropical variability: the QBO and SAO

Figure 2.3 presents time-height cross-section of monthly-mean equatorial zonal mean zonal wind. The equatorial stratospheric zonal wind (15–30 km, or about 70–0.3 hPa) is dominated by alternating easterlies and westerlies, with an average period about 28 months (Figure 2.3a). This phenomenon is known as the quasi-biennial oscillation (QBO). Above the QBO level, the semi-annual oscillation (SAO) is the most prominent, which extends from about 10 hPa to 0.1

hPa (Figure 2.3b). The QBO amplitude is approximately symmetric around the equator extending from 15° S to 15° N (Figure 2.4a), and the half width of the latitudinal range is approximately 12° (Baldwin et al. 2001).

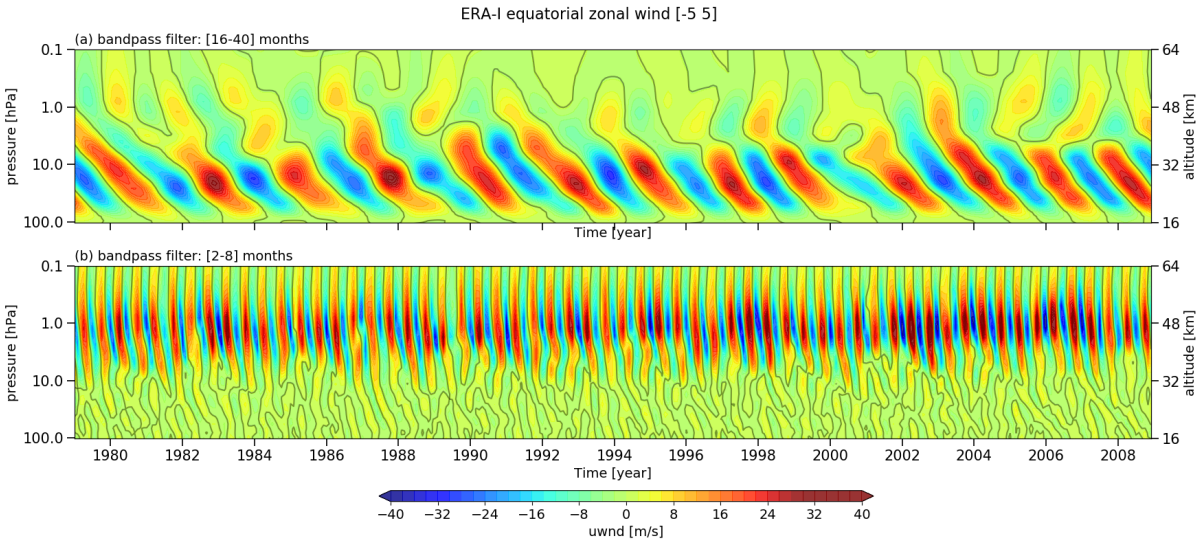

Figure 2.3– Time-height cross-sections of ERA-I equatorial zonal wind [5° S–5° N] for 1979–2008. The bandpass filter is applied to original equatorial zonal wind to isolate the QBO and SAO variability, with (a) bandpass filter of 16–40 months and (b) bandpass filter of 2–8 months. The contours mark zero-wind speed.

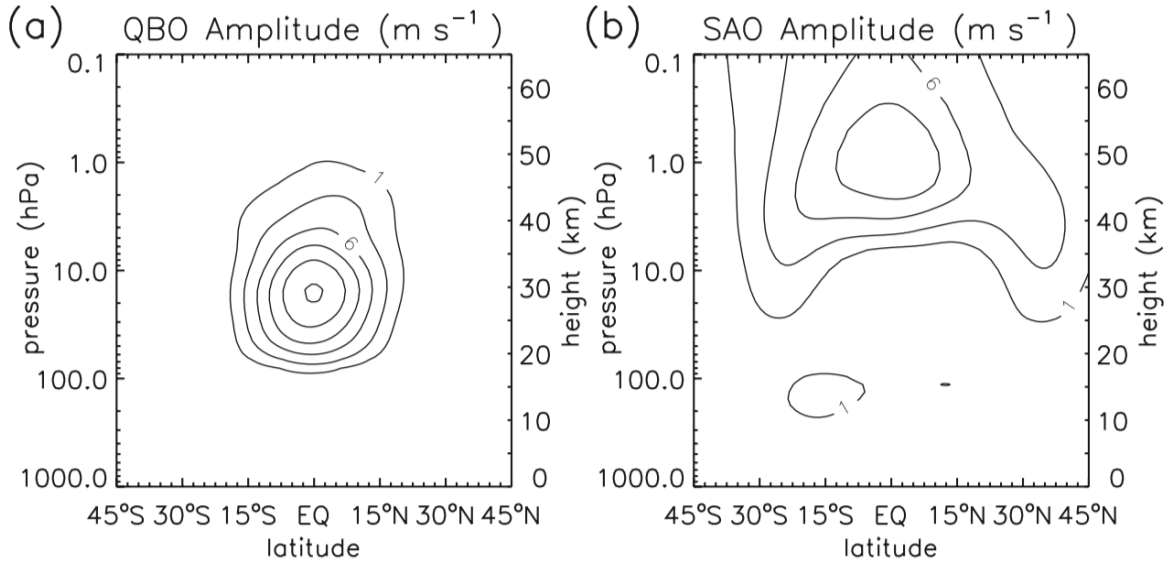

Figure 2.4– Amplitude of the QBO and SAO (source from Gallagher et al. (2010, P. 93), which is calculated using Fourier analysis of the zonal mean zonal wind after applying bandpass filtering. (a) The QBO amplitude is based on QBO harmonics 13–24 (22–40 months) and (b) the SAO amplitude is based on SAO harmonics 86–90 (~6 months) (see Pascoe et al. (2005)).

The QBO is characterised by repeating wind patterns, i.e., westerly to easterly at given height. The phase transition is often initiated at upper stratospheric levels. For example, the upper westerly winds are descending to the lower stratosphere, while upper westerly winds are turning into easterly. The wind speed of the easterlies is stronger than of westerlies, and the easterly phase is generally descending slower than the westerly phase. The phase transition is also weakly synchronized with seasonal cycle, e.g., onset of westerly or easterly wind patterns at 50 hPa occurs mainly during North Hemisphere late spring. The QBO is unique for its nearly 2-year oscillation, and the extra-tropical planetary waves and latent heating cannot explain the QBO. The theoretical explanation has been available from the pioneering works (Booker and Bretherton 1967; Lindzen and Holton 1968; Holton and Lindzen 1972; Lindzen 1987). Some fundamental theoretical concepts are also illuminated in a rotating tank by Plumb and McEwan (1978). A more detailed description of QBO structure and theoretical explanation could be found in Baldwin et al. (2001).

The SAO has a period of approximately 6 months and is clearly phase locked with the annual cycle. The SAO amplitude is also symmetric about the equator, but with a broader extension from about 30º S to 30º N (Figure 2.4b).

2.1.4 Vertical propagation of planetary waves

Planetary waves (PWs) or Rossby waves (named after C.G. Rossby), e.g., as described by geopotential height perturbations around a longitude circle, are forced by zonal asymmetries of (bottom) boundary conditions (e.g., land-sea contrasts and large mountains). Their vertical propagation and momentum deposition associated with wave breaking makes large contributions to the stratospheric (and mesospheric) temporal and spatial variability. For example, the Sudden stratospheric warmings (SSWs) are commonly initiated by the increased amplitude of upward propagating PWs. The PWs together with gravity waves are also believed to be the primary forcings of the Brewer-Dobson circulation (BDC) (Butchart 2014). The BDC acts to redistribute long-lived trace gases in the meridional and vertical direction, e.g., causing distinct methane (CH_4) gradients.

The vertical propagating PWs are filtered when they travel into the stratosphere from their tropospheric sources. According to Charney and Drazin (1961) (Charney-Drazin) theory, the theoretical explanation is formulated as

$$0 < \bar{u} - \mathrm{c} < \frac{\beta}{(k^2+l^2)+\frac{\mathrm{f}}{4H^2N^2}},$$

$$u_c = \frac{\beta}{(k^2+l^2)+\frac{\mathrm{f}}{4H^2N^2}},$$

with $\beta = 2\Omega\cos(\varphi)$ and $\mathrm{f} = 2\Omega\sin(\varphi)$ (Ω and φ are the Earth's rotation rate and latitude). H, N and $\bar{u}$ are the scale height, buoyancy frequency and background flow (zonal mean zonal wind). c, l and k are wave phase speed, meridional and zonal wave number. u_c is referred to as the critical Rossby velocity and is inversely proportional to zonal and meridional wave number ($k^2$and l^2). For stationary waves ($c = 0$), the vertical propagation of stationary PWs is favoured when the zonal wave number is small (typically zonal wave number 1–3) and the basic flow is weak westerly. For large wave number ($k > 3$), e.g., synoptic weather disturbances, the critical Rossby velocity is very small and the wave is trapped in the lower troposphere. As the wave propagation also depends on the background flow, Figure 2.5 (from Salby 2012, P. 453) illustrates two rays of stationary waves are propagating from the troposphere into the stratosphere:

- when the planetary wave encounters the polar night jet (turning level) (ray 1), this wave is reflected or refracted towards the equator.
- when the planetary wave approaches the zero-wind line (critical level) (ray 2), wave propagation is stalled, which is associated with wave absorption.

The two rays illustrate that the planetary wave propagation depends on background zonal wind. In the summer hemisphere, stationary planetary waves are trapped vertically because the zonal winds in the stratosphere are easterlies. In the winter hemisphere, stationary planetary waves are reflected or refracted towards the equator, if the polar stratospheric jets are very strong.

Except for background zonal wind, the vertical shear of zonal wind and atmospheric stability also play a role in controlling planetary wave propagation. A more general consideration is refractive index ($n_k^2(\varphi, z)$) (Andrews et al. 1987), which is defined by

$$n_k^2(\varphi, z) = \frac{1}{\bar{u}}\frac{\partial \bar{q}}{\partial \varphi} - \left(\frac{k}{a\cos\varphi}\right)^2 - \left(\frac{f}{2NH}\right)^2$$

where

$$\frac{\partial \bar{q}}{\partial \varphi} = \frac{2\Omega}{a} cos\varphi - \frac{1}{a^2}\frac{\partial}{\partial \varphi}\left[\frac{1}{cos\varphi}\frac{\partial}{\partial \varphi}(\bar{u}\cos\varphi)\right] - \frac{f^2}{\rho_0}\frac{\partial}{\partial z}\left(\frac{\rho_0}{N^2}\frac{\partial \bar{u}}{\partial z}\right) .$$

The $\frac{\partial \bar{q}}{\partial \varphi}$ is meridional gradient of zonal mean potential vorticity and ρ_0 is air density. The refractive index is used to diagnose planetary wave propagation: planetary waves tend to propagate towards positive $n_k^2(\varphi, z)$ and are refracted from regions where $n_k^2(\varphi, z) < 0$. It can be seen that $n_k^2(\varphi, z)$ depends on buoyancy frequency (N^2) and vertical shear of zonal wind ($\frac{\partial \bar{u}}{\partial z}$). When $\bar{u}$ and N^2 are constant, the refractive index is simplified to Charney-Drazin theory (Gallagher et al. 2010, P. 36).

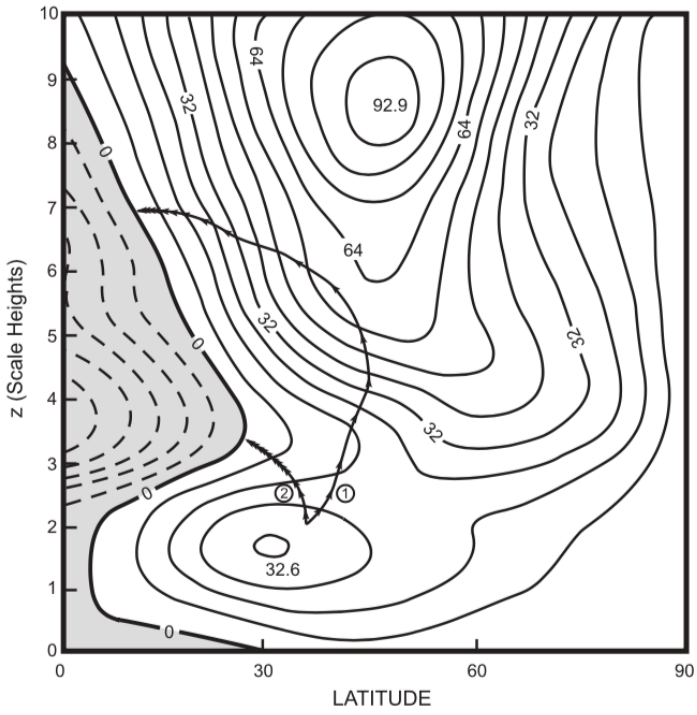

Figure 2.5– Illustration of vertical propagation of planetary waves (source from Salby (2012, P. 453)). Two stationary wave rays are propagating from the troposphere into the lower stratosphere.

2.1.5 Stratospheric ozone and ozone climate interactions

Ozone is produced in the stratosphere as a consequence of photochemical reactions. When molecules of oxygen (O_2) are broken down by photos (sufficient high energetic solar radiation), it results in two atomic oxygen (O) (a process which is called photolysis). Then, a free atomic oxygen reacts with oxygen to form ozone (O_3). On the one hand, ozone is an important absorber of Sun light in ultraviolet (UV) and infrared (IR) bands. This determines important aspects of

the vertical temperature structure of the atmosphere. On the other hand, ozone and meteorology are involved in a two-way coupling.

Firstly, the changes in both the temperature and atmospheric circulation significantly influence ozone concentration. The temperature change in the upper stratosphere affect the chemical reaction rate, and in the lower polar stratosphere, it affects the formation of polar stratospheric clouds (PSCs), which is responsible for Antarctic ozone hole in austral spring by providing surfaces for heterogeneous reactions. The atmospheric dynamics, such as BDC, redistribute the ozone from its tropical sources to extra-tropical sinks.

Secondly, the change of stratospheric ozone also feeds back onto the circulation. As a key absorber of Sun light, the stratospheric ozone changes lead to the changes of local radiative balance, therefore, the changes in temperature and circulation. For example, by comparing the Antarctic ozone hole with and without chlorine activation on PSCs, Keeble et al. (2014) found with > 75% of ozone destroyed at 50 hPa in chlorine activation run, this ozone destruction results in a > 12 K cooling of the lower polar stratosphere (as a result of decreased shortwave heating), which subsequently leads to a stronger polar night jet via the changes of temperature gradient. Due to the dynamical coupling between the stratosphere and the troposphere (in winter/spring), any changes in the stratosphere (particularly polar stratosphere) finally lead to downward influences on tropospheric circulation and the surface climate. Keeble et al. (2014) found that in December, stratospheric ozone depletion causes surface pressure dipole anomaly with positive values in the high latitudes (poleward of ~60° S), and negative values in the mid-latitudes (from 60° to 30° S), which resembles a positive phase of the SH annular model (SAM). Now, it has been widely accepted that the Antarctic ozone hole has played a key role in driving recent SH climate change (Son et al. 2009; Thompson et al. 2011).

2.2 Dynamical and chemical interactions in the polar stratosphere

The representation of the equatorial zonal wind oscillations (QBO and SAO), stratospheric chemistry and gravity wave drag in GCMs are directly linked to the modelled climatology and variability of the polar stratosphere. Therefore, the improvement of the individual process also

leads to an improved model performance. Here, the dynamical and chemical interactions with the polar stratosphere are introduced.

2.2.1 Extratropical effects of the QBO and upper stratosphere (or SAO)

The equatorial QBO not only dominates the tropical stratospheric variability in temperature and trace gases (see https://acd-ext.gsfc.nasa.gov/Data_services/met/qbo), but also considerably contributes to the interannual variability at high-latitudes. The equatorial westerlies (easterlies) at 50 hPa correlate with a stronger (weaker) polar vortex (Holton and Tan 1980, 1982, hereafter HT80), which is commonly referred to as Holton-Tan (HT) relationship. The HT relationship has been simulated by atmospheric models with internally generated QBO or imposed QBO, suggesting the HT relationship does not rely on the QBO generating method.

The HT relationship is commonly explained by the modulation of planetary wave propagation and activity. As shown in Figure 2.6, the zero-wind line is the critical line for stationary planetary waves (wave absorption and dissipation near the zero-wind line) and its position is affected by the QBO. The westerly (easterly) phase of QBO (e.g., defined at 50 hPa as a typical level) yields poleward (equatorward) displacement of zero-wind line (Figure 2.6 at scale height around 3–4, subtropical critical line). This corresponds to more or less planetary wave forcing in the polar stratosphere. The mechanism was firstly suggested in HT80, where they emphasized the modulation of the critical line at lower stratospheric altitudes. However, due to the non-linear interactions between wave and mean-flow (planetary waves and critical line), this mechanism is still not well understood in detail.

The HT relationship is most pronounced in the NH winter, coinciding with the favourable conditions for upward planetary wave propagation into the stratosphere. The HT relationship also displays seasonal change through the winter. In the HT80, they divided the winter into early and late winter, and found contrasting behaviour for wavenumber-1 and -2 amplitudes. Wavenumber-1 amplitude is stronger in early winter for easterly phase of QBO, while wavenumber-2 amplitude is stronger in late winter for westerly phase of QBO. By extending observation records (Hu and Tung 2002; Lu et al. 2008), the HT relationship is found most significant during early winter and weaker in late winter, which is suggested to be affected by non-linear effect, such as SSWs.

The HT relationship does not always hold. Using 49-year ERA-40, Lu et al. (2008) found decadal-scale weakening of HT relationship during 1977–1997, which is attributed to the changes in planetary wave forcing. Using 10.7 cm Solar flux, Labitzke (1987) found that the HT relationship only holds during solar minimum, and is reversed during solar maximum, and the result is further confirmed by extending data records (Labitzke et al. 2006). Other factors such as ENSO, volcanic eruptions are also believed to influence the HT relationship (Baldwin et al. 2001).

The upper stratosphere (or SAO) is dynamically connected with the QBO as well as 11-yr Solar cycle. The influence of equatorial zonal winds in the upper stratosphere has been emphasized in a series of studies of (Gray et al. 2001b,a). Based on data study, Gray et al. (2001b) found a greater sensitivity of polar temperatures to equatorial wind distributions in the region of the stratopause (–50 km) than in the lower-stratospheric region (–25 km). By using stratosphere-mesosphere model with perpetual January conditions (Gray et al. 2001a), they found only when the equatorial zonal wind is relaxed towards rocketsonde data over the extended height range 16–58 km, a realistic Holton-Tan relationship is reproduced. Conversely, there is no HT relationship when the equatorial zonal wind is relaxed towards the data in the height range 16–32 km. Considering the seasonal variation, the studies (Gray 2003; Gray et al. 2004; Pascoe et al. 2005) suggest that during the early winter, the lower stratospheric QBO is the most influential for the polar stratosphere, but later in the winter when the wave-mean flow interactions are strongly non-linear (effect of wave breaking on the mean flow), the greatest influence may come from the equatorial upper winds (SAO). Using full troposphere-stratosphere-mesosphere global model, Pascoe et al. (2006) examined the sensitivity of polar stratosphere to the imposed equatorial zonal wind height range (QBO and SAO) by relaxation, and suggested that the QBO in the lower equatorial stratosphere influences early winter polar variability, whereas the QBO and SAO in the upper equatorial stratosphere together influence midwinter polar variability. However, due to the idealized experiments that are applied, a comparison with observational record is hard. A recent review of high latitude influences of QBO is given by Anstey and Shepherd (2014).

2.2.2 Influences of interactive ozone as compared to non-interactive ozone

Because ozone and meteorology are coupled by dynamics, radiation and chemistry on different temporal and spatial scales, a realistic simulation of these couplings is critical for predictions

of global as well as regional climate variability. However, zonal and monthly mean ozone is commonly used for radiative calculation in most of the climate simulations (Eyring et al. 2013), where some of the ozone variabilities are neglected, such as zonal asymmetries and temporal variability below one month. Using linear interpolation of monthly ozone to the model time step, Neely et al. (2014) found that this induces significant biases in modelled seasonal variation of Antarctic ozone and temperature. The zonally asymmetric ozone (ZAO) is correlated with dynamical asymmetries (planetary waves) (Zhang et al. 2019). When prescribing zonal mean ozone in climate models, it ignores ozone asymmetries. Modelling studies found that inclusion of ZAO, it leads to a warmer polar stratosphere as well as higher frequency of SSWs of NH (Gillett et al. 2009; Peters et al. 2015), and colder and stronger polar vortex of SH (Crook et al. 2008; Waugh et al. 2009a). Using a wave-mean flow interaction model, Albers and Nathan (2011) proposed two pathways to explain the impacts of ZAO on the vortex: 1) modulation of planetary wave and 2) modulation of wave-ozone flux convergences. The two pathways are displayed and examined in a chemistry-climate model (Rae et al. 2019).

By directly comparing with and without interactively ozone calculation, Haase and Matthes (2018) identified a negative feedback between lower stratospheric ozone and vertical propagation of planetary waves during the NH polar vortex breakdown: a decrease of ozone is linked to an increase of polar night jet, which further leads to the increase of vertical wave propagation and dynamical heating as well as BDC. This negative feedback loop in interactive chemistry simulation is associated with a significantly stronger and colder polar night jet (PNJ) during spring. Similarly, on the SH, using Goddard Earth Observing System Model in two sets of transient simulations of 1960–2010, Li et al. (2016) found interactive chemistry causes stronger Antarctic lower stratosphere cooling and circumpolar westerly acceleration during November–January and through the stratosphere–troposphere coupling, this correlates with significantly stronger wind stress, leading to a stronger ocean warming and enhanced Antarctic sea ice decrease.

The interactive ozone also plays an important damping effect on the climate response to the anthropogenic increase of greenhouse gases. Under the 4xCO2 forcing, it is found that the poleward shift of SH midlatitude jet is significantly reduced (by 20%) as well as the number of extreme ENSO events, when interactive ozone is included (Chiodo and Polvani 2017a; Nowack et al. 2017). The damping effect is also shown at the global surface temperate. When

neglecting the ozone feedback effect under climate change, it leads to ~20% increased global warming for a four times CO_2 increase (Nowack et al. 2015).

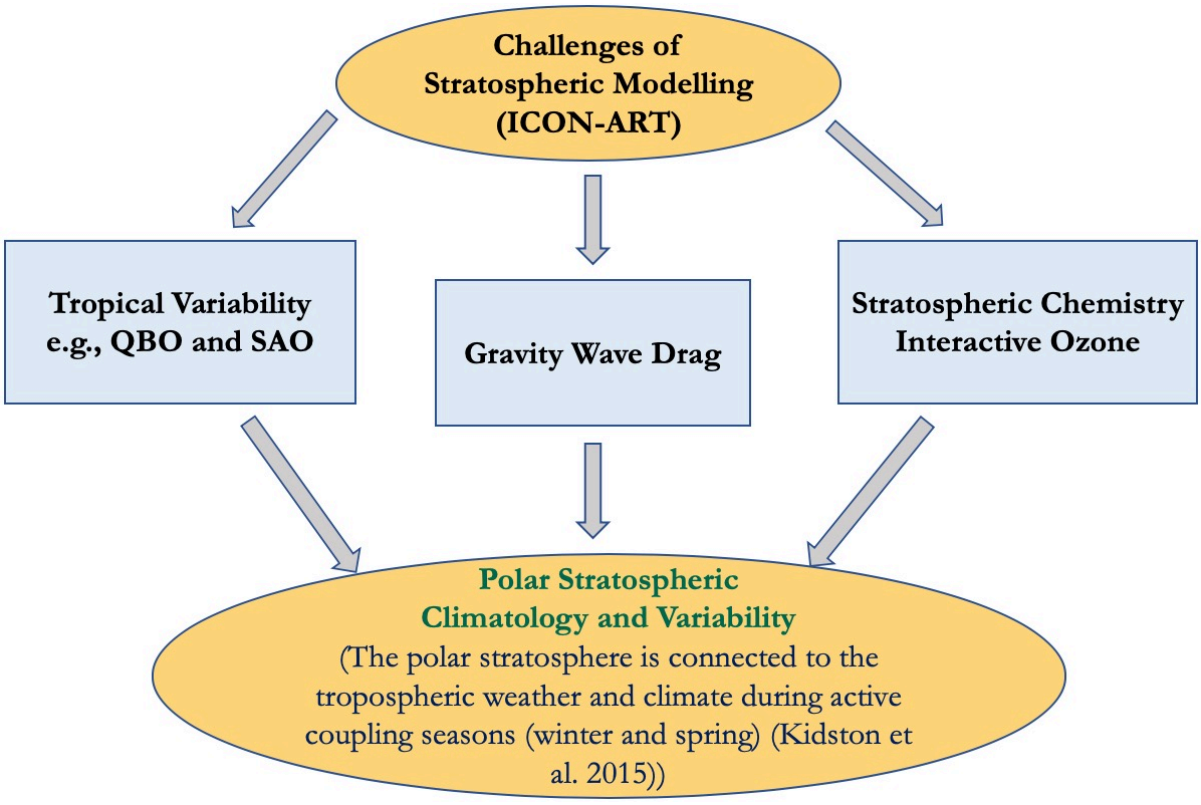

Figure 2.6– Schematic illustration of the existing challenges of stratospheric modelling.

2.3 Challenges of stratospheric modelling

For long-term climate simulation, coarse model resolutions with several subgrid-scale physical parametrizations are often used. This is due to the high computational cost of using high resolution model. For example, by comparing a high resolution Earth System Model of the Max Planck Institute (MPI-ESM-HR) (~100 km, 95 layers) with a low one (MPI-ESM-LR) (~200 km, 47 layers), Müller et al. (2018) found that the MPI-ESM-HR has a throughput of ~15 model years per day as compared to ~50 model years per day for MPI-ESM-LR, meanwhile the MPI-ESM-HR uses 106 nodes (each 36 cores) as compared to only 16 nodes for MPI-ESM-LR. Therefore, it is inevitable that the coarse resolution models suffer from some significant biases, which are potentially improved in high-resolution model simulation. For my stratospheric modelling approach, Figure 2.6 summarizes three aspects of challenges that are relevant to my research – polar stratospheric climatology and variability.

2.3.1 Gravity wave drag

Small-scale gravity waves are generated from different sources in the troposphere, such as flow over mountains and convection processes. The restoring force for gravity wave is provided by buoyancy. As gravity waves propagate vertically into the stratosphere, they are dissipated and deposit momentum into the mean flow. The wave drag arising from gravity wave dissipation plays a key role in driving atmospheric circulation like BDC. Therefore, it is necessary to take account of their dynamical effects in stratosphere-resolving models. While the large-scale planetary waves are well resolved in coarse climate models, the small-scale gravity wave cannot be resolved on the grid and so the effect of small-scale waves on the mean flow is parameterised (formulated as a drag). The gravity wave drag (GWD) parameterizations are generally grouped into (1) subgrid-scale orographic (SSO) gravity wave drag and (2) non-orographic gravity wave drag (NONGWD). However, the gravity wave drag parameterizations are poorly constrained by observations, which leads to large uncertainties on stratospheric simulations. Both SSO and NONGWD parameterizations contain some tuneable parameters to adjust gravity wave drag (e.g., launch height and amplitude). A simple rule of thumb of tuning is to get a better representation of QBO or polar stratospheric climatology (smaller temperature bias). It remains one of largest uncertainty on the stratospheric (or middle atmosphere) simulations. A recent review of GWD parameterization is given by Alexander et al. (2010).

2.3.2 Model simulations of tropical OBO and SAO

The theoretical explanation of the QBO has been available for many years (Lindzen and Holton 1968; Holton and Lindzen 1972), which suggested both the tropical large-scale waves (mixed Rossby gravity waves and Kelvin waves) and small-scale gravity waves could drive the QBO-like oscillation. However, modelling a realistic QBO remains a great challenge for many numerical models (Butchart et al. 2018). It is shown that among 47 models participating the Coupled Model Intercomparison Project 5 (CMIP5), only five models spontaneously produce the QBO-like behaviour. The QBO is believed to be driven by vertically propagating atmospheric waves which deposit easterly and westerly momentum. A continuous spectrum of large-scale equatorial waves and small-scale gravity waves transports the momentum necessary to force the QBO-like oscillation. According to some model experiments with successful simulations of QBO-like oscillation, some general prerequisites are: (1) a proper tuning of non-

orographic gravity waves (e.g., gravity wave amplitude) and (2) a sufficiently high vertical resolution in the upper troposphere and lower stratosphere (at least 700 m or smaller).

2.3.3 Interactive ozone in climate models

Ozone in observation has large spatial and temporal variabilities. Due to the ozone (amongst other gases), temperature and circulation are coupled by dynamical, chemical and radiative processes, these variabilities are consistent with the atmospheric dynamics (flow-consistent). How the ozone variability is represented in climate model has large impacts on climate simulations and projections (Nowack et al. 2015; Sassi et al. 2005; Haase et al. 2018). A flow-consistent representation of ozone requires the climate model to calculate ozone interactively, i.e., ozone chemical reactions in chemistry schemes, and ozone transport in conjunction with atmospheric dynamics and/or ozone in radiation schemes. This enables simultaneous coupling between the ozone and circulation. However, due to the computational cost of full interactive chemistry calculations, instead, prescribed ozone fields as zonal and monthly mean climatology are generally applied for majority climate models. When using zonal and monthly ozone climatology as the boundary condition in climate simulations, the ozone asymmetries and temporal variability are missing.

The fully interactive chemistry ozone calculation can be approximated in several ways, which significantly reduce the computational cost required. In a linearized ozone scheme (e.g., Linoz), a first order Taylor expansion is used to approximate the rate of ozone change relative to a reference condition in terms of ozone mixing ratio, temperature and the locale ozone column. Nowack et al. (2018) use machine learning to build temperature-based ozone parameterizations, which gives better representation of temperature variability. Both methods overcome the computational cost in fully interactive chemistry ozone calculation, while keeping the interactive ozone effect in a simple way. However, both methods are simplified a required work to sufficiently represent different climate change scenarios (background and reference conditions have changed for e.g., Linoz; the data base on which the Nowack scheme is trained would need to be extended). In this thesis, I employ a simple chemistry scheme using Taylor expansion with additional approximation of PSCs effect (see Chapter 6).

Chapter 3 Model description

3.1 Chemistry-climate model ICON-ART

ICON (ICOsahedral Non-hydrostatic model) is jointly developed between the German Weather Service (DWD) and the Max Planck Institute for Meteorology (MPI-M) as a seamless weather and climate modelling system. It has already been extended by the ART module (Aerosols and Reactive Trace gases) (Rieger et al. 2015), developed at the Karlsruhe Institute of Technology (KIT). Some features are listed below (see Wan et al. (2013a); Zängl et al. (2015)),

- The ICOsahedral (grid) stands for icosahedron, which is a convex solid and consists of 20 equilateral triangles. A desired resolution is reached through recursively subdividing an icosahedron and projecting the result onto the circumscribed sphere. The advantage of icosahedral grid is the absence of polar convergence issues that are presented in the longitude-latitude grid models.
- Non-hydrostatic model means the model uses a non-hydrostatic atmospheric dynamic core without the hydrostatic approximation. The benefit of a non-hydrostatic dynamic core is its ability to handle convective instability (Ohfuchi and Hamilton 2010). Thus, it enables for applications global weather forecasting and cloud-resolving climate modelling.
- Scalability and efficiency on massively parallel computing platforms with 10^4 or more cores.
- ART stands for Aerosols and Reactive Trace gases. The goal is to model atmospheric chemistry, aerosol chemistry and dynamics, and related feedback processes (Rieger et al. 2015; Schröter et al. 2018). With the extension of ART, ICON-ART is often referred to as a chemistry-climate model.

The climate physics packages, such as cloud microphysics, gravity wave drag and radiative transfer, are derived from ECHAM6 (Stevens et al. 2013) and adapted to the ICON grid (Giorgetta et al. 2018) (hereafter referred to as Gior18).

3.2 Integration strategy

In this thesis, I employed two benchmark integrations: 1) AMIP-type integrations and 2) timeslice integrations.

3.2.1 ICON-ART AMIP simulation

The performance of ICON for AMIP-type (Atmospheric Model Intercomparison Project) simulation has been comprehensively documented in ICON assessment (Crueger et al. 2018; Giorgetta et al. 2018) with different horizontal and vertical resolution as well as a range of physical parameters tuning. They found the model gives a compelling representation of the climate and its variability (e.g., the response of precipitation to El Niño sea surface temperature variability is close to observations). The model performance of ICON-ART for AMIP-type simulation is presented in Schröter et al. (2018).

Table 3.1 – List of physical schemes in ICON-ART

Physics schemes	Description	Reference
Radiation	Radiative transfer	(Pincus and Stevens 2013)
Convection	Cumulus convection	(Nordeng 1994)
Clouds	Cloud microphysics	(Stevens et al. 2013)
GWD	Wave forcing by Hines gravity wave drag	(Hines 1997a, b)
SSO effects	Wave forcing by sub-grid scale orographic effects	(Lott and Miller 1997)
Vertical diffusion	Vertical diffusion	(Mauritsen and Svensson 2007)
ART module	Aerosols and Reactive Trace gases	(Rieger et al. 2015)

The climate version of ICON-ART adopts its physics schemes from ECHAM6 (Stevens et al. 2013) with modification of time stepping scheme, grid discretization and vertical coordinate system. Table 3.1 lists the physics schemes in ICON-ART. The physics schemes calculate atmospheric tendencies (e.g., temperature and momentum), and then feedback onto the dynamics. For the AMIP-type run, the grid takes R2B4 (approximately 160 km) with 47 vertical layers. The prescribed boundary conditions include sea surface temperature (SST) and sea ice concentration (SIC) and greenhouse gases and aerosols, which are read from provided datasets and interpolated to model timestep and grid.

3.2.2 ICON-ART timeslice simulation

The timeslice integration uses the same basic settings of AMIP-type run, but the transient boundary conditions are replaced with annually invariant ones, repetitive boundary conditions of year 2000. When neglecting the interannual variability of boundary conditions (e.g., SST/SIC), it helps to assess the variability that comes from the atmospheric internal dynamics.

Chapter 4 Bias characterization and rectification

4.1 Introduction

An accurate representation of the stratosphere is not only important for medium-range weather forecasts, but also for climate projections, such as the projection of ozone recovery. With the advent of fast computer resources, high-top general circulation models (GCMs) are more commonly used to better simulate the observed structure and variability of the middle atmosphere (Garcia et al. 2007; Hardiman et al. 2010). The middle atmosphere climate is determined by the dominant processes of radiation and wave drag arising from the deposition of momentum from the breaking of small-scale gravity waves (both orographic and non-orographic) and large-scale planetary waves (such as Rossby waves or Kelvin waves), which is related to the upward propagation of waves from the troposphere to the stratosphere and subsequent breaking and dissipation (Polichtchouk et al. 2017). Small-scale gravity waves are not resolved in most GCMs and the related wave drag is included via parameterizations. Models without small-scale gravity wave drag effects are biased to cold polar stratosphere during winter (Palmer et al. 1986). Parameterizations characterize gravity wave sources, wave propagation and subsequent wave dissipation processes. There are certain semi-empirical or artificial parameters that are poorly constrained by observations (Geller et al. 2013). In order to obtain more realistic middle atmospheric mean states or variability (QBO or SSWs), tuning of these parameters is often necessary.

The gravity wave drag parameterizations are generally grouped into (1) subgrid-scale orographic (SSO) gravity wave drag and (2) non-orographic gravity wave drag (NONGWD). In the climate version of ICON-ART, the physical parameterizations use ECHAM physics (Stevens et al. 2013), where the SSO drag is parameterized following Lott and Miller (1997); and the NONGWD is parameterized following Hines (1997a,b).

The model performance of an ICON AMIP-type simulation (without the ART module) has been assessed in Gior18, where they show that the circulation in the stratosphere and in the mesosphere is biased against reanalysis data, especially in the winter hemisphere. This issue is also presented in Schröter et al. (2018), where the ART module is included.

In this chapter, I aim to characterize the bias in ICON-ART using a series of standard AMIP-type simulations, with special emphasis on bias in the middle atmosphere. These biases are defined relative to European Centre for Medium-Range Weather Forecasts (ECMWF) reanalysis data. Furthermore, how the bias is related to gravity wave parameterizations is investigated. In Section 4.2, model experiments, the dataset used to assess model performance and diagnostic metrics are described. In Section 4.3, I present the model bias in temperature, zonal winds and planetary waves, and the correction of the bias in Northern Hemisphere winter by tuning the SSO gravity wave drag. In Section 4.4, the QBO in the tropical stratosphere is carefully examined. Finally, In Section 4.5, here is the summary and conclusions.

4.2 Data and methods

In this thesis, the ERA-Interim reanalysis (ERA-I, Dee et al. 2011) from the ECMWF is used to evaluate ICON-ART AMIP-type simulations. The ERA-I data are from 1979 to 2008 with a grid resolution of 1.5°x1.5°, which is consistent with the model outputs.

4.2.1 Model experiments

Model evaluation is firstly based on the basic settings of ICON-ART AMIP-type simulation that have been introduced in Chapter 3 (denoted as ICON-CTL). Then, gravity wave drag parameter tuning and relaxation method is used to reduce the model bias. The corresponding experiments are described in Table 4.1 (see Chapter 3) that will be examined in this chapter.

Table 4.1 – List of ICON-ART AMIP-type simulations.

Abbreviation	Description
ICON-CTL	Control run, which is similar to Gior18 and Schröter et al. (2018)
ICON-SSO40	Subscale-scale orographic (SSO) gravity wave drag above 40 km (no SSO drag) is switched off (see Section 4.3.1)

ICON-NONGWD	The non-orographic gravity wave drag (NONGWD) is tuned by increasing the total root-mean-square gravity wave speed at the source level (see Gior18), with rmscon=1.5
ICON-QBO	To include a stratospheric QBO, the QBO-varying wind profile from ERA-I is directly imposed by relaxation

4.2.2 Diagnostics

4.2.2.1 Transformed Eulerian Mean (TEM)

The TEM equation provides a useful framework to diagnose the effect of atmospheric waves on the mean flow. In log-pressure coordinate (Andrews et al. 1987), the TEM equation is formulated as

$$\frac{\partial \bar{u}}{\partial t} + \left[\frac{1}{a\cos\phi}\frac{\partial(\bar{u}\cos\phi)}{\partial\phi} - f\right]\bar{v}^* + \bar{w}^*\frac{\partial \bar{u}}{\partial z} = \frac{1}{\rho_0 a\cos\phi}\nabla\cdot F + \bar{X}\ ,$$

where $\bar{u}$ is the zonal mean zonal wind; ρ_0, f and a are air density, the Coriolis parameter and Earth's radius; z and ϕ are log-pressure height and meridional radian; the vector $(\bar{v}^*, \bar{w}^*)$ represents the northward and upward components of the residual mean circulation. The Eliassen–Palm (EP) flux divergence (EPFD) $\nabla\cdot F$ is defined as

$$\nabla\cdot F = \frac{1}{a\cos\phi}\frac{\partial(F_\phi\cos\phi)}{\partial\phi} + \frac{\partial Fz}{\partial z}\ ,$$

where the (F_ϕ, F_z) is the EP flux vector and is defined as

$$F_\phi = \rho_0 a\cos\phi\left(\frac{\overline{v'\theta'}}{\partial\bar{\theta}/\partial z}\frac{\partial\bar{u}}{\partial z} - \overline{u'v'}\right)$$

$$F_z = \rho_0 a\cos\phi\left[\frac{\overline{v\prime\theta\prime}}{\partial\bar{\theta}/\partial z}\left(f - \frac{1}{a\cos\phi}\frac{\partial(\bar{u}\cos\phi)}{\partial\phi}\right) - \overline{u'w'}\right].$$

The TEM equation relates the zonal mean flow acceleration to the residual mean circulation $(\bar{v}^*, \bar{w}^*)$ and wave forcing. The wave forcing consists of resolved $(\nabla\cdot F)$ and unresolved one $(\bar{X})$ (such as small-scale gravity wave drag). See Appendix A for more details.

4.2.2.2 Planetary wave amplitude

I use monthly-mean temperature to derive wave number 1–3 and their amplitude. Firstly, the temperature perturbation is defined as the departure from the zonal average and is formulated as

$$T' = T - \bar{T}.$$

Here, $\bar{T}$ is the zonally averaged temperature. Then, at a specific height and latitude(z, ϕ), temperature perturbation could be decomposed into their harmonics (zonal wave number) and is formulated as Fourier transform

$$T' = \sum_{k=1}^{n} A_k(z,\ \phi)\exp\left[i(kx)\right], \mathrm{k}=1, 2, 3\ldots,$$

where A_k is wave amplitude of wave number k, and $\mathrm{z},\ \phi$ and x are altitude, latitude and longitude, respectively.

4.2.2.3 Stratospheric wave spectral analysis

Equatorial waves, coupled with convection, consist of Kelvin waves, mixed Rossby gravity waves, equatorial Rossby waves and internal gravity waves, which are trapped near the Equator. They are detected in observational data (e.g., reanalysis data and satellite data) and could be explained by shallow water equations (see Appendix B). Momentum force by their vertical propagation and dissipation is believed to be the essential for the stratospheric QBO. Therefore, it is important to know how the equatorial waves is simulated and what is the momentum forcing associated with them. Here, the spectral wave analysis is used to detect equatorial waves. Then, the modelled equatorial wave spectra are evaluated against the equatorial wave spectra from ERA-I. Following the method (Hendon and Wheeler 2008; Kiladis et al. 2009), both power spectra and cross-spectra are calculated. See Appendix B for more details.

4.3 Model bias with respect to ERA-I

Here, the mean states of ICON-ART are compared with that of ERA-I, and the model bias is defined as the 30-year mean differences between ICON-ART and ERA-I. The robustness of

the differences is examined using a two-sided Student's *t* test and only the statistically significant differences are analysed.

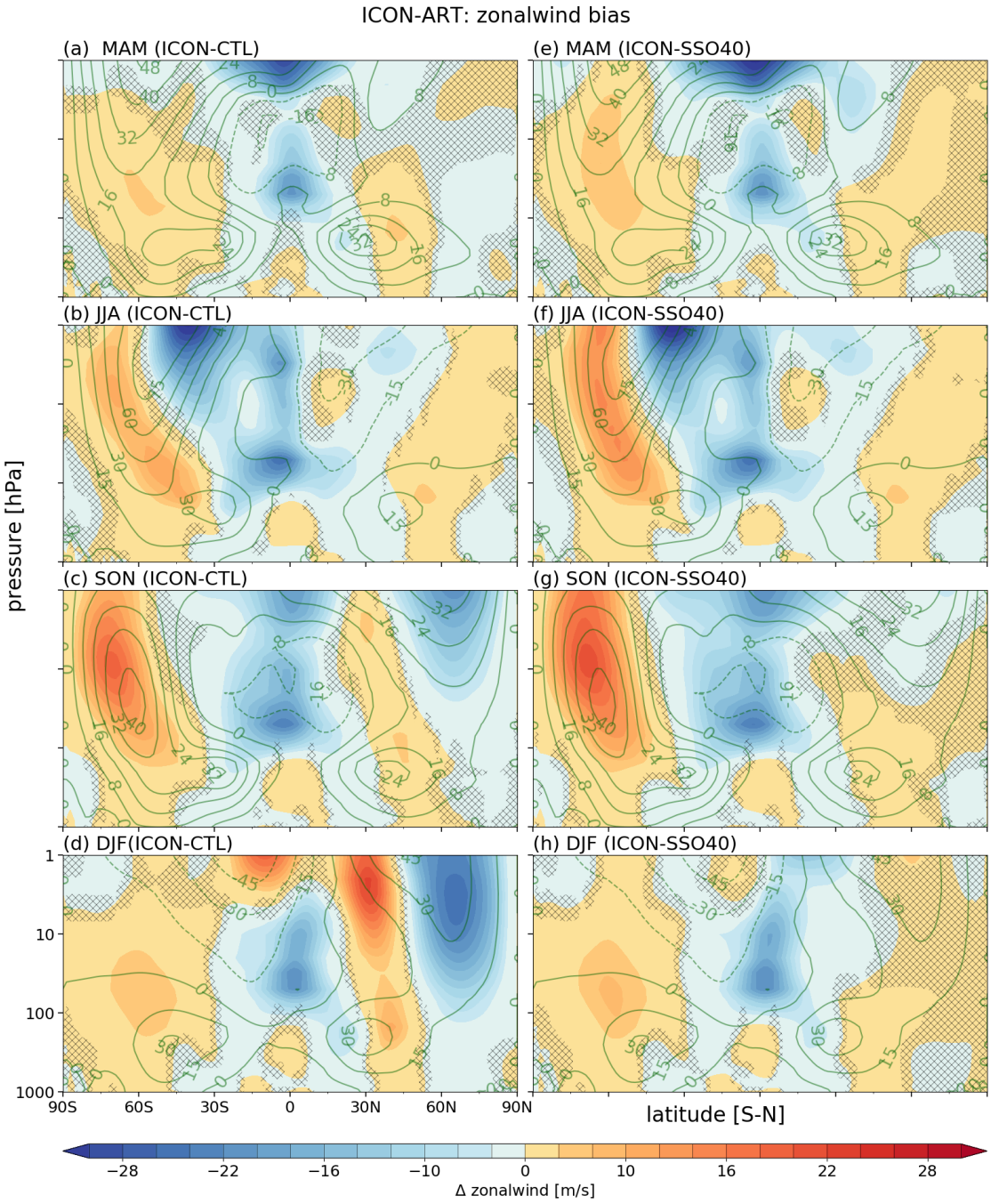

Figure 4.1– Left panel: seasonal and zonal mean zonal wind differences between ICON-CTL and ERA-I for four seasons: (a) MAM, (b) JJA, (c) SON and (d) DJF. Right panel: the same as upper panel, but for the differences between ICON-SSO40 and ERA-I. The contours are the seasonal mean climatology of zonal mean zonal wind of ERA-I. Stippling denotes the differences that are not significant at the 95% ($p = 0.05$) confidence level.

4.3.1 Model bias in seasonal mean temperature and zonal wind

Figure 4.1 (a–d) shows the seasonal and zonal mean zonal wind (ZMZW) differences between ICON-CTL and ERA-I for four seasons (i.e., MAM, JJA, SON and DJF). Note the grey hatching denotes the differences that are not significant at 95% confidence level. For the Southern Hemisphere (SH), the simulated polar stratospheric westerly jets are significantly stronger than that in ERA-I, extending from ~150 hPa to 1 hPa. The largest wind bias is found during SON, when the difference exceeds ~30 m/s (Figure 4.1c), indicating that the simulated strength of the winter residual circulation downwelling in the SH is very weak. For the Northern Hemisphere (NH), however, the polar stratospheric westerly jets are significantly weaker than that in ERA-I, especially during SON and DJF (Figure 4.1c and Figure 4.1d), and the polar night jet (10 hPa and 60° N) is negatively biased by ~25 m/s with respect to ERA-I. Meanwhile, the simulated tropical westerly jets in the mid-latitudes are stronger and located more northward for all four seasons. The substantial negative biases in the NH winter polar stratosphere suggest that the simulated strength of the residual circulation downwelling is too strong. For the tropical stratosphere, significant negative biases are found for all four seasons, and the easterlies are dominant, implying that the model is lacking a QBO-like oscillation.

Figure 4.2 (a–d) shows the seasonal differences of zonal mean temperature (ZMT) between ICON-CTL and ERA-I. For the SH, there are significant cold biases in the lower stratosphere and warm biases above that, from 10–1 hPa (Figure 4.2a–d). According to thermal wind balance, the cold biases are just consistent with the significantly stronger polar night jet in Figure 4.1. The cold biases in the lower stratosphere (below 10 hPa) peak in autumn (SON) (Figure 4.2c) and the simulated temperature is approximately 12 K lower than that in ERA-I. The cold-pole biases in the SH are largely related to the strength of residual circulation, which is driven by the unresolved gravity wave drag (parameterized in the model) and the resolved large scale wave drag. This problem is quite prevalent in the chemistry-climate models (Eyring et al. 2006) as well. The gravity wave parameterizations are possibly playing an important role (see Butchart et al. (2018)). For the NH, above 10 K warming through the polar stratosphere is found during SON and DJF, which is related to the weaker polar night jet (Figure 4.2c–d). Contrary to the SH, the wave drag (resolved or unresolved) at NH winter pole might be largely overestimated as also pointed out by other studies (e.g., McLandress et al. (2011)). Using the ICON (without the ART module) in an AMIP-type simulation, Gior18 also found that the circulation in the stratosphere and the mesosphere is highly biased against ERA-I, especially

in the winter hemisphere, where too much gravity wave drag is exerted. They notice the problem is related to the parameterization of the SSO drag. For the tropical stratosphere, a significant cold bias is found in the lower stratosphere all year-round and a warm bias in the upper stratosphere but only in DJF, suggesting that there is no QBO-like oscillation simulated in ICON-ART.

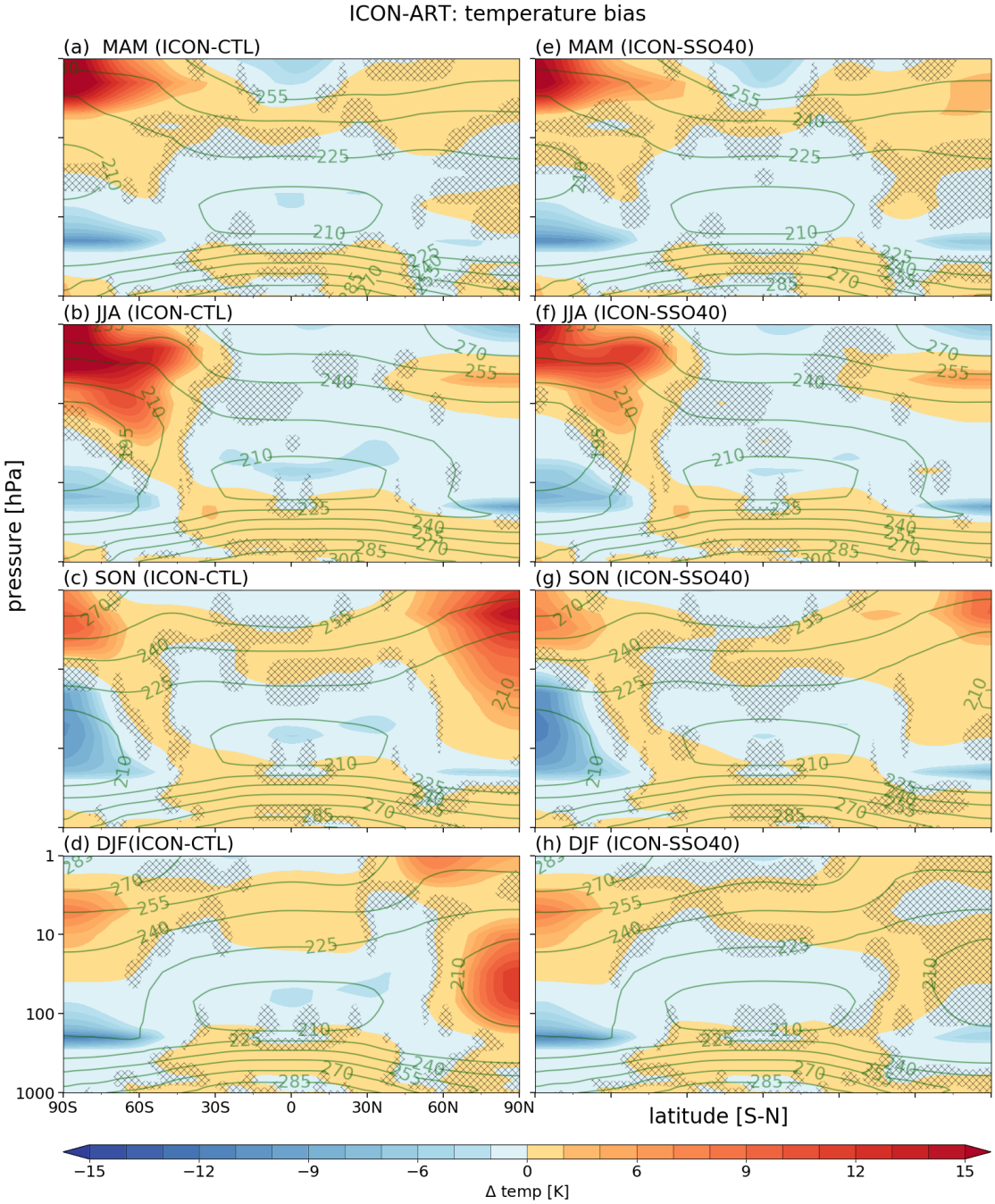

Figure 4.2– the same as Figure 4.1, but for zonal mean temperature.

To sum up, the simulated stratospheric mean states are biased, compared to ERA-I exhibiting: 1) SH polar winter cold biases; 2) NH polar winter warm biases, and 3) no stratospheric QBO-like oscillation.

To correct the NH warm biases, the SSO drag parameterization is tuned. The remedy which is from NWP physics (numerical weather prediction version of ICON-ART) just sets height dependent limits to constrain the development of SSO drag. Here, I simply switched off the SSO drag for model levels that are above 40 km, which is similar to previous studies (Scaife et al. 2000; Wells 2015). After switching off the SSO drag, the same AMIP run is conducted, and is denoted as ICON-SSO40 (see Table 4.1).

To test the effect of SSO drag reduction, the seasonal mean ZMZW and ZMT differences between ICON-SSO40 and ERA-I for four seasons are computed and shown in the right panel of Figure 4.1 and Figure 4.2. Due to the reduction of SSO gravity wave drag entering upper stratosphere and above, the biases of polar night jet and temperature in the NH polar stratosphere during SON and DJF have been largely reduced (Figure 4.1g–k and Figure 4.2g–k). Although the polar night jet in SON and DJF is slightly higher and the polar stratosphere is slightly warmer than that of ERA-I, the differences are not significant at all (Figure 4.1g–k and Figure 4.2g–k). Except for that, the biases in tropical stratosphere and SH polar stratosphere are nearly identical to that of ICON-CTL (see Table 4.1 where different ICON-ART AMIP-type runs are defined).

Based on the above analysis, the switching off SSO drag above 40 km in ICON-SST40 largely reduces the NH warm biases during SON and DJF. Hereafter, the results from ICON-SSO40 are also displayed below.

4.3.2 Tropospheric impacts of stratospheric biases

Due to the stratosphere-troposphere coupling (see Figure 1.1), the stratospheric biases link down to the troposphere. Figure 4.3 shows the ZMZW difference between ICON-CTL and ICON-SSO40 with special concern of the NH troposphere. During the winter, when the stratosphere-troposphere coupling is active (planetary waves into the stratosphere are available), the ZMZW difference shows a meridional dipole with a node centred at ~45° N indicating a poleward shift of the polar stratospheric jet in ICON-SSO40. This meridional dipole resembles a NH annular mode (NAM) pattern.

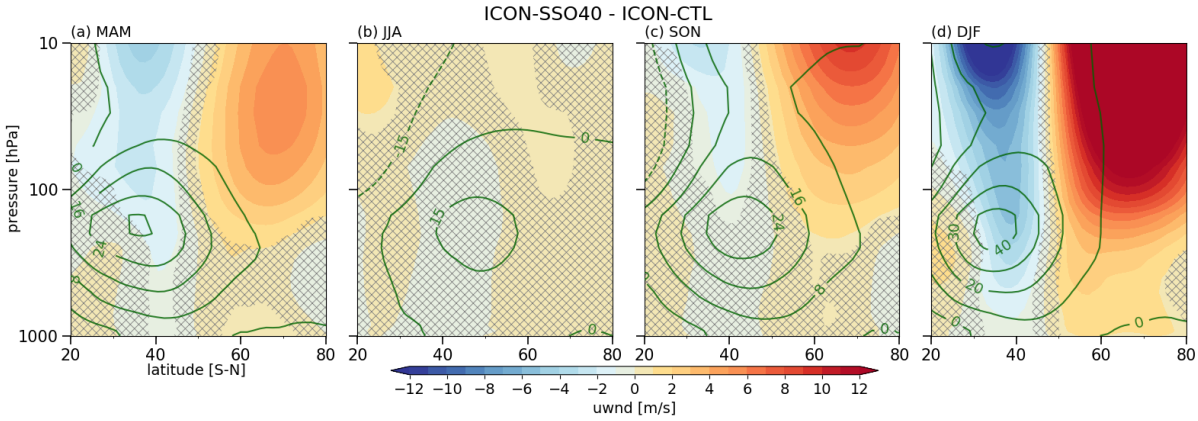

Figure 4.3– The same as Figure 4.1, but for the zonal mean zonal wind differences between ICON-SSO40 and ICON-CTL, and with special emphasis on the Northern Hemisphere (NH) and troposphere.

Figure 4.4 further shows the differences in temperature at 50 hPa and 850 hPa. In ICON-SSO40, the polar vortex is significantly colder, resulting in significantly warming northern Siberia and cooling the Arctic Archipelago. The lower tropospheric temperature response largely resembles the positive Arctic Oscillation (AO) pattern, which is the surface pattern of the downward propagation of NAM (Thompson and Wallace 2000). Similarly, the colder SH polar stratosphere biases induce a positive phase of SH annular mode (SAM) that propagates downward, leading to a poleward shift of the tropospheric jet (not shown). The results suggest the model biases at the middle stratosphere are significantly connected to the troposphere climate via stratosphere-troposphere coupling.

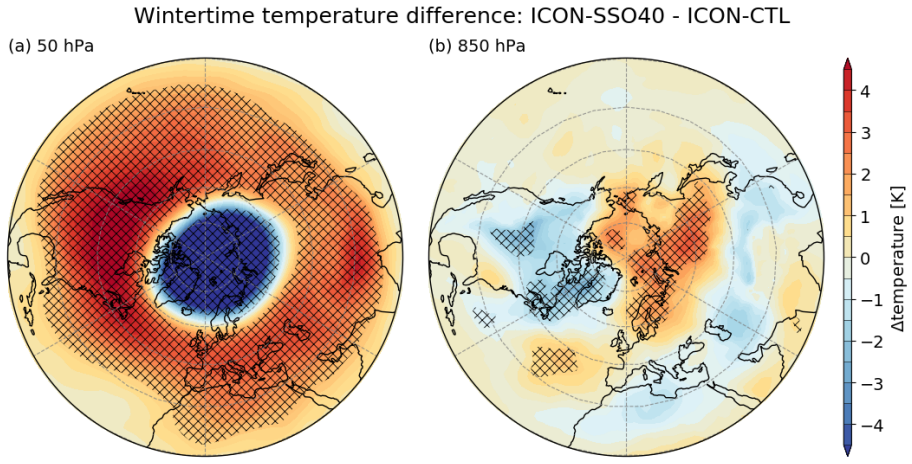

Figure 4.4– Wintertime (DJF) temperature differences at 50 hPa and 850 hPa between ICON-SSO40 and ICON-CTL. During NH wintertime, the coupling between stratosphere and troposphere is active. Stippling denotes the differences that are not significant at the 95% (p = 0.05) confidence level.

4.3.3 Polar night jet and temperature biases

Figure 4.5 shows the annual cycle of the NH and SH polar night jet (defined as zonal wind at 10 hPa and 60° N and 60° S) for ICON-CTL, ICON-SSO40 and ERA-I. For the NH, the evolution of the polar night jet of ICON-CTL is approximately flat from September through March with a constant wind speed about 10 m/s (green line). This differs significantly from that of ICON-SSO40 (brown line) and ERA-I (blue line), where the acceleration of polar night jet from September to March is quite evident. The evolution of the polar night jet in ICON-SSO40 and ERA-I matches very well, except for February and March where ICON-SSO40 simulates a stronger westerly jet. According to the TEM equation, both the resolved and unresolved wave drag provide potential forcing on the mean flow. For ICON-CTL, the SSO drag dominates over the other wave forcing. The extensive SSO drag not only leads to a very flat polar night jet in ICON-CTL, it also damps the planetary wave activities. The overlaid standard deviation of the polar night jet is very small in ICON-CTL. In ICON-SSO40, however, the reduction of SSO drag makes the standard deviation slightly stronger than that in ERA-I, indicating stronger planetary wave activities. For the SH, both ICON-CTL and ICON-SSO40 simulate stronger polar night jet all year round. Due to the reduction of SSO drag above 40 km, the polar night jet in ICON-SSO40 is strongest from April to October.

Figure 4.6 shows the annual cycle of ZMT at 50 hPa as the differences of ICON-CTL and ICON-SSO40 with ERA-I. In both ICON-CTL and ICON-SSO40, the significant cold biases are found in tropical stratosphere all year round, indicating no QBO-like oscillation and the easterlies are prevalent (in Figure 4.10a). Both in ICON-CTL and ICON-SSO40, the far colder SH polar stratosphere is found from May to December (Figure 4.6a–b), which is consistent with a stronger SH polar night jet in Figure 4.5. The cold-pole problem is still present in ICON-SSO40. This indicates that the SSO drag has a smaller impact on the SH than that on the NH pole. For the NH polar vortex evolution, in ICON-CTL, significant warm biases prevail from September to March, with maximum values around January (Figure 4.6a). However, in ICON-SSO40, the biases are very small and not significant at all.

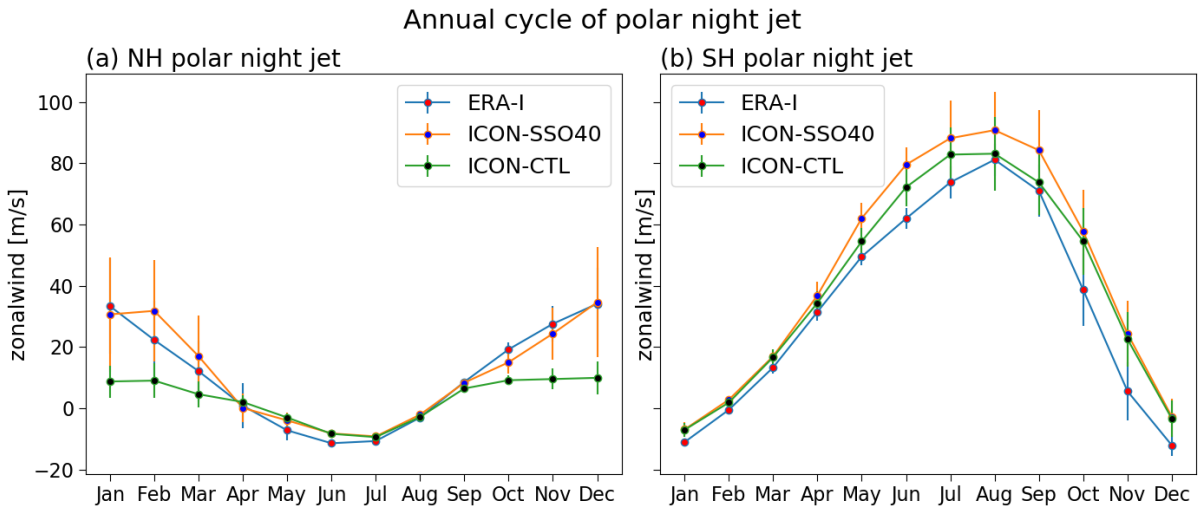

Figure 4.5– 30-year mean annual cycle of polar night jet for the Northern Hemisphere (NH) and Southern Hemisphere (SH) for ICON-CTL (brown line), ICON-SSO40 (green line) and ERA-I (blue line). The polar night jet is defined as zonal mean zonal wind at 10 hPa and 60° N (S). The 30-year standard deviation is overlaid on the average.

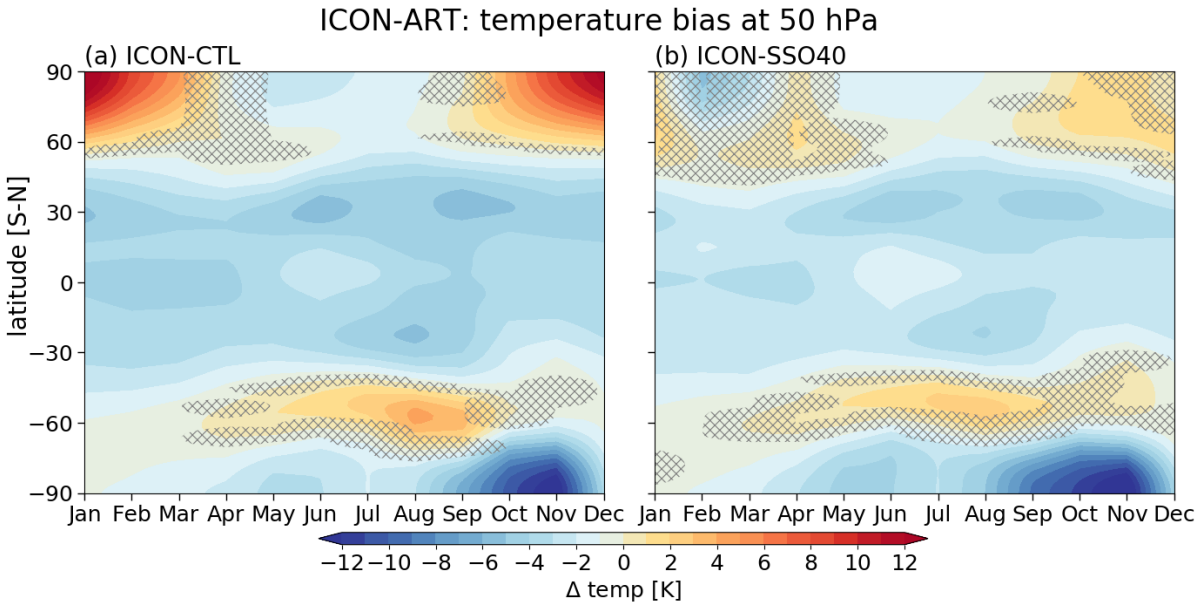

Figure 4.6– The differences of climatological monthly and zonal mean temperature at 50 hPa between ICON-ART and ERA-Interim for (a) ICON-CTL and (b) ICON-SSO40. Stippling denotes the differences that are **not** significant at the 95% (p = 0.05) confidence level.

4.3.4 NH planetary waves

The upward propagating planetary waves provide a large portion of total eddy forcing to the extra-tropics, particularly in winter. From the above analysis, the NH polar winter stratosphere

in ICON-CTL is largely biased by too much SSO drag. Here, the representation of planetary waves in the model is examined under conditions of strong SSO drag (ICON-CTL) or no SSO drag (above 40km, ICON-SSO40).

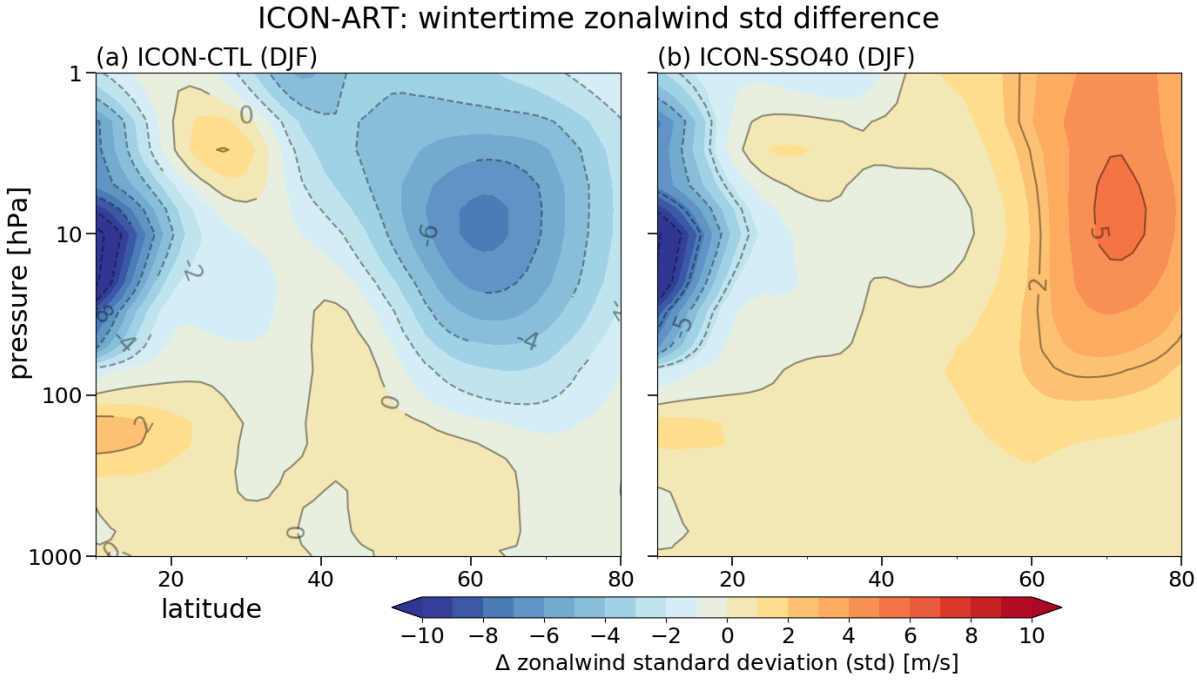

Figure 4.7– The differences in the standard deviation of wintertime (DJF) zonal mean zonal wind for (a) ICON-CTL and ERA-Interim, and (b) ICON-SSO40 and ERA-Interim.

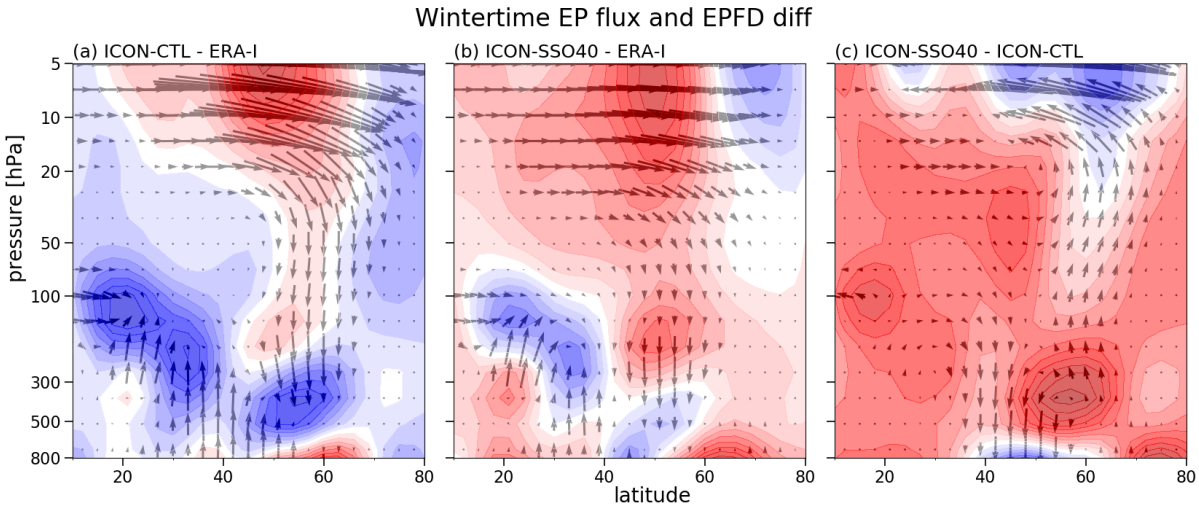

Figure 4.8– Wintertime EP flux vector and EP flux divergence differences for (a) ICON-CTL minus ERA-I and (b) ICON-SSO40 minus ERA-I.

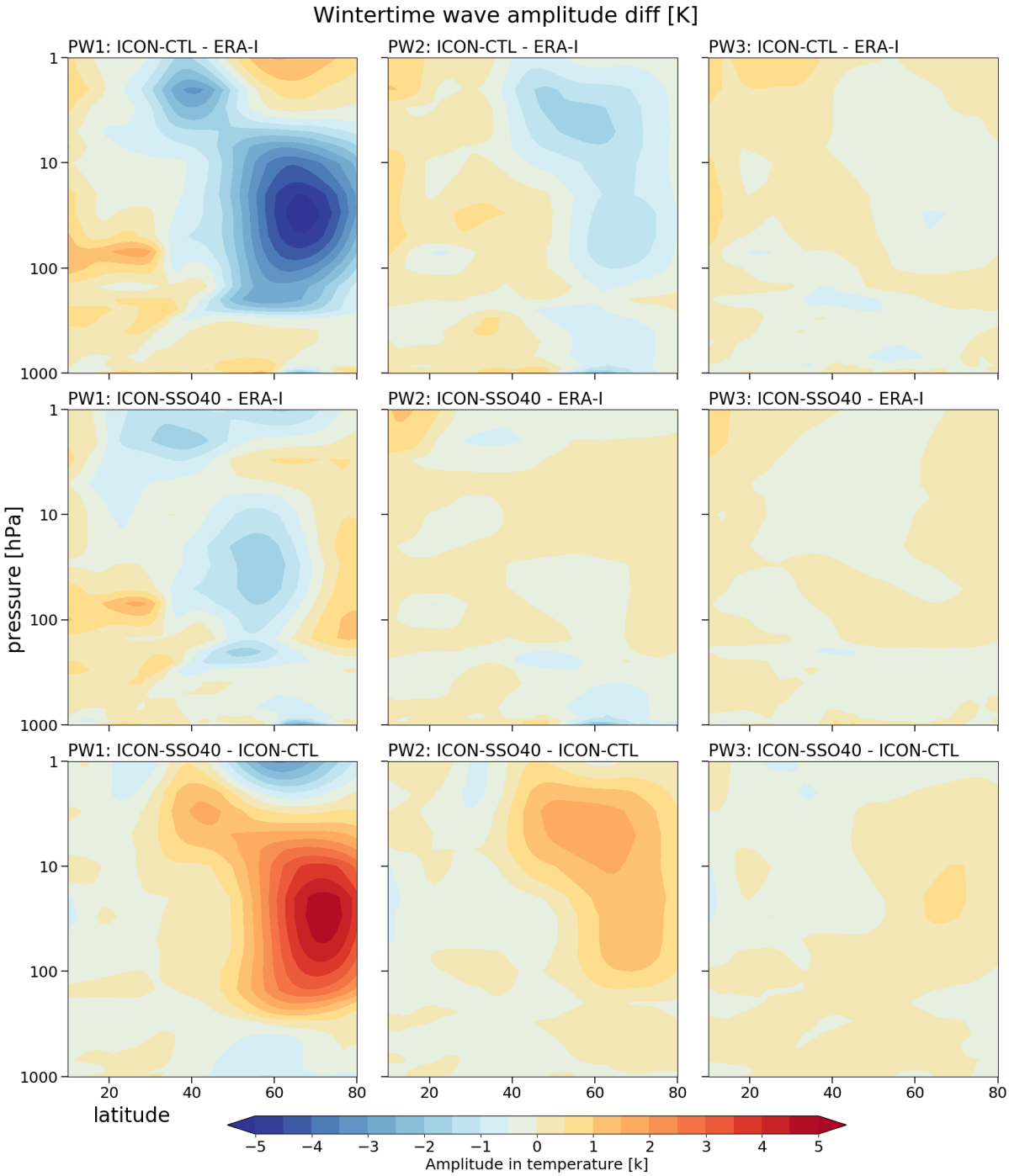

Figure 4.9– The same as Figure 4.6, but for planetary wave amplitude of wave number 1, 2 and 3 (PW1, PW2 and PW3). The amplitude is calculated using temperature field.

Figure 4.7 shows the differences of wintertime standard deviation of ZMZW between model simulations and ERA-I. Both ICON-CTL and ICON-SSO40 have a very weak zonal wind standard deviation in the tropical stratosphere, indicating a lack of zonal asymmetry. In the upper tropical troposphere, wave activities are stronger in the two model simulations than in ERA-I. For ICON-CTL, comparing to ERA-I, the stratospheric zonal wind standard deviation

is negatively biased from middle-to-high latitude (Figure 4.7a), indicating a lack of wave activities, which is consistent with a much weaker polar night jet in ICON-CTL; for ICON-SSO40, however, the standard deviation is much stronger in the polar stratosphere (Figure 4.7b).

After switching off SSO drag, planetary waves are able to propagate more easily into the stratosphere. The EP flux and its divergence (EPFD) are used to show the planetary wave activities and forcing on the zonal mean flow. Compared to ERA-I, ICON-CTL has fewer planetary waves that propagate vertically from the troposphere to the stratosphere at mid-latitudes (Figure 4.8a). In subtropical regions, the model simulated stronger upward planetary wave activities, leading to stronger wave forcing on subtropical jet at the southern flanks. This is consistent with the weaker subtropical jet in ICON-CTL (Figure 4.1d). For ICON-SSO40, the upward wave propagation is also smaller than for ERA-I (Figure 4.8b), but the absolute deviations are smaller than that for ICON-CTL. This is also seen in Figure 4.8c, implying more planetary waves are able to propagate into the stratosphere when switching off SSO drag.

Figure 4.9 shows the wave amplitude differences for planetary wave number 1, 2 and 3 (hereafter referred to as PW1, PW2 and PW3). In ICON-CTL, the PW1 amplitude is substantially weaker than in ERA-I at polar stratosphere, the PW2 amplitude also shows similar behaviour, although weaker and PW3 doesn't show a difference (Figure 4.9 first row). In ICON-SSO40, the bias in PW1 amplitude becomes smaller, with slightly larger wave amplitude poleward of 60° N and smaller equatorward of 60° N. The slightly larger PW1 amplitude in the polar stratosphere is consistent with the stronger standard deviation in the zonal wind (Figure 4.5b). No big difference is found in the wave amplitude of PW2 and PW3 (Figure 4.9 second row). The third row in Figure 4.9 demonstrates the net effects of SSO reduction on the wave amplitude. It is shown that the wave amplitude of PW1, PW2 and PW3 have substantially increased, particularly above 100 hPa. From the above analysis, it is clear that stratospheric planetary waves are largely suppressed in ICON-CTL, which is due to too much SSO drag exerted. Limiting the SSO drag development at upper altitude (above 40 km) results in more planetary waves propagating vertically from the troposphere into the stratosphere. Note, this is different from the vertical Rossby wave propagation theory (Charney and Drazin. 1961), which states that vertical planetary wave propagation into the middle atmosphere is only possible when the background westerlies are smaller than a critical value ($0 < \mathrm{u} < U_c$). Due to too much SSO drag in ICON-CTL and $\bar{X}$ (the unresolved wave forcing)

is the dominant in TEM momentum equation, and therefore preventing the planetary wave-mean-flow interactions ($\nabla \cdot F$ is too small).

4.3.5 Non orographic gravity wave drag

The parameterization of gravity wave drag is one of the major sources of the middle atmospheric model bias. As is shown in Figure 4.1, the parameterized SSO gravity wave drag is too large, which is responsible for warm biases in the NH winter polar stratosphere. Here, another type of parameterized gravity wave drag, i.e., NONGWD, is tested. In the new experiment, non-orographic gravity wave amplitude at launch height in the Hines parameterization is increased by 1.5. This experiment is denoted as ICON-NONGWD) (also see in Table 4.1).

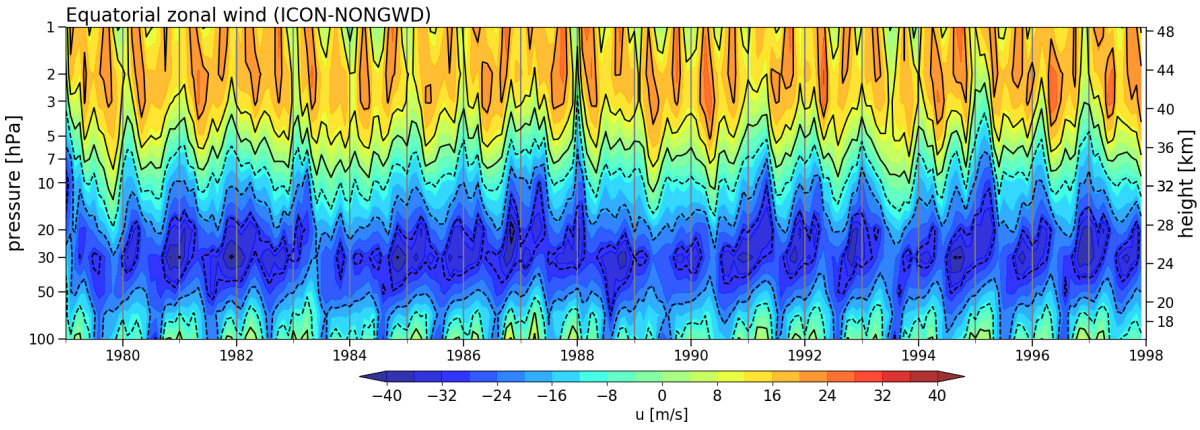

Figure 4.10– Equatorial zonal wind [5° S–5° N] from ICON-NONGWD over the period 1979–1997.

Figure 4.10 shows the modelled equatorial ZMZW of ICON-NONGWD. There is still no QBO-like oscillation, but the ZWZW in the upper stratosphere is substantially larger as compared to ICON-CTL (Figure 4.1a, and also see Figure 4.12a). This indicates the NONGWD is also important for QBO simulation.

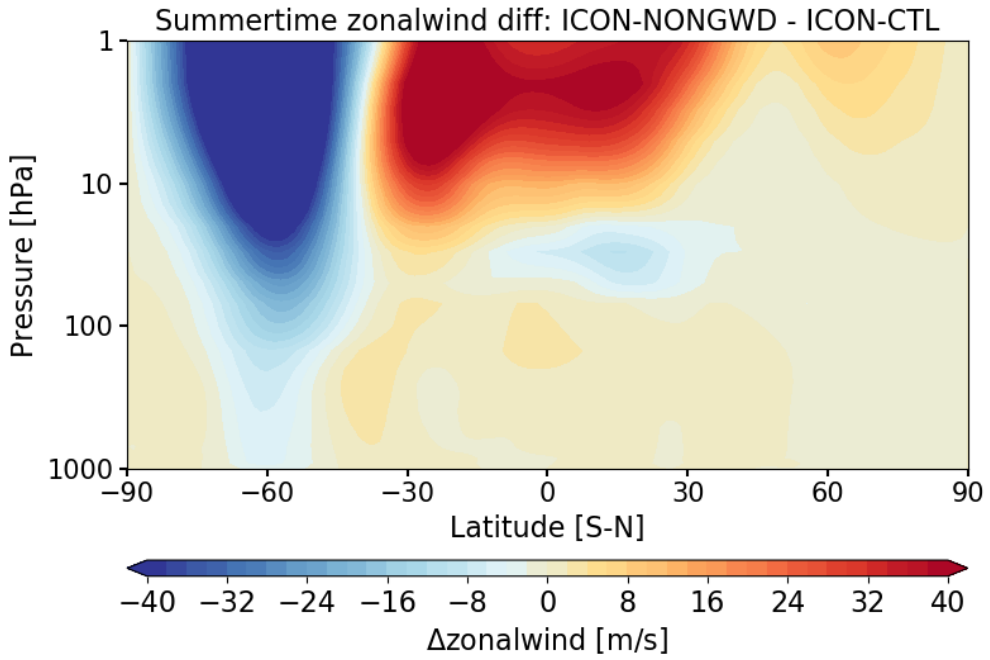

Figure 4.11– Zonal mean zonal wind differences between ICON-NONGWD and ICON-CTL in JJA.

The NONGWD is not only relevant for a QBO simulation, but it is also important for the polar stratospheric simulation. In Figure 4.1, it is shown the SH polar stratospheric jets are far stronger than the ERA-I. Figure 4.11 shows ZMZW differences between ICON-NONGWD and ICON-CTL during JJA. When increase of the gravity wave amplitude at launch height, the SH polar night jet is substantial reduced, suggesting an important direction to rectify the cold biases in the SH pole. I haven't expanded the investigation of NONGWD in this study. More detailed information about the effect of NONGWD on the middle stratospheric circulations is given in Polichtchouk et al. (2017). The representation of stratospheric ozone in the model is also important for SH polar stratosphere, which will be discussed in Chapter 6.

4.4 Tropical stratospheric QBO and wave spectra

The QBO is the dominant mode of variability in the tropical stratosphere and influences the extratropical middle atmosphere in winter by modulation of planetary wave propagation (Baldwin et al. 2001). However, modelling of a realistic QBO remains a great challenge for many numerical models (Butchart et al. 2018). It is shown that among 47 models participating the Coupled Model Intercomparison Project 5 (CMIP5), only five models spontaneously produce a QBO-like behaviour (Butchart et al. 2018). As shown in Figure 4.1, the equatorial

stratospheric winds in ICON-CTL have easterly deviations and the model fails to reproduce a QBO-like oscillation.

In this section, adoption of a QBO relaxation into ICON-ART is discussed to include QBO variability; then, the question why does the model fail to simulate a QBO-like oscillation is examined in the second part.

4.4.1 QBO relaxation in ICON-ART

There are two ways to generate a QBO-like oscillation in a model. One option is tuning the gravity wave parameters or using a fine vertical and horizontal resolution grid, which doesn't necessarily reproduce QBO-like oscillation; another simple and straightforward way to include QBO in ICON-ART is to let the model winds be relaxed to the provided QBO-varying winds. It suffices to investigate the impact of the QBO on the extra-tropics (Matthes et al. 2010).

Here, I adopted a relaxation scheme to relax the stratospheric equatorial winds in ICON-ART approximately to the observed equatorial wind profile of ERA-I. The relaxation scheme follows (Matthes et al. 2010) and the procedure is formulated as follows,

$$\Delta U = F_{mt} + G * \Delta t * (U_{ref} - U_{icon}).$$

In this formula, ΔU is the total wind tendency that accelerates or decelerates the zonal wind in the model; F_{mt} is the wind tendency due to parameterized physical processes (e.g., small-scale gravity waves); G is the relaxation time parameter; Δt is the relaxation time frequency and $(U_{ref} - U_{icon})$ is the wind difference between ERA-I and ICON-ART. The value of the relaxation parameter is set to 1/10 days^{-1} to let the equatorial zonal winds slowly approach that of ERA-I. The nudging is not applied to all levels and places. Vertically, the nudging extends from the lower stratosphere (17 km) to the upper stratosphere (40 km). Below 17 km and down to 14 km, the nudging parameter G gradually reduces to zero; and within 40–65 km, the nudging parameter G gradually reduces to zero. Outside this altitude region (less than 14 km or greater than 65 km), there is no zonal wind relaxation being applied. Horizontally, similar to Matthes et al. (2010), the nudging of zonal wind extends latitudinally from 22° S to 22° N decaying with a Gaussian distribution centred at the equator. The reference wind profile is the monthly mean ZMZW of ERA-I, averaged over 5° S to 5° N from 1979–2008, which is consistent with the ICON-ART AMIP-type simulation period. At each model time step, the

QBO relaxation procedure is called, the monthly reference wind profile is linearly interpolated to the model running time. This ICON-ART AMIP-type run with QBO relaxation is denoted as ICON-QBO (also described in Table 4.1).

Figure 4.12 shows the time-height cross-section of stratospheric equatorial winds for ICON-CTL, ERA-I and ICON-QBO. Obviously, there is no QBO-like oscillation in ICON-CTL and the winds are dominated by easterlies. With the QBO relaxation, though the wind magnitude is slightly weaker (because the soft relaxation is adopted), the ICON-QBO precisely repeats the QBO-like wind variability of ERA-I. Therefore, after the relaxation, the model has a good representation of the observed QBO. The associated equatorial waves are discussed below and the extra-tropical responses are discussed in Chapter 5.

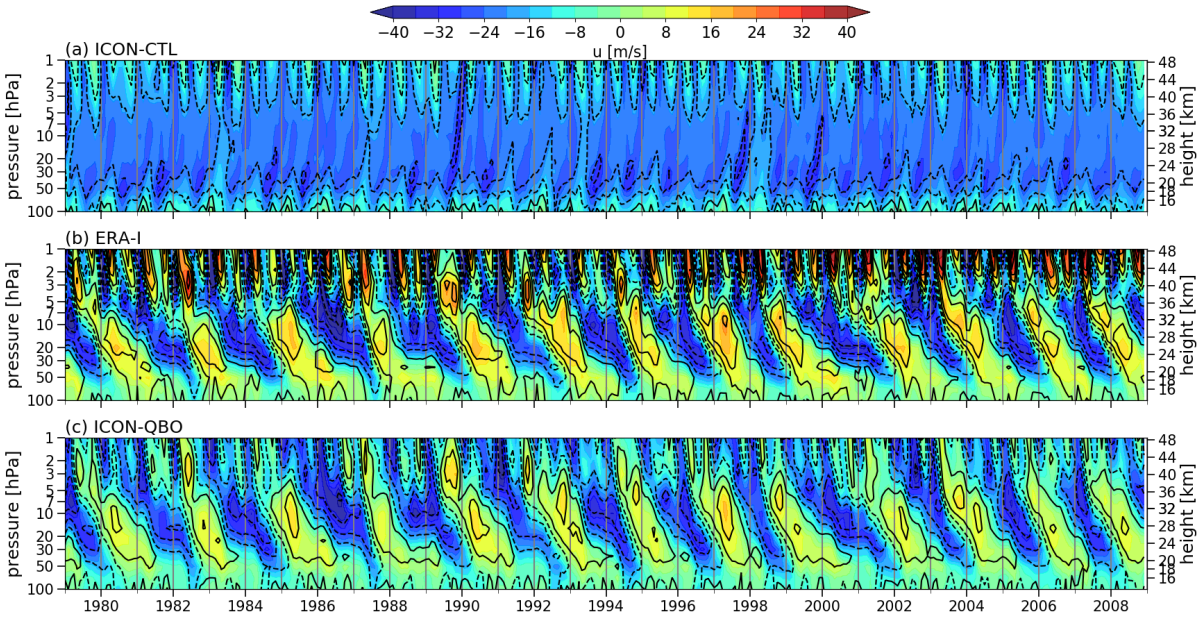

Figure 4.12– Time-height cross-sections of the equatorial zonal wind [5° S–5° N] over the period 1979–2008 for (a) ICON-CTL, (b) ERA-I and (c) ICON-QBO.

4.4.2 Why does the model fail to simulate a QBO?

Momentum transport and its dissipation on the mean flow by a wide range of upward-propagating waves, including large-scale (Kelvin, Rossby and mixed Rossby and gravity waves) and small-scale waves (gravity waves), drive the regular QBO wind cycle. Several studies (e.g., Kawatani et al. 2010; Kim and Chun 2015) suggest that small-scale gravity wave forcing provides roughly half of the eastward acceleration during easterly to westerly QBO

phase transition (resolved wave forcing provides the other half), and is dominant during westerly to easterly QBO phase transition.

4.4.2.1 Momentum balance: a comparison between ERA-I and ICON-ART

The momentum balance in terms of the TEM framework is applied to ICON-SSO40 (without QBO) and ERA-I (with QBO). The wave forcing consists of two types: (1) resolved wave forcing, which is generally resolved in coarse climate model and is represented by EPFD and (2) unresolved wave forcing, which is parameterized in the model. Furthermore, the EPFD consists of a meridional derivative ($\frac{\partial F_y}{\partial y}$ is denoted as dFydy) and a vertical derivative ($\frac{\partial F_z}{\partial z}$ is denoted as dFzdz),

$$\nabla \cdot F = \frac{\partial F_y}{\partial y} + \frac{\partial F_z}{\partial z} = \frac{1}{a cos\phi} \frac{\partial (F_\phi cos\phi)}{\partial \phi} + \frac{\partial Fz}{\partial z}.$$

Figure 4.13 presents the time-height cross-sections of the momentum forcing of EPFD, dFydy and dFzdz, overlaid the stratospheric equational winds. The resolved wave drag is in line with the QBO phase transition, i.e., easterly to westerly transition (zero contour line) is related to positive wave drag and vice versa (Figure 4.13a). The magnitude of positive drag is larger than that of negative drag. The EPFD consists of meridional gradient (dFydy) and vertical gradient (dFzdz). During the QBO phase transition, the dFzdz accounts for the major part of positive wave drag; while, both the dFzdz and dFydy account for part of negative wave drag (Figure 4.13b–c). And at higher altitude (>10 hPa), the stratospheric circulation is more easily affected by resolved wave drag. Furthermore, the dFzdz is decomposed to two components that are related to vertical heat transport and momentum transport:

$$\frac{\partial F_z}{\partial z}|_{\text{heat}} = \text{acos}\phi \frac{\partial \left(\rho_0 \frac{\overline{v'\theta'}}{\partial \bar{\theta}/\partial z} \left(f - \frac{1}{a cos\phi} \frac{\partial (\bar{u} cos\phi)}{\partial \phi} \right) \right)}{\partial z},$$

$$\frac{\partial F_z}{\partial z}|_{mom} = -\text{acos}\phi \frac{\partial (\rho_0 \overline{u'w'})}{\partial z}.$$

Here, the term $\frac{\partial F_z}{\partial z}|_{\text{heat}}$ and $\frac{\partial F_z}{\partial z}|_{mom}$ are denoted as dFzdz_heat and dFzdz_mom, respectively. By comparing dFzdz, dFzdz_heat and dFzdz_mom, it is evident that dFzdz_mom is the dominant, indicating the importance of vertical momentum transport (Figure 4.13e).

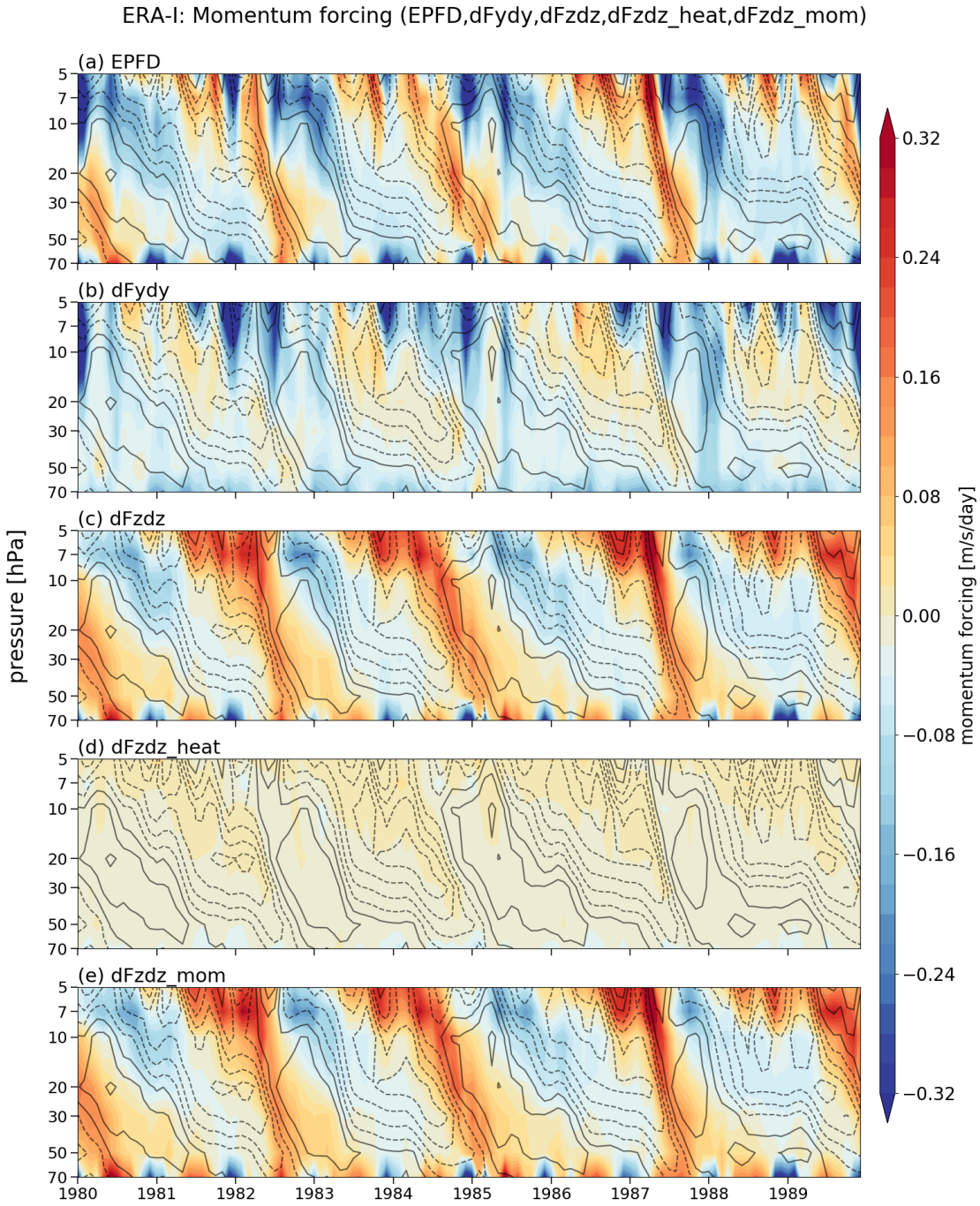

Figure 4.13– Time-height evolution of the momentum forcing by EPFD, dFydy, dFzdz, and dFzdz_heat and dFzdz_mom averaged over 5° S–5° N over the period 1980–1989 based on ERA-I. The dashed and solid lines indicate westerly and easterly equatorial stratospheric wind.

Similar to ERA-I, ICON-SSO40 has strong positive resolved wave drag with prevailing interannual variation in the lower stratosphere (Figure 4.14a). Again, the dFzdz accounts for the major part of positive drag and as well as dFzdz_mom (Figure 4.14e). However, the

resolved wave drag is substantially larger than that in ERA-I and the wave drag has strong interannual instead of quasi-biennial variation.

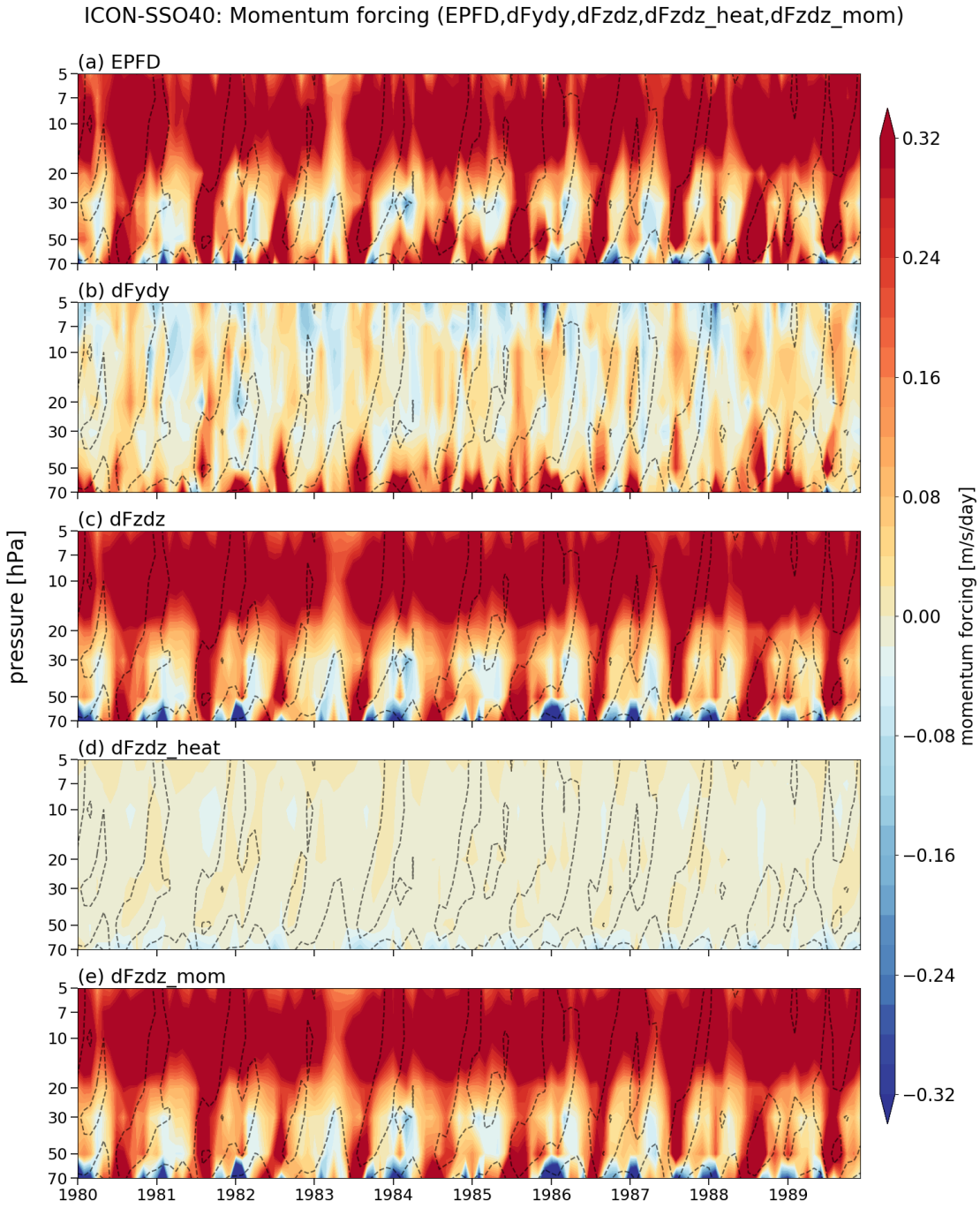

Figure 4.14– The same as Figure 4.13 but for ICON-SSO40.

The momentum balance terms in the TEM equation are displayed in Figure 4.15 for ERA-I and ICON-SSO40. In ERA-I, during QBO easterly to westerly phase transition, the EPFD provides about ~30–40% of total zonal wind tendency (Figure 4.15a, red line). However, during QBO westerly to easterly phase transition, the resolved wave drag is quite small. The unresolved

wave drag that is related to small-scale gravity waves is the primary wave forcing. In ICON-SSO40, the resolved wave drag is substantially larger than that in ERA-I and the peaks of EPFD coincide with strong negative zonal wind tendency. The parameterized gravity wave drag in ICON-CTL (Figure 4.15b, purple line), is almost always negative and the magnitude is very small. Although there is strong westerly forcing in ICON-ART from Kelvin waves, the EPFD is to some extent balanced by residual circulation forcing. Note, the diagnosed terms from the TEM equation are not balanced (due to remapping of native-grid, time-sampling and vertical interpolation).

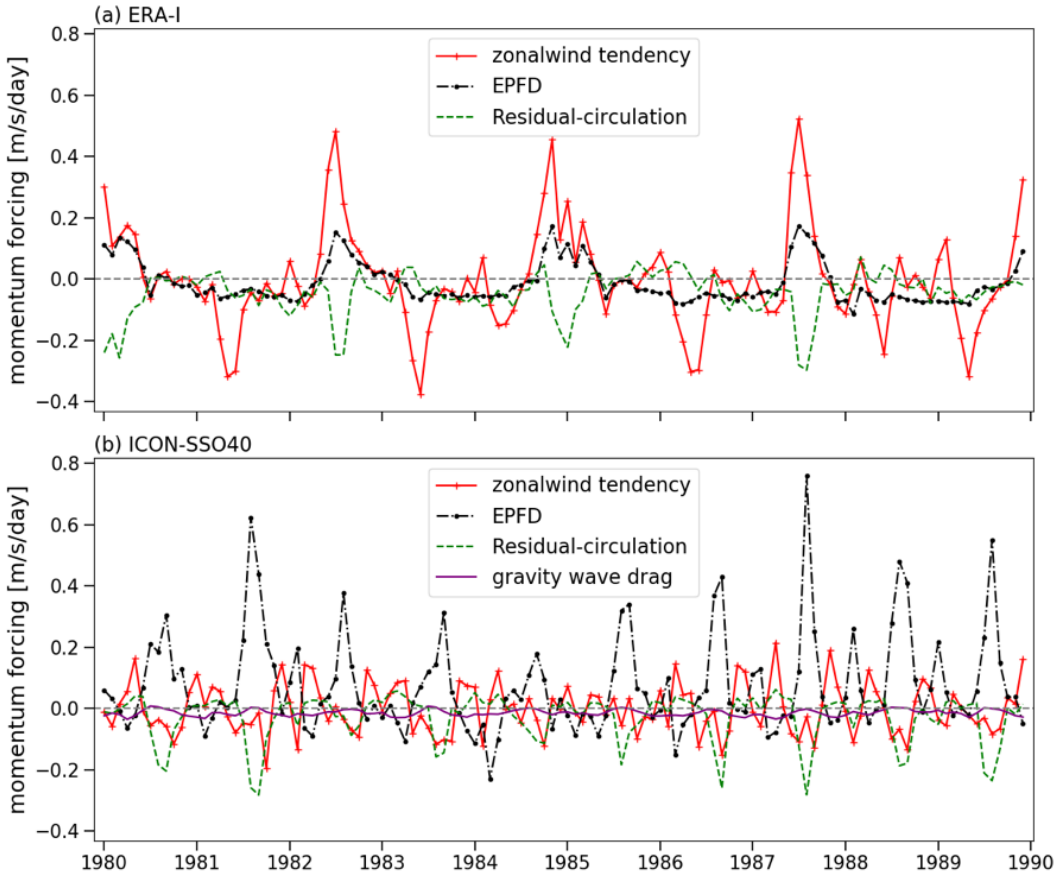

Figure 4.15– Timeseries of momentum forcing for equatorial stratosphere at 30 hPa for the period over 1980–1989, including zonal wind tendency (red line), EPFD (black line), residual-circulation term (green line) and parameterized gravity wave drag (purple line): (a) ERA-I; (b) ICON-SSO40.

4.4.2.2 Equatorial waves: a comparison between ERA-I and ICON-ART

The Kelvin waves and mixed Rossby-gravity waves are two primary waves in tropical stratosphere, which can be resolved in ICON-ART with the current horizontal resolution (~160 km). From the above analysis, in ICON-SSO40 the modelled vertical momentum transfer is far stronger than that in ERA-I, but which particular equatorial wave accounts for the large momentum transfer?

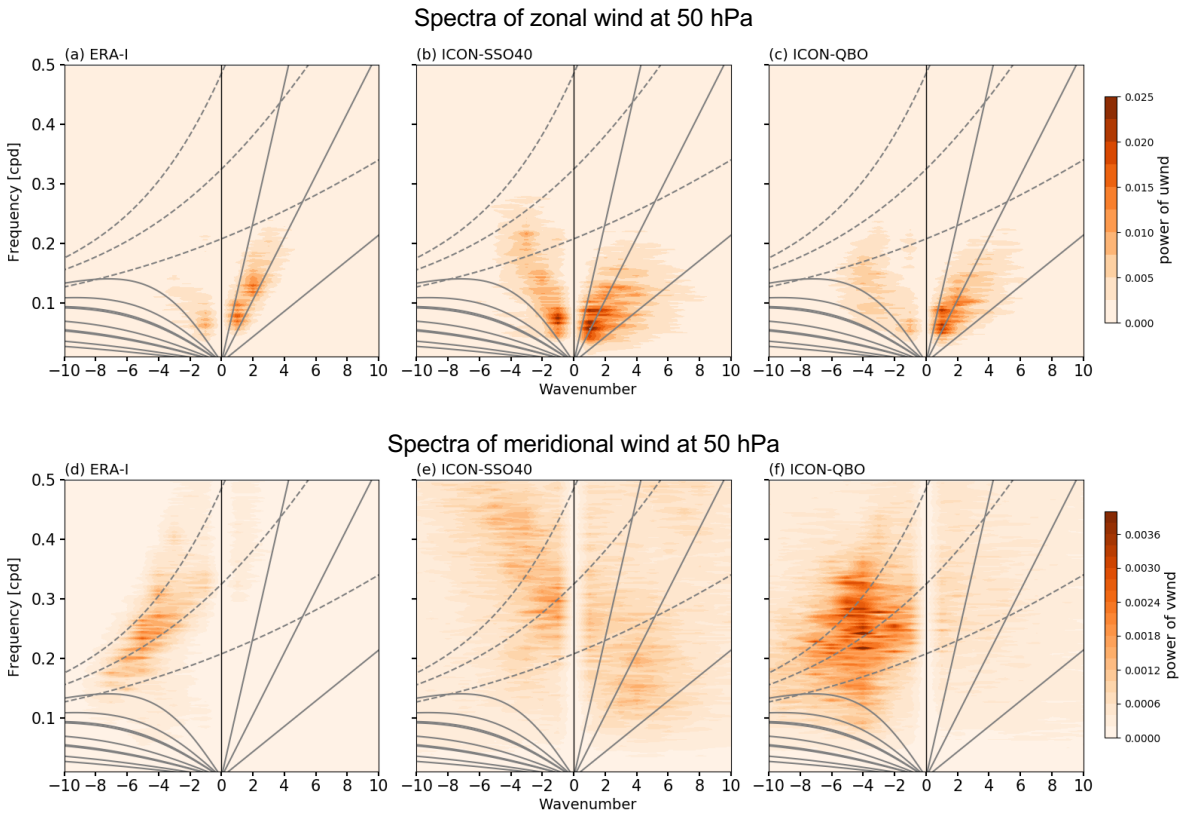

Figure 4.16– Wave number-frequency power spectra of the zonal wind (upper panel) and meridional wind (lower panel) at 50 hPa. Firstly, the zonal wind (meridional wind) is tapered by a cosine (sine) function to represent the symmetric (anti-symmetric) component, and then summed over the latitudinal band [9° S–9° N]. Dispersion curves are overlaid for Kelvin, equatorial Rossby and mixed Rossby-gravity waves with equivalent depths of 10, 60 and 300 m. The background power spectra are removed.

The power spectra of zonal wind and meridional wind at 50 hPa are computed based on daily data and averaged over 10 years. The overlaid dispersion curves are Matsuno-type equatorial waves (solutions to shallow water equations) (see Appendix B). In Figure 4.16, positive wave numbers stand for eastward propagating waves and negative wave numbers westward propagation. In ERA-I, the Kelvin wave spectra are concentrated at higher frequency and

wavenumber (Figure 4.16a). Compared to ERA-I, in ICON-SSO40, the modelled Kelvin waves have stronger power density and the spectral domain of Kelvin waves is broader than that of ERA-I (the region bounded by equivalent depths [10–300 m] vs. [10–60 m] (Figure 4.16a–b)). According to wave-mean-flow interaction theory, the vertically propagating equatorial wave from the troposphere to the stratosphere is filtered by the background wind speed following Doppler shifting (background wind speed equals wave speed). For the eastward propagating Kelvin waves, the vertically transported momentum by the waves is deposited in the mean flow as the wave speed is close to background wind speed. Kelvin waves are an important source of westerly momentum for the QBO, particularly in the lower stratosphere. However, in ICON-SSO40, the dominance of easterlies in the stratosphere largely rules out the possibility of Kelvin wave spectra filtering by the background mean flow. In the QBO relaxation experiment (ICON-QBO), the Kelvin wave power spectra are closer to ERA-I with smaller power density and a narrow spectral band (Figure 4.16c). In ERA-I, the power spectra of anti-symmetric meridional wind at 50 hPa lie in the spectral domain of mixed Rossby-gravity waves (Figure 4.16d). In ICON-SSO40, the power spectra are very dispersive and not concentrated in the spectral domain of mixed Rossby-gravity waves (Figure 4.16e). In ICON-QBO, the spectra are more concentrated within the spectral domain of mixed Rossby-gravity waves but larger in amplitude than that in ERA-I.

In ICON-ART, the modelled EPFD is far stronger than that in ERA-I and the dFzdz_mom is the primary component (Figure 4.14), which is proportional to the momentum flux $\overline{u'w'}$. The cross-spectra of $\overline{u'w'}$ are shown in Figure 4.17 for ERA-I, ICON-SSO40 and ICON-QBO. For ERA-I, the cross-spectra peaks at 50 hPa are mainly lying along the Kelvin wave dispersion curves with equivalent depth of 10–60 m (Figure 4.17a). This is similar to the power spectra of zonal wind at 50 hPa, suggesting the momentum flux $\overline{u'w'}$ is mainly from Kelvin waves. For ICON-SSO40, the cross-spectra of $\overline{u'w'}$ at 50 hPa shows broader maximum values for wavenumbers between 1–9 and for periods less than ~5 days (0.2 cycle per day) (Figure 4.17b), with a significant increase of the magnitude. This means in ICON-SSO40, in the lower stratosphere, the Kelvin wave spectra correspond to large range of equivalent depths. On the contrary, in ICON-QBO, the Kelvin wave spectra are largely constrained with similar spectral peaks in the wavenumber and the frequency domain (Figure 4.17c). At 10 hPa, the peaks of the cross-spectra in ERA-I shift a little bit to higher equivalent depth with respect to that at 50 hPa, and the cross-spectra peaks in ICON-SSO40 also show broader in spectral domain and

larger value in amplitude (Figure 4.17d–e). This gives rise to the exceptional large values of dFzdz_mom as well as EPFD in ICON-SSO40 (Figure 4.14a and 4.14e). The poorly represented Kelvin wave spectra in ICON-SSO40 are mainly due to a lack of background wind filtering. Since the stratospheric equatorial zonal winds are dominant by easterlies, the eastward propagating Kelvin waves don't have the chance to approach the critical level, i.e., the mean flow speed equals phase speed, therefore it generally rules out the wave absorption and mean-flow acceleration.

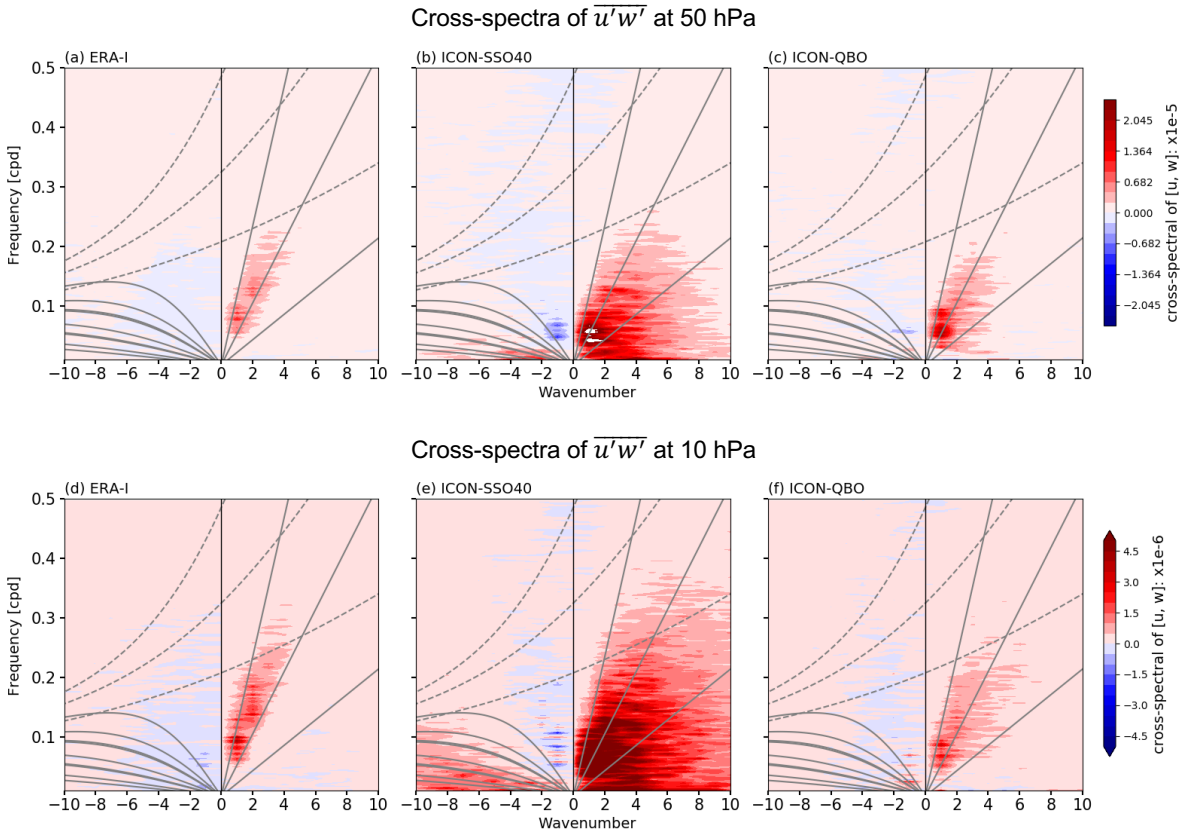

Figure 4.17– wavenumber-frequency cross-spectra of $\overline{u'w'}$ at 50 hPa for (a) ERA-I, (b) ICON-SSO40 and (c) ICON-QBO; (d), (e) and (f) are the same as (a), (b) and (c), but for cross-spectra of $\overline{u'w'}$ at 10 hPa.

4.5 Summary and conclusions

In this chapter, the climatology and variability of ICON-ART long-term simulation (AMIP-type) is examined with respect to ERA-I data. The modelled stratospheric mean states exhibit substantial biases: 1) SH polar winter cold biases; 2) NH polar winter warm biases, and 3) no stratospheric QBO-like oscillation.

The biases in the NH winter polar stratosphere have been found to be related to extensive subgrid-scale orographic (SSO) wave drag, which is parameterized following Lott and Miller (1997). To correct the NH winter warm biases, the SSO drag above 40 km in the model has been switched off. This results in a substantial improved simulation of the polar night jet, the polar vortex and planetary waves compared to ERA-I. The NH winter polar stratospheric biases are linked to the tropospheric jet and near surface temperature via stratosphere-troposphere coupling. Therefore, the correction of polar stratospheric biases also leads to a better simulation of the NH troposphere and surface climate.

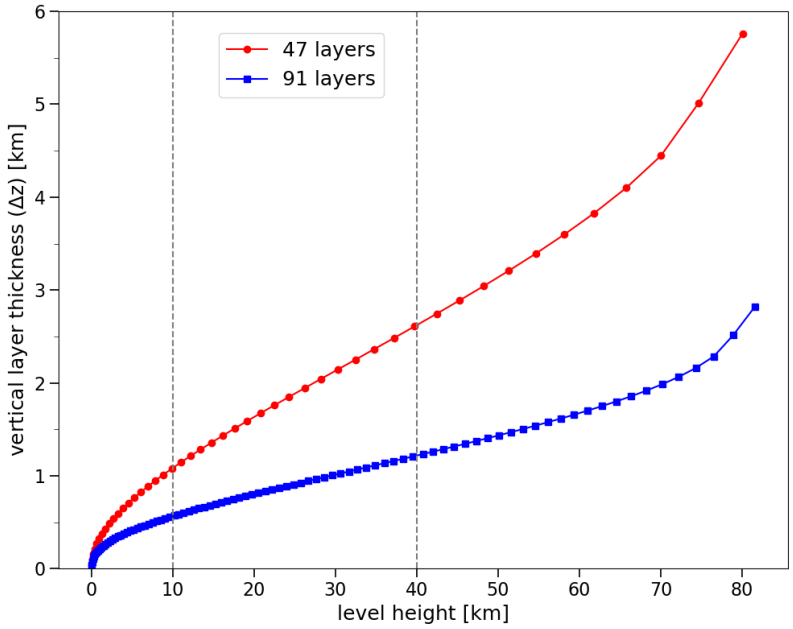

Figure 4.18– Full-level height [km] and layer thickness Δz [km] of the vertical levels of ICON-ART. The blue line denotes 47 full levels (ICON-CTL, ICON-SSO40, ICON-QBO and ICON-NONGWD) and red line denotes 91 full levels that could be used for higher vertical resolution simulations. But, in this study, for the computational cost, this configuration has not been tested.

The QBO not only dominates the tropical stratospheric variability in temperature and trace gases, but also strongly influences the polar stratosphere by modulating planetary wave propagation. However, in the current version of ICON-ART in which coarser resolutions (horizontal and vertical) are applied, the model fails to generate a QBO-like oscillation. The missing QBO-like oscillation in the tropical stratosphere is rectified by zonal wind relaxation, which suffices to study the high latitude influences of the QBO (I will examine in Chapter 5). The characterization of the biases and corrections are summarised in Table 4.2.

Table 4.2 – List of major biases or rectifications for ICON-ART AMIP-type simulations

Abbreviation	Description
ICON-CTL	(1) cold-pole in SH winter stratosphere: lack of NONGWD (2) warm-pole in NH winter stratosphere: excessive SSO gravity wave drag (3) no QBO in tropical stratosphere: lack of NONGWD and coarse vertical resolution at UTLS
ICON-SSO40	Switching off SSO drag above 40 km: (1) better simulated polar stratospheric climatology (2) tropospheric jet and tropospheric temperature, resembles NAM pattern
ICON-NONGWD	Increase NONGWD amplitude: (1) Better representation of SH winter polar stratosphere (2) Stronger westerlies in the upper stratosphere
ICON-QBO	Specifying QBO-varying wind variability by QBO-relaxation: (1) the equatorial zonal wind is consistent with ERA-I, but with smaller amplitude (2) repeats the classic Holton-Tan relationship (in Chapter 5)

The QBO simulation remains a challenge in climate models, especially when coarser resolutions are applied (Butchart et al. 2018). When using an Earth system model for longterm climate projections, it demands huge computational resources. So, it is a compromise to use coarser resolutions with several sub-grid physical parameterizations (e.g., gravity wave drag and convection). In order to better understand why the tropical stratosphere is poorly simulated, the momentum analysis and equatorial wave spectral analysis are carried out. In ERA-I, both EP flux divergence (EPFD) and residual circulation forcing contribute to the QBO phase transition, especially for the easterly to westerly phase transition. However, the forcing due to the residual circulation often tries to balance the EPFD, suggesting that forcing from the unresolved waves is particularly important. The vertical momentum transfer (vertical derivative of $\overline{u'w'}$) accounts for a large portion of the EPFD during the easterly to westerly phase transition. In ICON-CTL, the EPFD is much larger than that of ERA-I and suffers from strong interannual instead of quasi-biennial variability. The model simulated too much vertical momentum transfer. Through equatorial wave diagnostics, I identified that the simulated Kelvin waves are excessively stronger with a broader wavenumber-frequency domain. The

power spectra of $\overline{u'w'}$ also shows much larger values in the Kelvin wave domain, suggesting that the enhanced Kelvin wave propagation into the equatorial stratosphere accounts for the larger vertical momentum transfer in ICON-CTL. This could be understood as that the eastward propagating Kelvin waves not being filtered in the prevailing easterlies (Lott et al. 2014).

According to some model experiments with successful simulations of a QBO-like oscillation, some general rules are concluded: 1) a proper tuning of non-orographic gravity waves (e.g., gravity wave amplitude) and 2) the sufficient high vertical resolution at UTLS (at least 700 m). When examining different terms in the TEM momentum equation, it is found that the magnitude of GWD is too small in ICON-CTL. Figure 4.18 shows the model vertical resolution as a function of model height. At the height range 10–40 km, the model vertical resolution is greater than 10 km (red line). That is to say the ICON-CTL failed to meet the two primary requirements for QBO simulation. However, this can only be justified when the model uses higher vertical resolution (for example 91 model layers, Figure 4.18 blue line) and larger GWD, and as a consequence, the model simulates an internally generated QBO-like oscillation.

Chapter 5 Dynamical interactions between high and low latitudes

5.1 Introduction

The quasi-biennial oscillation (QBO) is characterized by the alternation of westerly and easterly zonal wind regimes in the equatorial lower and middle stratosphere (15–30 km) (Baldwin et al. 2001). The relationship between the QBO and the Northern Hemisphere (NH) winter polar vortex is often referred to as the Holton-Tan relationship (hereafter HT relationship), i.e., the equatorial westerlies (easterlies) at 50 hPa correlate with a stronger (weaker) polar vortex (Holton and Tan 1980, 1982, hereafter referred to as HT80). Both reanalysis-based studies (Dunkerton and Baldwin 1991; Lu et al. 2008; Anstey et al. 2010) and model simulations (Hamilton 1998; Yamashita et al. 2011) support such a relationship.

HT80 proposed a dynamical mechanism to explain the observed HT relationship. They hypothesized that the QBO modulates the position of the subtropical critical line (the zonal mean flow has zero velocity speed) in the lower stratosphere. Because the easterly (westerly) phase of QBO is related to northward (southward) shifts of the critical line, this corresponds to a narrowing (widening) of the width of the planetary wave guide. As a result, there is a weaker (stronger) polar vortex during the easterly (westerly) phase of QBO. But the debate still exists about the mechanism (Anstey and Shepherd 2014a).

Recent studies have emphasized the role of the equatorial zonal winds in the middle stratosphere and upper stratosphere. Based on reanalysis data and QBO-relaxation experiments, Yamashita et al. (2011) found that the meridional circulation anomalies induced by the QBO at 10 hPa are consistent with a stronger or weaker polar vortex while the

mechanism of the critical line shift influenced by QBO at 50 hPa is unclear. Based on idealized experiments with the Whole Atmosphere Community Climate Model (WACCM), Garfinkel et al. (2012) pointed out that the meridional circulation induced by equatorial zonal winds in the middle and upper stratosphere is more important than the critical line mechanism for the polar response to the QBO. Including the variability from the upper stratosphere (above ~1 hPa) (semi-annual oscillation, SAO), Pascoe et al. (2006) found that the timing of midwinter sudden warmings is advanced by about one month.

Due to the long-standing challenge for general circulation models to generate a QBO-like oscillation spontaneously, QBO-relaxation is often used to study the interactions between the QBO and the polar stratosphere. The QBO-relaxation width and height ranges are shown to be of great importance for extra-tropical responses. In Chapter 4, it is shown that the QBO-relaxation requires to set relaxation width and height range. By comparing a pair of idealized experiments with the QBO relaxation width of 8° and 15°, Hurwitz et al. (2011) found that a broader QBO corresponds to a weaker Arctic vortex with enhanced total ozone at high latitudes, which is further confirmed in Hansen et al. (2013). Gray et al. (2001) suggested that due to the deep structure of the stratospheric polar vortex, the equatorial upper stratosphere is also important for polar stratospheric responses. They found the existence of a HT relationship when the equatorial QBO was relaxed to a height range of 16–58 km and no HT relationship when the equatorial QBO was relaxed to a height range of 16–32 km. Subsequent idealized experiments (Gray 2003; Pascoe et al. 2006) also confirm the strong sensitivity of the polar stratosphere to the upper equatorial stratosphere.

This chapter aims to investigate the sensitivity of the polar stratosphere to the height range of the equatorial zonal wind (QBO and SAO) in ICON-ART, and is organized as follows. Section 5.2 presents the HT relationship in an ICON-ART AMIP-type simulation with QBO relaxation (ICON-QBO, see Chapter 4) as compared to ERA-Interim. Then, Section 5.3 introduces an idealized experimental design, where the equatorial zonal winds are relaxed to a different phase or height range of the specified wind profiles that are derived from ERA-I. Section 5.4 examines the sensitivity of polar stratospheric responses to the specified QBO phases and QBO relaxation height ranges. Finally, Section 5.5 gives the summary and conclusions.

5.2 The HT relationship: observation and simulation

The HT relationship is one of the prominent connections between low latitudes and high latitudes. Here, I revisit the HT relationship in ICON-ART and make a comparison to this relationship in ERA-Interim (ERA-I). The HT relationship is displayed as the composite of wintertime (December-January-February, DJF) zonal mean zonal wind (ZMZW) and temperature (ZMT) over the period 1979–2008.

The ICON-ART is not able to internally generate a QBO-like oscillation, and the equatorial zonal wind is biased with unconstrained easterlies in the middle atmosphere (see Chapter 4). In order to investigate the HT relationship in the model, the equatorial zonal wind is relaxed to a monthly mean reference wind profile, where the wind profile is the zonally averaged wind over 5° S to 5° N of ERA-I. The relaxation procedure is similar to Matthes et al. (2010) and has been introduced in Chapter 4, where the ICON-ART with QBO-relaxation is denoted as ICON-QBO.

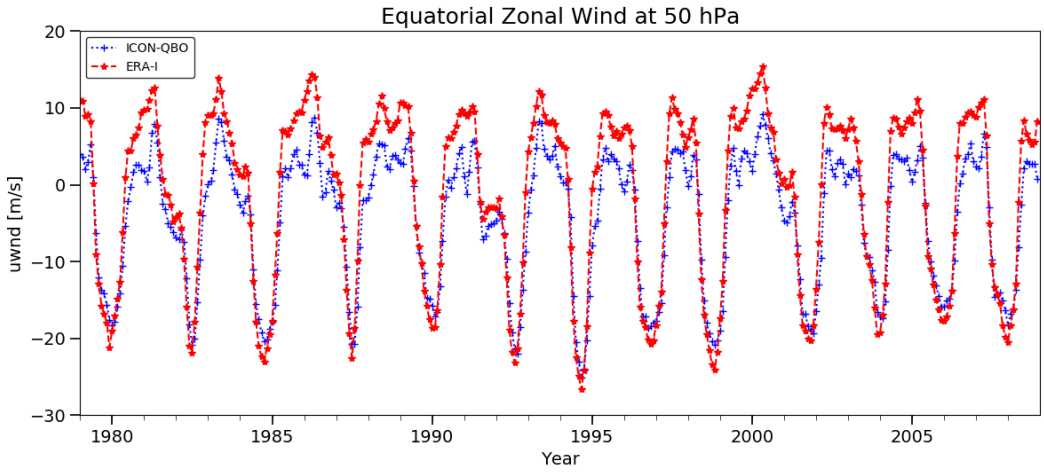

Figure 5.1– Timeseries of monthly mean equatorial zonal wind at 50 hPa over the period 1979–2008 for ERA-I (red line) and ICON-QBO (blue line).

5.2.1 QBO phase definition

The timeseries of equatorial zonal mean zonal wind (Ueq) at 50 hPa (Ueq50) is shown in Figure 5.1. Basically, the modelled Ueq50 (ICON-QBO) during the months of the easterly phase of QBO is comparable to the observed Ueq50 (ERA-I), while during the months of the westerly phase of QBO, the amplitude of the modelled Ueq50 is weaker than the amplitude of the

observed Ueq50 (because soft QBO relaxation is applied). In order to be consistent with previous studies (Holton and Tan 1980; Lu et al. 2014), the QBO phase is defined based on wintertime mean Ueq50, i.e., the easterly phase of QBO (eQBO) is defined as Ueq50 < -2m/s and the westerly phase of QBO (wQBO) is defined as Ueq50 > 0 m/s, respectively. According to the definition, the wQBO and eQBO winters are selected, and the composite of the meteorological fields for wQBO and eQBO is calculated. The selected wQBO winters in ICON-QBO are less than that in ERA-I, which is due to the weaker Ueq50 in ICON-QBO.

5.2.2 Comparison of the HT relationship in ERA-I and ICON-QBO

Figure 5.2 shows the wintertime ZMZW composite difference. For ERA-I, the observed ZMZW difference shows dipole anomalies in the tropical regions with a significant westerly anomaly in the lower stratosphere centred at 50 hPa (the level at which the QBO phase is defined) and an easterly anomaly in the middle stratosphere (around 10 hPa) (Figure 5.2a) (because that the QBO phase is descending at a rate of ~1–2 km/month). Away from the tropical regions, the differences gradually decrease. At the NH polar latitudes, associated with the westerly anomaly in the lower equatorial stratosphere, the polar night jet is significantly enhanced throughout the stratosphere (100–5 hPa) and the zonal wind deviation reaches 8 m/s at ~10 hPa, which is consistent with previous studies (Dunkerton and Baldwin 1991; Yamashita et al. 2011). This is typical of the HT relationship, i.e., the wQBO (eQBO) corresponds to a stronger (weaker) winter polar stratospheric vortex. For ICON-QBO, the composite ZMZW difference is comparable to that of ERA-I in the tropical stratosphere and NH polar latitudes (Figure 5.2b), except that the easterly anomaly in the upper stratosphere extends up to ~1 hPa (only up to ~5 hPa in ERA-I). In the polar stratosphere, the westerly anomaly in the lower stratosphere also corresponds to a stronger westerly jet through the depth of the stratosphere, suggesting the QBO relaxation largely reproduced the observed HT relationship (ERA-I). But, note the polar night jet responses are weaker (4 m/s in ICON-QBO vs. 8 m/s in ERA-I) and not significant (Figure 5.2a vs. Figure 5.2b). The cause for this might be that stronger polar stratospheric wave activities are simulated in NH winter (see Chapter 4, Figure 4.7b).

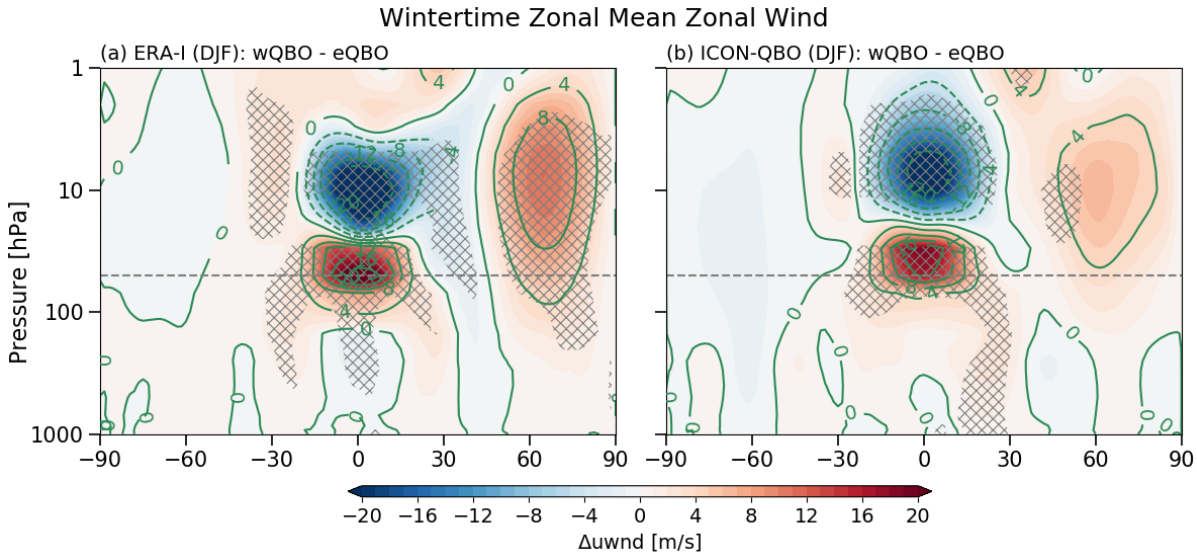

Figure 5.2– Composite differences between wQBO and eQBO for wintertime (DJF) zonal mean zonal wind: (a) ERA-I; (b) ICON-QBO. Stippling denotes the composite differences that are significant at the 95% confidence level according to the Student's t-test. The black dashed lines indicate the 50 hPa pressure level (phase definition of QBO).

Figure 5.3 shows the composite ZMT difference. For ERA-I, in the tropical stratosphere, the temperature anomaly shows tripole structure vertically with warming in the lower stratosphere, cooling in the middle stratosphere and warming again in the upper stratosphere. The triple structure is consistent with the wind anomalies in Figure 5.2a. According to thermal wind balance, for example, the maximum westerly at 50 hPa is related to positive wind shear, resulting in a warm anomaly in the lower stratosphere (Figure 5.3a). In the mid-latitudes (30° N–60° N), there is a dipole anomaly pattern with warm anomaly at levels of 100–10 hPa, and cold anomaly in the upper stratosphere (> 10 hPa). This dipole anomaly pattern is maintained by the QBO-induced meridional circulation, with upwelling or downwelling at the equator and an opposite motion at the subtropics (Baldwin et al. 2001). The dipole temperature anomalies also appear in the polar stratosphere, displaying a ~2 K warming in the upper stratosphere (> 10 hPa) and a ~2 K cooling at the levels of 100–10 hPa. Figure 5.3a together with Figure 5.2a clearly demonstrate the classic HT relationship, i.e., the wQBO (at 50 hPa) corresponds to a stronger and colder winter polar vortex and the eQBO (at 50 hPa) corresponds to a weaker and warmer winter polar vortex. The composite ZMT difference in ICON-QBO largely resembles the observation (Figure 5.3a vs. Figure 5.3b). For the polar stratosphere, the HT relationship is slightly less significant and weaker in magnitude (similar to the polar night jet in Figure 5.2b).

The composite differences of ZMZW and ZMT demonstrate the ICON-QBO is able to reproduce the HT relationship when the QBO-varying wind profiles are imposed.

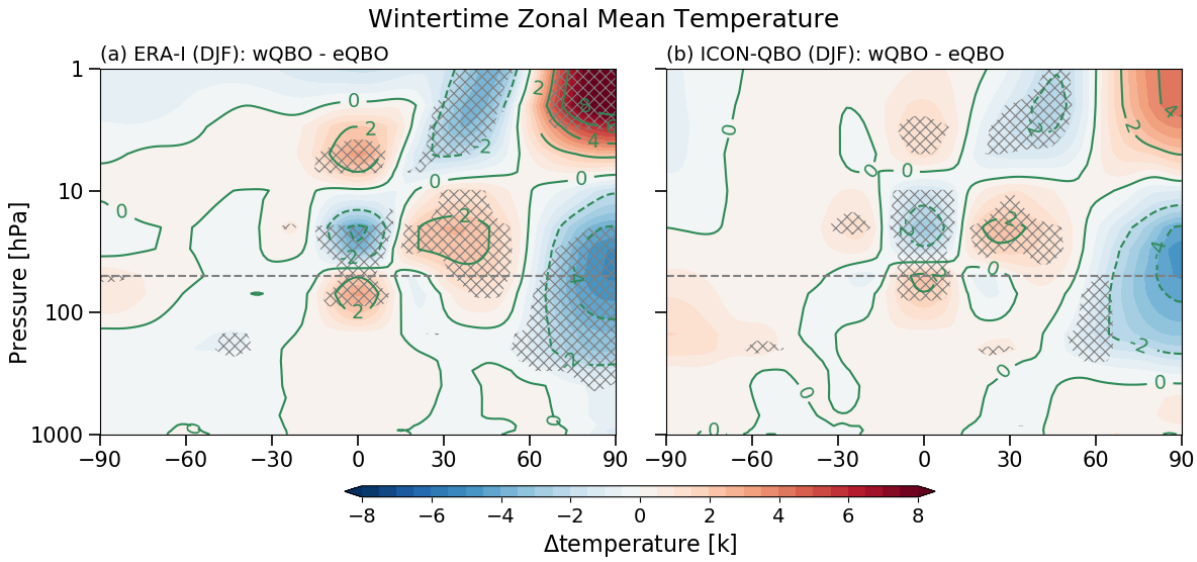

Figure 5.3– Composite differences between wQBO and eQBO for wintertime (DJF) zonal mean temperature: (a) ERA-I; (b) ICON-QBO. Stippling denotes the composite differences that are significant at the 95% confidence level according to the Student's t-test. The black dashed lines indicate 50 hPa pressure level (phase definition of QBO).

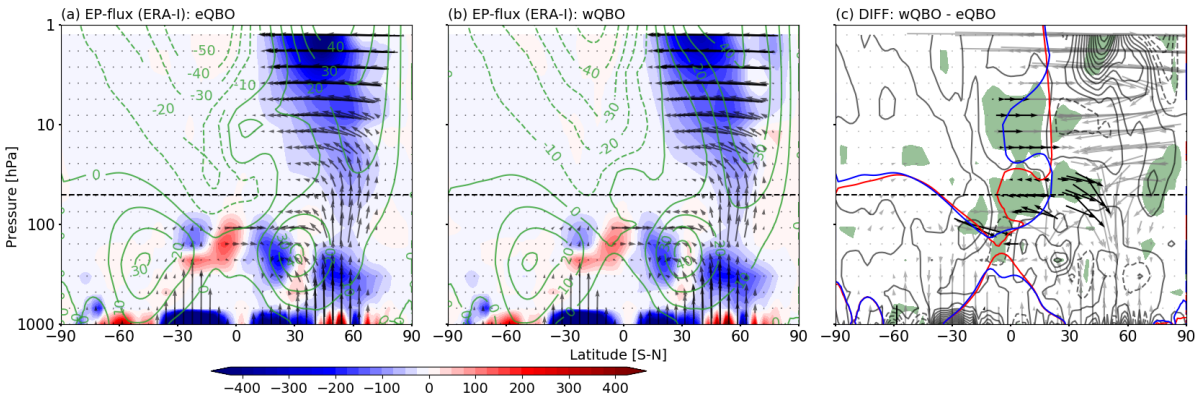

Figure 5.4– Composite of EP flux vectors (arrows) and the EP flux divergence (red and blue shadings), and zonal mean zonal wind (green contour lines) for (a) eQBO and (b) wQBO. For (c), the composite differences of EP flux (grey vectors, black vectors denote the difference are significant at the 90% confidence level), EP flux divergence (grey contour lines, the green shaded area denotes the difference are significant at the 90% confidence level). The red and blue lines in (c) indicate the zero-wind speed of the zonal mean zonal wind (critical line) for wQBO (red) and eQBO (blue).

The modulation of the extra-tropical planetary waveguide is commonly used to explain the dynamical mechanism of the HT relationship (Lu et al. 2014; Holton and Tan 1980; Dunkerton and Baldwin 1991). Here, the EP flux and its divergence (EPFD), which measures planetary wave propagation and wave forcing, are used to diagnose the planetary wave activities. Based on ERA-I data, Figure 5.4 shows the EP flux vectors and EPFD for wQBO (Figure 5.4a), eQBO (Figure 5.4b) and their composite differences (Figure 5.4c). The EP flux is calculated using monthly mean data and the quasi-geostrophic approximation formula (see Appendix A), which is sufficient for the diagnostic of extra-tropical stratospheric wave-mean flow interaction (Martineau et al. 2017). In Figure 5.4a, the climatological planetary waves in NH mid-latitudes propagate vertically from the troposphere into the stratosphere (indicated by black vectors). Some of the planetary waves propagate towards the equator in the upper troposphere, leading to EP flux convergence at the southern flank of the tropospheric jet; the others continue to propagate vertically, and gradually turn towards the equator (strong polar night jet services as a turning level), which results in an EP flux convergence in the upper stratosphere and zonal flow deceleration. The two ways of planetary wave propagation are also displayed in Figure 2.5 (see Chapter 2). In the Southern Hemisphere (SH, austral summer), planetary waves propagate upward from tropospheric sources, then stall in the lower stratosphere when encountering the zero-wind line, which is the critical line for stationary planetary waves. This is because when the group velocity vanishes, the wave propagation becomes extremely slow (see Salby 2012, P. 453), resulting in wave breaking and absorption. Without the disturbance from the planetary waves, the summer stratosphere is very stable. This also demonstrates that planetary waves are not able to propagate across critical lines (Charney and Drazin 1961). During the wQBO, in the lower stratosphere (~50 hPa), the composite position of subtropical critical line is located at around 25° N (Figure 5.4c, blue line); while in the middle stratosphere (~10 hPa), the subtropical critical line is located at around 6° S (Figure 5.4c, blue line). During the eQBO, the position of subtropical critical lines is clearly reversed to that in the wQBO (Figure 5.4c, red line vs. blue line). The subtropical critical line moves towards the equator in the lower stratosphere, and towards the NH in the middle stratosphere (Figure 5.4c, red line). The composite differences in EP flux vectors and EPFD in Figure 5.4c indicate that the wQBO is associated with anomalous equatorward wave propagation in the lower equatorial stratosphere (~50 hPa), and poleward and downward wave propagation at subtropical regions. Accordingly, there is EP flux convergence anomaly in the lower equatorial stratosphere and an

EP flux divergence anomaly in the lower subtropical stratosphere. At ~10 hPa, on the contrary, there is anomalous positive EP flux vector at equatorial regions which is associated with an EP flux divergence anomaly in equatorial regions and an EP flux convergence anomaly in subtropical regions. Note that the anomalous equatorward stationary wave propagation is exactly bounded by the zero-wind lines of wQBO (blue) and eQBO (red) around 50 hPa, suggesting the important role of the subtropical critical line in controlling planetary wave propagation.

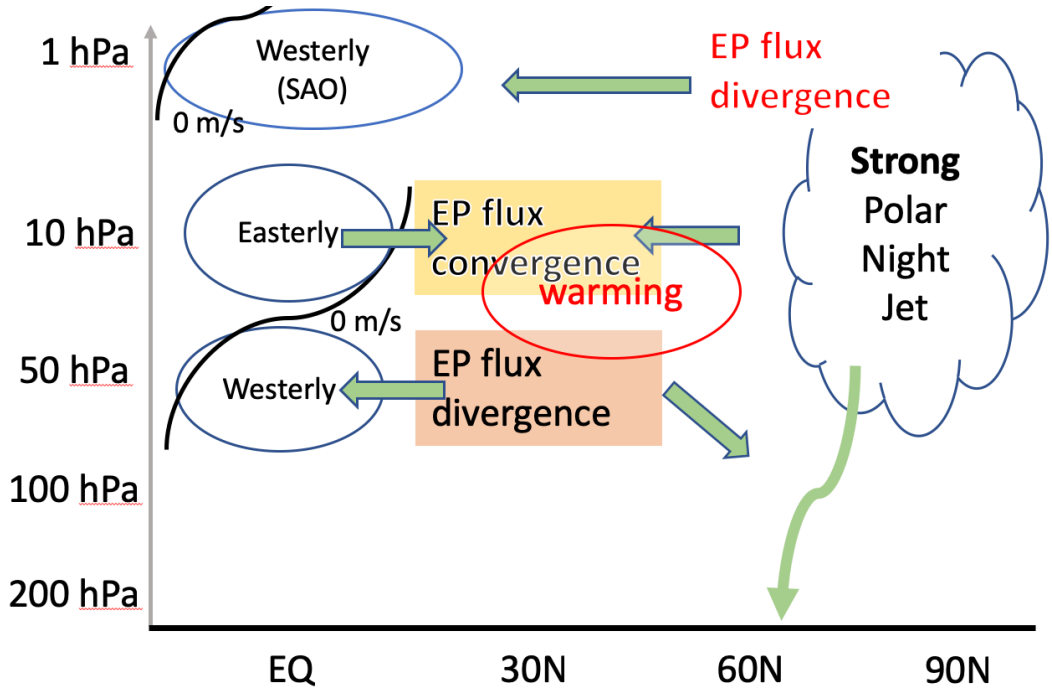

Figure 5.5– Snapshot for a particular QBO phase configuration (adapted from Yamashita et al. (2011)) (presuming that the QBO is in the westerly phase at 50 hPa). Green vectors denote the direction of planetary wave propagation. The role of upper stratospheric SAO will be discussed in the following section.

According to the "downward control" principle (Haynes et al. 1991), the mid-latitude EP flux convergence anomaly in the middle stratosphere is related to an increase of downwelling, resulting in a warm anomaly (Figure 5.3a). Furthermore, the warmer middle stratosphere increases the temperature gradient between the pole and mid-latitudes, resulting in a stronger polar night jet. Therefore, QBO winds in the middle stratosphere also contribute to polar stratospheric variability, which has been emphasized in recent studies (Yamashita et al. 2011; Garfinkel et al. 2012; Lu et al. 2014). Based on the EP flux diagnostic of ERA-I data, a schematic illustration of the low and high latitude interactions is summarised in Figure 5.5. In the lower stratosphere, the westerly phase of QBO (at 50 hPa) corresponds to an equatorward

shift of the critical line, EP flux divergence in the mid-latitudes and downward planetary wave propagation at around 60° N; in the middle stratosphere, the westerly phase of QBO (at 50 hPa) corresponds to a poleward shift of the critical line, EP flux convergence and warming at the mid-latitudes, resulting in a strengthening of the temperature gradient between the pole and the midlatitudes. The role of upper equatorial westerlies (SAO) will be discussed in the following section.

5.3 Idealized experimental design

The high-latitude influence of the lower-stratospheric QBO is well documented and denoted as HT relationship (also in above analysis). This HT relationship is commonly explained by the modulation of the latitudinal width of planetary wave propagation in the lower stratosphere (e.g., Anstey et al. (2014b)). However, the critical line position in the middle-to-upper stratosphere is often opposite to that of the lower stratosphere (see Figure 5.4c), so it is still unclear whether the middle-to-upper stratospheric zonal winds have played a role in the HT relationship. Here, the high-latitude influence from the equatorial stratosphere is revisited in a set of idealized experiments. The idealized experiments use wQBO or eQBO wind profiles in the chemistry-climate model ICON-ART.

5.3.1 Composite of wQBO and eQBO wind profiles

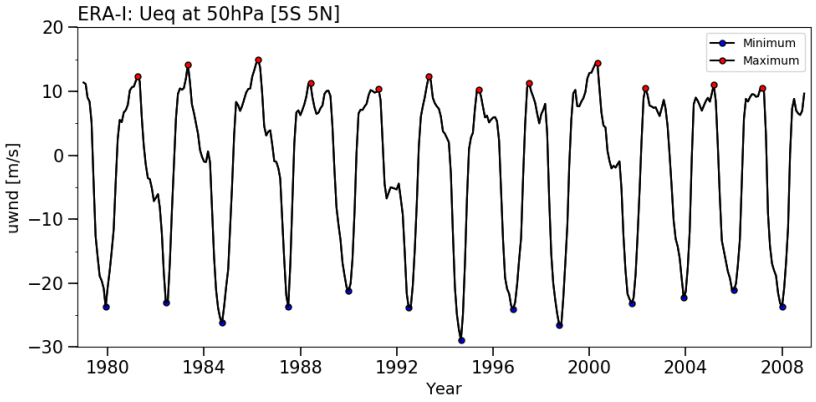

Figure 5.6– Time series of equatorial zonal wind (Ueq) at 50 hPa obtained from ERA-I. For each QBO cycle, the months corresponding to maximum (red dots) and minimum (blue dots) are selected to construct composites of wQBO and eQBO wind profiles.

The wQBO or eQBO wind profiles are from the ERA-I data, which are composite profiles with respect to the maximum and minimum of each QBO cycle at 50 hPa. Figure 5.6 shows monthly Ueq50 for 1979–2008 with the maximum and minimum of each QBO cycle marked as red and blue dots. The magnitude of the easterly minima is stronger than the magnitude of the westerly maxima.

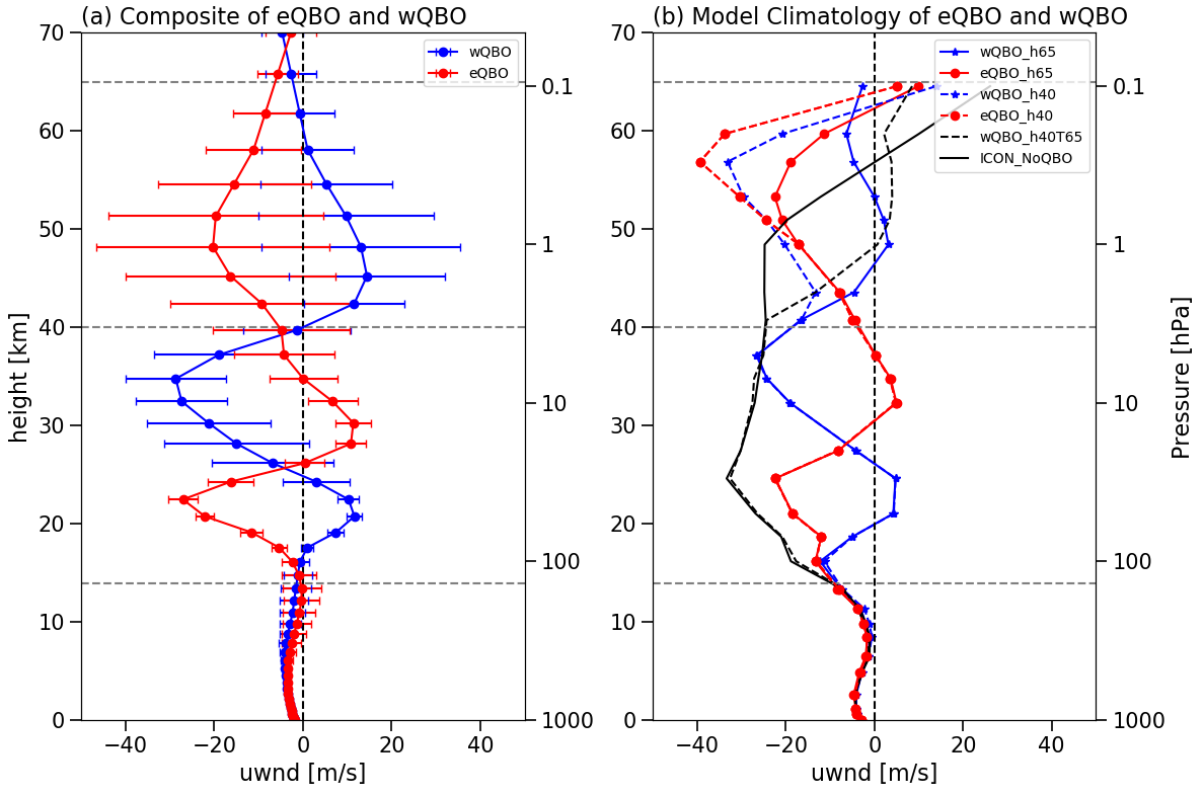

Figure 5.7– Wind profiles of equatorial zonal wind (Ueq). (a) shows composite profiles of the eQBO and wQBO based on the minima and maxima of each QBO cycle (see Figure 5.6). The eQBO and wQBO wind profiles are denoted as red lines and blue lines, respectively. The standard deviation of wQBO (12 cases) and eQBO (13 cases) are overlaid on the lines. The grey dashed horizontal lines indicate the relaxation depths (14–40 km vs. 14–65 km for the ICON-ART idealized experiments. (b) shows the 35-year annual mean equatorial zonal wind for eQBO_h40 (dashed red line), eQBO_h65 (solid red line), wQBO_h40 (dashed blue line) and wQBO_h65 (solid blue line), wQBO_h40T65 (dashed black line) and ICON_NoQBO (solid black line).

Based on the maxima of Ueq50 (wQBO) and minima of Ueq50 (eQBO), the composite wind profiles for wQBO and eQBO are shown in Figure 5.7a. Here, the Ueq are from 91 model levels of ERA-I (L91), extending from the surface to ~80 km. Note that even though the ERA-I upper stratospheric zonal winds are used, it does not necessarily mean they are realistic (Polichtchouk et al. 2017). The wQBO wind profile (blue line) peaks at ~21 km (50 hPa), then

turns to minimum at around 35 km and a maximum at around 45 km; the eQBO wind profile (red line) is generally opposite to that of wQBO. Therefore, the Ueq in the upper stratosphere (above 40 km) is in-phase with the lower stratosphere during the maximum or minimum Ueq50. Note that the upper stratospheric Ueq have a strong interannual variability. The wind patterns related to QBO are well-known (Baldwin et al. 2001), especially in the lower-to-middle stratosphere. The upper stratosphere or lower mesosphere is dominated by the semi-annual oscillation (SAO), which manifest itself as the twice-year wind reversal. The period of the QBO has a tendency to synchronize with the SAO, i.e., the wQBO in the lower stratosphere always corresponds to a westerly phase of SAO (Tung et al. 2008; Liu et al. 2011), which is also demonstrated in Figure 5.7a.

5.3.2 Idealized experiments

To investigate dynamical connections between high and low latitudes, a set of idealized experiments are conducted, in which the Ueq in the model is relaxed to the imposed wind profiles. Specifically, the model is forced by eQBO and wQBO composite wind profiles (Figure 5.7a) with varying relaxation depths, i.e., 14–65 km and 14–40 km (Figure 5.7a, dashed lines), respectively. The experiments are idealized in aspects of 1) perpetual wQBO or eQBO wind profile (annual-invariant) is used instead of a seasonally varying QBO wind profile; 2) a model run without an internally generated QBO. The height level 40 km is used to isolate the "upper stratosphere" from the lower QBO wind structure (Figure 5.7a), which is also consistent with Gray (2003). Therefore, considering relaxation depths and QBO phases, four experiments are conducted and denoted as wQBO_h65, wQBO_h40, eQBO_h65 and eQBO_h40. The settings of the four experiments are explained bellow,

– wQBO_h65: the Ueq in the model are relaxed to the wQBO composite wind profile (Figure 5.7a, blue line) with a relaxation height range from 14 km to 65 km;

– wQBO_h40: the Ueq in the model are relaxed to the wQBO composite wind profile (Figure 5.7a, blue line) with a relaxation height range from 14 km to 40 km, and above 40 km, there is no relaxation;

– eQBO_h65: the Ueq in the model are relaxed to the eQBO composite wind profile (Figure 5.7a, red line) with a relaxation height range from 14 km to 65 km;

– eQBO_h40: the Ueq in the model are relaxed to the eQBO composite wind profile (Figure 5.7a, red line) with a relaxation height range from 14 km to 40 km, and above 40 km, there is no relaxation.

Furthermore, the four experiments are supplemented by two experiments.

– wQBO_h40T65: the Ueq in the model is relaxed to the wQBO composite wind profile (Figure 5.7a, blue line) with a relaxation height range from 40 km to 65 km, and outside the region, there is no relaxation. This experiment tries to highlight the role of upper stratosphere.

– ICON_NoQBO: no QBO relaxation is applied.

Except for the relaxation depth, the relaxation parameters are the same as the ICON-QBO with a relaxation width of 44º from 22 ºS to 22º N and a relaxation frequency of 1/10 days^{-1}. All experiments use a timeslice integration strategy with trace gases and boundary conditions of the year 2000 (see Chapter 3) and integration time of 37 years.

5.3.3 Modelled equatorial zonal wind profiles

Figure 5.7b shows modelled Ueq profiles that are presented as 35-year annual mean (the first 2 years are ignored). The modelled Ueq in wQBO_h65 (solid blue) and wQBO_h40 (dashed blue) remain the same below ~40 km, then branch off above 40 km with that Ueq are weak westerlies in wQBO_h65 and even strong easterlies in wQBO_h40 (solid blue vs. dashed blue). This is due to the lack of non-orographic gravity wave drag as explained in Chapter 4. Similarly, the modelled Ueq in eQBO_h65 and eQBO_h40 also remain the same below ~48 km, then branch off above ~48 km with a strong westerly anomaly in eQBO_h65 compared to that in eQBO_h40 (solid red vs. dashed red). The wind profiles in wQBO_h40T65 and ICON_NoQBO are nearly the same below 40 km, and then branch off above 40 km with a strong westerly anomaly in wQBO_h40T65 compared to that in ICON_NoQBO (dashed black vs. solid black). Therefore, generally, the modelled Ueq profiles are comparable to the imposed composite wind profiles below ~40 km, and the modelled westerlies are much weaker while the easterlies are much stronger than the imposed ones above ~40 km (Figure 5.7a vs. Figure 5.7b). In the following section, the extra-tropical responses to the different Ueq configurations are displayed. The circulation responses to the relaxation depths and QBO phases are emphasized.

5.4 Responses of polar stratosphere to the perpetual w/eQBO wind profiles

The imposed equatorial wind profiles serve as boundary conditions, which are important for polar stratospheric circulations. The results are presented as the differences between the mean state of the four experiments. The calculation of the differences is done following Table 5.2, which emphasize the role of the relaxation depths or QBO phases.

Table 5.1 – The model results are presented as the differences between the run with relaxation height range of h40 (14–40 km) and h65 (14–65 km), and the differences between the run with relaxation QBO phases (eQBO and wQBO). The following lists the definition of the differences.

(1) Difference: wQBO_h65 – wQBO_h40 Both runs are in westerly phase of QBO, but differ in relaxation height range (14–65 km vs. 14–40 km)	**(2) Difference: eQBO_h65 – eQBO_h40** Both runs are in easterly phase of QBO, but differ in relaxation heights (14–65 km vs. 14–40 km)
(3) Difference: wQBO_h65 – eQBO_h65 Both runs have the same relaxation depth (14–65 km), but differ in QBO phases (wQBO vs. eQBO)	**(4) Difference: wQBO_h40 – eQBO_h40** Both runs have the same relaxation depth (14–40 km), but differ in QBO phases (wQBO vs. eQBO)

5.4.1 NH wintertime circulation

The wintertime ZMZW differences are presented in Figure 5.8a–d (presentation follows Table 5.2). With a high relaxation depth, compared to wQBO_h40, wQBO_h65 has a strong westerly anomaly in the tropical upper stratosphere with a wind deviation >20 m/s (Figure 5.8a). This is accompanied by a significant stronger NH polar night jet from ~100 hPa to 1 hPa (note a moderate easterly anomaly in the middle stratosphere). Compared to eQBO_h40, a strong westerly anomaly in the tropical upper stratosphere is also found in eQBO_h65, which also coincides with a significant stronger NH polar night jet from ~100 hPa to 1 hPa (a moderate

easterly anomaly in the middle stratosphere) (Figure 5.8b). This indicates that the upper stratospheric westerly anomaly in wQBO_h65 and eQBO_h65 play similar roles for NH polar stratospheric responses. With a high relaxation depth (14–65 km), the ZMZW differences between wQBO_h65 and eQBO_h65 show tripole anomalies in the equatorial stratosphere with a westerly anomaly overlying a dipole wind anomaly structure (Figure 5.8c). The NH polar night jet is slightly stronger in wQBO_h65 with similar magnitude as in Figure 5.2b, but it is not significant. With a low relaxation depth (14–40 km), the zonal wind difference largely resembles that of high relaxation depth (Figure 5.8c vs. Figure 5.8d). This indicates the HT relationship is not sensitive to equatorial upper stratosphere.

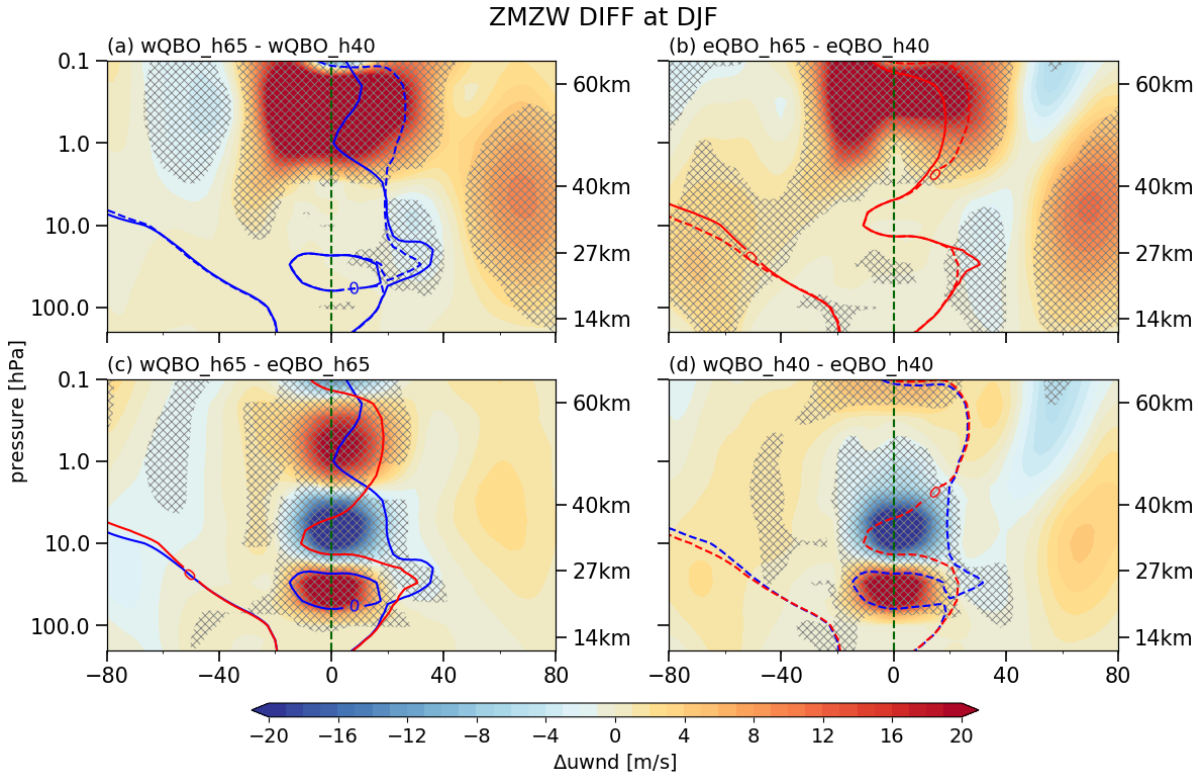

Figure 5.8– Latitude and height cross-section of zonal mean zonal wind (ZMZW) differences for DJF (December-January-February) for (a) wQBO_h65 – wQBO_h40; (b) eQBO_h65 – eQBO_h40; (c) wQBO_h65 – eQBO_h65; (d) wQBO_h40 – eQBO_h40. Stippling denotes the differences that are significant at the 95% confidence level. The zero wind contours (0 m/s) for the four experiments are highlighted with solid blue lines for wQBO_h65, dashed blue lines for wQBO_h40, solid red lines for eQBO_h65 and dashed red lines for eQBO_h40.

The wintertime ZMT differences are shown in Figure 5.9. A tropical westerly anomaly (above 40 km) in wQBO_h65 (Figure 5.9a) is related to a meridional dipole anomaly from 10 hPa to 0.5 hPa with a significant warming and cooling in the mid-latitudes (30° N–60° N) (Figure

5.9a). And near 0.1 hPa, there is also a meridional dipole, but the temperature anomaly is opposite to the levels of 10–0.5 hPa. In the polar stratosphere, wQBO_h65 corresponds to a significant warming in the upper stratosphere and a cooling in the lower stratosphere. In general, the extra-tropical responses to a tropical westerly anomaly (above 40 km) in eQBO_h65 is similar to wQBO_h65 (Figure 5.9a vs. Figure 5.9b). The ZMT difference in low relaxation height shows cold and warm dipole in the polar stratosphere (Figure 5.9d), which differs from that of high relaxation height (Figure 5.9d). The cold and warm dipole is very close to the observed HT relationship (shown in Figure 5.3a), thus the HT relationship is better represented, when there is no upper equatorial wind relaxation.

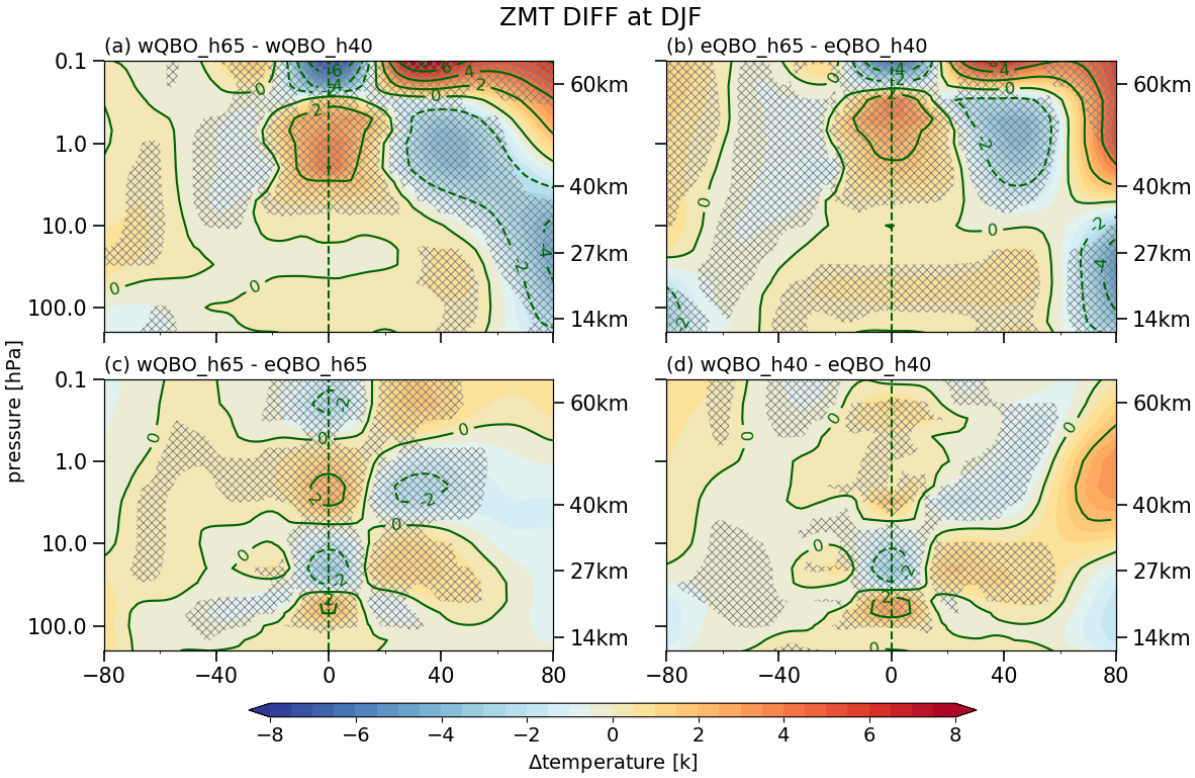

Figure 5.9– The same as Figure 5.8, but for zonal mean temperature (ZMT).

Figure 5.10 and Figure 5.11 show the differences of the meridional component of the EP flux vector (Fphi) and EPFD, respectively. The climatology of the EP flux vector is characterized by vertical propagation from the troposphere into the stratosphere, and by an equatorward propagation in the upper stratosphere (green arrows), indicating that the planetary waves propagate both vertically and horizontally. Comparing the differences of the relaxation depths (Figure 5.10a and Figure 5.10b), we see that both wQBO_h65 and eQBO_h65 have stronger equatorward propagation. Thus, fewer planetary waves are directed to the NH polar

stratosphere. The strong equatorward propagation of planetary waves is consistent with an equatorward shift of the critical line in wQBO_h65 and eQBO_h65 in the upper stratosphere (Figure 5.8a–b, blue solid and red solid lines) (compared to wQBO_h40 and eQBO_h40). Note that the negative Fphi anomalies in wQBO_h65 and eQBO_h65 are very broad with a latitudinal range from ~0 to 60º N. The cause for this might be that in the upper stratosphere, the planetary waves are dominated by meridional propagation (very small vertical propagation) (Figure 5.10, green arrows). Correspondingly, the EPFD differences show EPFD positive anomalies in wQBO_h65 and eQBO_h65 above ~10 hPa and at 60° N (Figure 5.11a and 5.11b), leading to a stronger polar night jet shown in Figure 5.8a and Figure 5.8b. The Fphi differences between wQBO_h40/65 and eQBO_h40/65 are shown in Figure 5.10c and Figure 5.10d. Both with high and low relaxation depths, the wQBO_h40/65 shows a significant poleward wave propagation in the tropical stratosphere (~10 hPa) and equatorward wave propagation in the mid-latitude stratosphere, which corresponds to EP flux convergence anomaly at ~40° N and 10 hPa (blue, Figure 5.11c and Figure 5.11d). The "downward control" principle further suggests that the EP flux convergence anomaly induces a downwelling motion below, which is consistent with the warm anomaly in the middle stratosphere in Figure 5.9c–d. Note this EP flux convergence anomaly is consistent with those in Figure 5.4c and Figure 5.5.

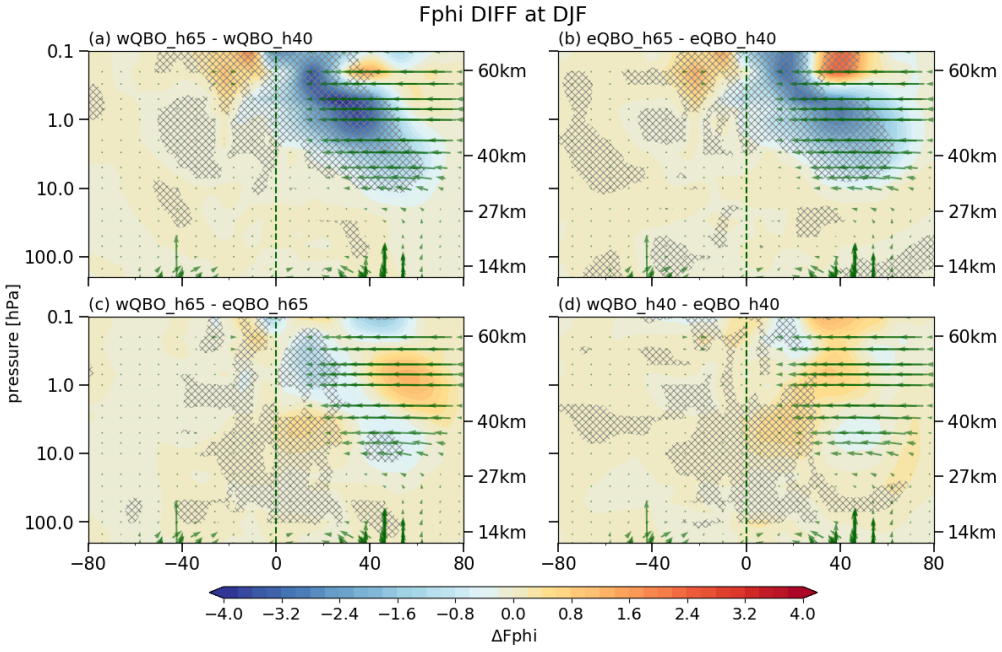

Figure 5.10– The same as Figure 5.9, but for meridional component of EP flux vector (Fphi). The green vectors denote the DJF mean climatology EP flux vector.

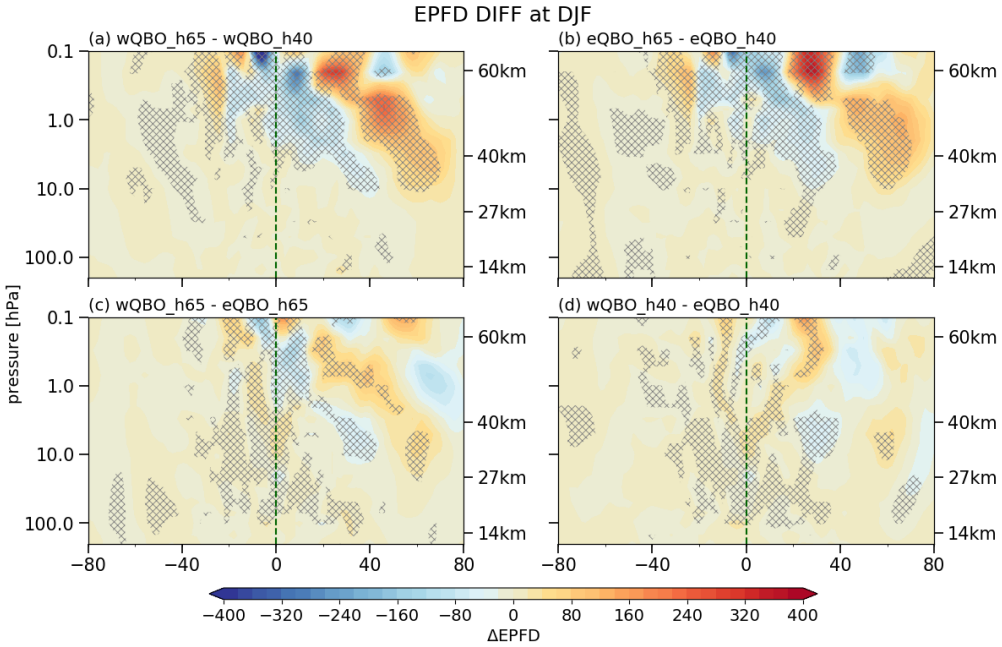

Figure 5.11– The same as Figure 5.9, but for EP flux divergence (EPFD).

5.4.2 Polar cap temperature and polar night jet

The seasonal evolution of polar stratospheric responses to the imposed Ueq is examined here. Figure 5.12 shows time-height cross-sections of the NH polar cap temperature as the differences from the relaxation depths (14–40 km or 14–65 km) and the relaxation QBO phases (wQBO or eQBO). The results are presented in accordance with Table 5.2. Compared to wQBO_h40, with a westerly anomaly in the upper stratosphere and in the tropics, wQBO_h65 has a significant cold anomaly during mid-winter (January), which is followed by a significant warm anomaly during late winter (February–March) (Figure 5.12a). The cold anomaly appears firstly in the upper stratosphere during late December, then propagates down to the lower stratosphere and lasts into March. The maximum cooling (~10 K) is found during January at levels of 100–1 hPa. Compared to eQBO_h40, eQBO_h65 has significant cooling in the lower stratosphere and warming in the upper stratosphere (mainly in January, Figure 5.12b). Both wQBO_h65 and eQBO_h65 have a westerly anomaly in the upper stratosphere and tropics, which both correspond to a colder polar stratosphere with a small difference in the seasonal evolution (Figure 5.12a vs. Figure 5.12b). The second row shows the differences that are related to relaxation QBO phases. Compared to eQBO_h65, wQBO_h65 corresponds to a significant cold anomaly during mid-winter (mid-January) from ~70 hPa to 1 hPa (Figure 5.12c). With a low relaxation height range (14–40 km), the difference between wQBO_h40

and eQBO_h40 shows significant cooling in early winter (~December) from ~100 hPa to 10 hPa, which is different from the high relaxation height range (14–65 km) (mid-winter vs. early winter, Figure 5.12c vs. 5.12d), implying that with the influence of the equatorial upper stratosphere, the HT relationship is delayed.

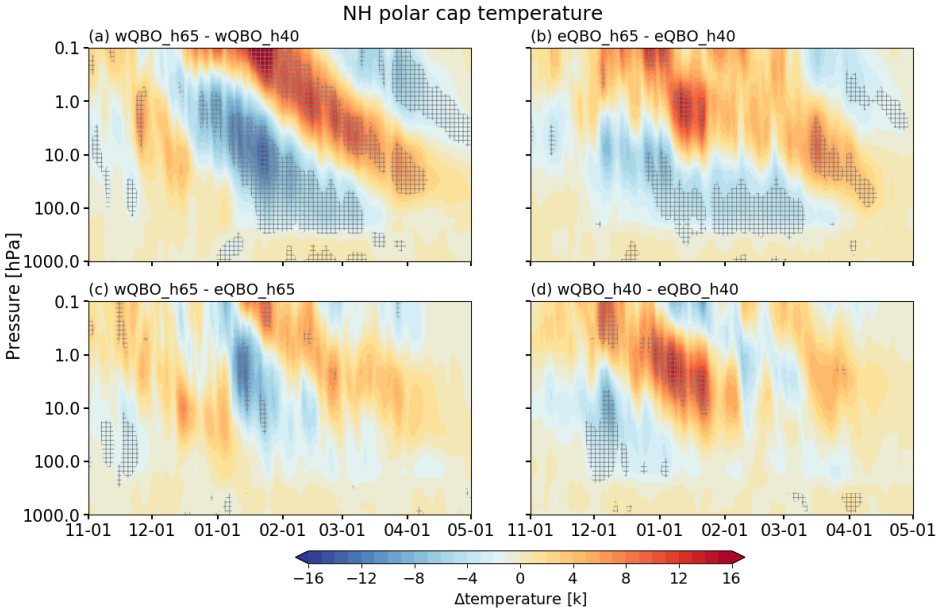

Figure 5.12– Time-height cross-section of evolution of NH polar cap temperature difference from 01/Nov to 01/May for (a), wQBO_h65 – wQBO_h40; (b) eQBO_h65 – eQBO_h40; (c), wQBO_h65 – eQBO_h65;(d), wQBO_h40 – eQBO_h40. Stippling denotes the difference that are significant at the 95% confidence level.

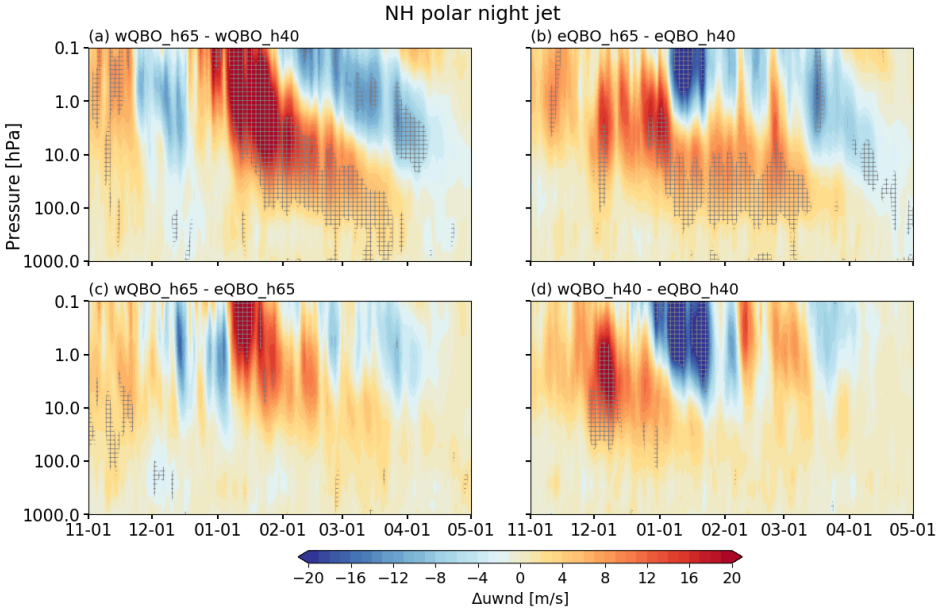

Figure 5.13– The same as Figure 5.12 but for NH polar night jet (zonal winds at 60° N).

Figure 5.13 shows the seasonal evolution of the polar night jet. The differences in polar cap temperature and polar night jet are consistent with each other (opposite sign), i.e., a colder polar vortex is accompanied by a stronger polar night jet (zonal winds at 60° N).

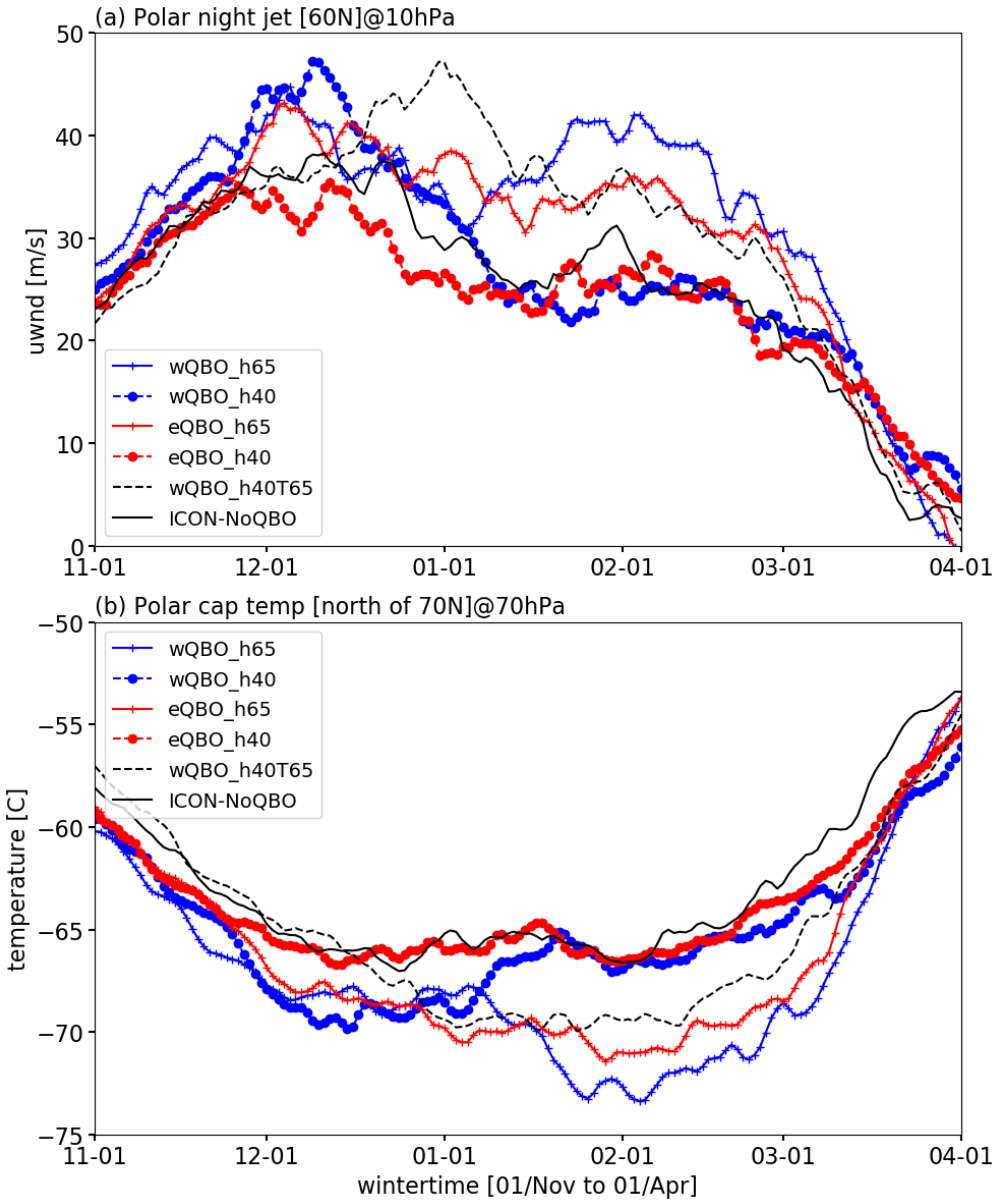

Figure 5.14– Wintertime evolution of the NH polar night jet (60° N and 10 hPa) and the NH polar cap temperature (area weighted average poleward of 70° N at 70 hPa) for experiments: wQBO_h40 (blue-dashed lines), wQBO_h65 (blue-solid lines), eQBO_h40 (red-dashed lines), eQBO_h65 (red-solid lines), wQBO_h40T65 (black-dashed lines) and ICON-NoQBO (black-solid lines).

Figure 5.14 shows the evolution of the polar night jet (defined as zonal wind at 60° N and 10 hPa) and the polar cap temperature at 70 hPa (defined as weighted average of 70° N to pole) for the six idealized experiments. Firstly, considering the relaxation depth, compared to

wQBO_h40, wQBO_h65 has a stronger polar night jet during January and February (Figure 5.14a, blue-dot vs. blue-cross), which coincides with a colder polar vortex shown in Figure 5.14b (blue-dot vs. blue-cross). Compared to eQBO_h40, eQBO_h65 also has a stronger polar night jet and a colder polar vortex (Figure 5.14a and 5.14b, red-dot vs. red-cross), but the stronger and colder polar vortex occurs earlier, which is from December–to–February, than that in wQBO_h65 (compared to wQBO_h40). Similarly, comparing wQBO_h40T65 and ICON_NoQBO, there is a stronger and colder polar vortex (Figure 5.14a–b, black-solid vs. black-dashed) in wQBO_h40T65 during DJF (reminder that the westerly Ueq anomaly in wQBO_h40T65, Figure 5.7b). Therefore, by comparing the model differences from the relaxation depths in the six experiments, the results suggest that the seasonal evolution of the polar stratosphere is very sensitive to the Ueq in the upper stratosphere (above ~40 km); a weaker Ueq in the upper stratosphere would result in a weaker polar vortex.

In Chapter 4, I showed that the model is slightly biased to a warmer NH polar stratosphere (when switching off the gravity wave drag effect). Here, the results indicate the NH polar stratosphere is also significantly influenced by the equatorial upper stratosphere. Considering the model also simulates a Ueq that is too weak in the equatorial upper stratosphere, this also contributes to a warmer NH pole.

Secondly, considering the relaxation QBO phase, compared to eQBO_h65, a stronger polar night jet and a colder polar cap is found during January and February in wQBO_h65 (blue-dot vs. red-dot). On the other hand, compared to eQBO_h40, a stronger polar night jet and a colder polar cap is only found during November and December in wQBO_h40 (blue-cross vs. red-cross), which is consistent with the fact that the HT relationship is found from reanalysis based studies to be strongest in early winter (e.g., Holton and Tan 1980; Lu et al. 2008). Thus, if the influence from the upper stratosphere is included, the HT relationship tends to be delayed.

To summarize, a westerly Ueq anomaly in the upper stratosphere could result in: 1) a colder NH polar stratosphere; 2) a delayed HT relationship.

5.5 Summary and conclusions

In this chapter, the dynamical connections between equatorial zonal wind (QBO and SAO) and the polar stratosphere were investigated through a series of model simulations in ICON-ART.

The QBO is most prevalent in the middle-to-lower stratosphere (15–30 km) and is gradually replaced by the dominant variability of the semi-annual oscillation (SAO) in the upper stratosphere (and lower mesosphere). Due to a coarse vertical resolution and a lack of gravity wave drag, the model ICON/ICON-ART fails to generate a QBO-like oscillation. Instead, QBO relaxation is applied to include QBO-varying equatorial winds, a technique which is widely used by the model community to explore the interactions between the QBO and the polar stratosphere (e.g., Matthes et al. 2010). This chapter starts with an assessment of the HT relationship in ERA-I and in ICON-QBO (QBO relaxation run). In general, the ICON-QBO largely reproduced the HT relationship as that in ERA-I (Figure 5.2 and 5.3). But the modelled HT relationship is weaker, and the NH polar stratospheric responses are weaker and less significant than in ERA-I. Then, based on an EP flux analysis of ERA-I, two mechanisms are presented in aspects of lower and middle stratosphere QBO wind. In the lower stratosphere, during wQBO (at 50 hPa), the subtropical critical line is located in the SH, allowing more planetary waves to propagate across the equator. This is associated with an EPFD anomaly at ~30° N, and less upward planetary wave propagation from the troposphere. In the middle stratosphere, the equatorial wind is reversed to that of the lower stratosphere, the critical line is located in the NH, which is associated with an EP flux convergence anomaly at ~30° N. Consequently, the convergence anomaly leads to a warming anomaly, which increases the temperature gradient between the pole and the mid-latitudes, and further results in a stronger polar night jet. This mechanism has been emphasized in recent studies (Yamashita et al. 2011; Garfinkel and Hartmann 2011; Lu et al. 2014). A schematic illustration of the connections is shown in Figure 5.5.

Secondly, based on timeslice integration, a series of idealized experiments is conducted to examine the sensitivity of the polar stratosphere to the QBO phases and the vertical range of equatorial zonal wind. In the idealized experiments, the equatorial zonal wind in the model is relaxed towards the specified perpetual wQBO or eQBO wind profiles over the height range 14–40 km (h40) or 14–65 km (h65). Accordingly, there are four experiments: wQBO_h65, wQBO_h40, eQBO_h65 and eQBO_h40 (see Figure 5.7b). The resulted differences are presented following Table 5.2.

By comparing relaxation depths, it is found that the high relaxation depth runs (wQBO_h65 and eQBO_h65) have a strong westerly anomaly in the equatorial upper stratosphere, which corresponds to a significant strengthening of the polar night jet and a cooling of the polar

vortex. The stronger polar vortex in high relaxation depth runs are directly linked to an equatorward shift of the zero-wind line, allowing more planetary waves to propagate equatorward, and as a result, there is a significant EPFD anomaly in the upper polar stratosphere (above 10 hPa). The results show that how the equatorial zonal wind in the upper stratosphere is simulated strongly influences the model biases in the polar stratosphere. By comparing relaxation QBO phases, though both the zonal mean zonal wind (ZMZM) differences of w/eQBO_h65 and w/eQBO_h40 show a stronger polar night jet, and that the polar stratosphere responses are not significant (also for the polar cap temperature), suggesting that the equatorial upper stratosphere is not the key to build up the HT relationship.

The seasonal evolution of the polar stratospheric response to the equatorial zonal wind shows that both the high relaxation depth runs (wQBO_h65 and eQBO_h65) correspond to a substantial stronger polar night jet and a colder polar vortex during wintertime (late winter for wQBO_h65 and December–February for eQBO_h65). The evolution of the HT relationship (a comparison of QBO phases) is most significant during early winter (November–January) in the pair of low relaxation runs (eQBO_h40 vs. wQBO_h40), and in mid-late winter (January–February) in the pair of high relaxation runs (eQBO_h65 vs. wQBO_h65). Therefore, the HT relationship is delayed when the influence from the upper stratosphere is included. The results further substantiate previous studies (Pascoe et al. 2005), where they found that the QBO in the lower equatorial stratosphere influences early winter polar variability, whereas the QBO and SAO in the upper equatorial stratosphere together influence midwinter polar variability.

Chapter 6 A comparison between interactive-ozone and non-interactive-ozone

6.1 Introduction

With the availability of sunlight and oxygen causes an abundance of ozone in the stratosphere through photochemistry. The absorption of ultraviolet (UV) radiation by stratospheric ozone protects life on Earth from harmful UV radiation and determines the stratospheric temperature structure. Ozone is transported from its' tropical source to middle and high latitudes by the Brewer-Dobson circulation (BDC). The circulation shaped ozone distribution is further feedbacked onto meteorology by radiative heating. It is believed that the interactions between atmospheric ozone and meteorology play a key role in the Earth's climate system. A prominent example is the Antarctic ozone depletion, which significantly contributes to Southern Hemisphere (SH) climate change in recent decades (Thompson et al. 2011; Son et al. 2009). However, in weather/climate models often climatological values of atmospheric ozone (or other atmospheric trace gases) are used. Thus, some feedbacks and interactions between atmospheric ozone and meteorology would be ignored. In this chapter, I focus on the role of stratospheric ozone in the context of general chemistry-climate interactions. Several interactions and feedbacks associated with ozone are first illustrated (Figure 6.1) and will be examined later based on the chemistry-climate model ICON-ART. As illustrated in Figure 6.1, for the polar stratosphere, stratospheric ozone and temperature are coupled (e.g., Pyle et al. 2005),

(1) when the polar stratospheric temperatures are below a threshold value (around 195 K), this is associated with the formation of polar stratospheric clouds (PSC), enabling ozone depletion via heterogeneous chemical reactions and

(2) because polar (Antarctic or Arctic) ozone depletion leads to radiative cooling in the lower stratosphere (Randel and Wu 1999), which may in turn cause further ozone depletion via (1) heterogeneous chemical reactions.

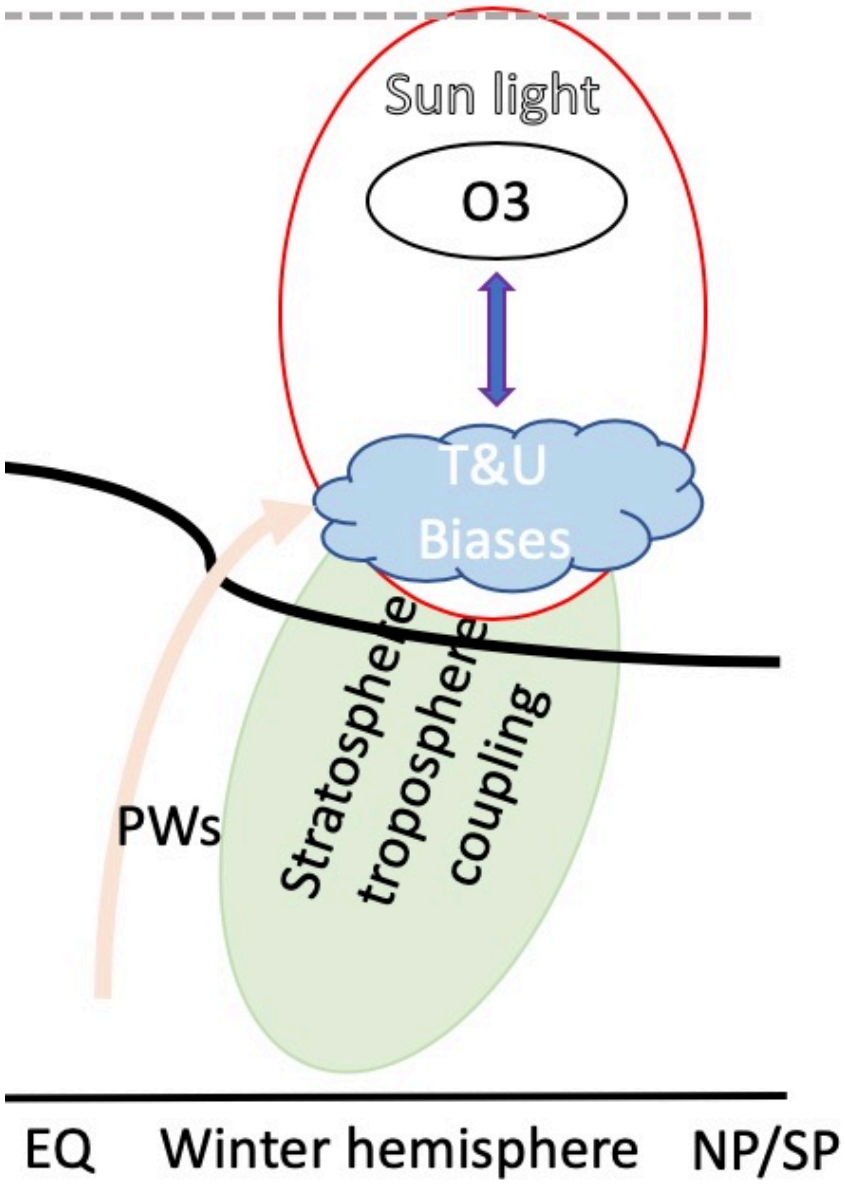

Figure 6.1– Schematic illustrating possible interactions between stratospheric ozone, radiation and circulation. The PWs denotes planetary waves and T, U denotes temperature and zonal wind. The EQ and NP/SP denote the equator and North Pole/South Pole. The illustration is mainly adapted from Haase and Matthes (2018).

Therefore, there is a positive feedback between ozone and polar stratospheric temperature through radiative-chemical processes. Similarly, stratospheric ozone is also influenced by atmospheric dynamics. Lower stratospheric cooling due to polar ozone depletion would strengthen the polar night jet (thermal wind relation), resulting in diminished meridional ozone

transport (or ozone mixing across the polar vortex). Because the BDC is largely driven by vertically propagating and subsequently breaking planetary waves (PWs), the change in PWs also contributes to the meridional ozone transport. As explained by previous studies (e.g., Haase and Matthes (2018)), the feedback between PWs and polar ozone depletion depends on the background polar night jet,

(1) if the background polar night jet is strong, the ozone radiative cooling in the lower stratosphere would hinder upward planetary wave propagation, leading to a weakening of the BDC, i.e., a positive feedback.
(2) if the background polar night jet is very weak, the ozone radiative cooling in the lower stratosphere would favour upward planetary wave propagation, leading to a strengthening of the BDC, i.e., a negative feedback.

Several studies (e.g., Manzini et al. 2003a; Lin et al. 2017; Haase and Matthes 2018) have shown the dominant role of the negative feedback (2) on the polar stratospheric responses to the polar ozone depletion during springtime polar vortex breakup.

As shown above, ozone and meteorology are strongly coupled via chemistry, radiation and transport processes. Thus, whether there is ozone-meteorology coupling in weather/climate models really matters for the forecasts on weather and climate timescales. However, for many weather/climate models, ozone is often represented as a fixed climatology, which is partly due to the high computational cost of fully interactive-ozone simulations. The importance of interactive-ozone has been recognised for the global and regional circulation over time scales ranging from days to years. Based on seasonal ensemble forecast (SEAS5), the impact of interactive-ozone is neutral on the tropospheric forecast scores, and positive on the stratospheric scores, except near the Stratopause (Dragani et al. 2018). A series of typical climate sensitivity simulations with abrupt quadrupled CO2 forcing have been conducted to study the differences between the models with and without interactive-ozone. Nowack et al. (2015, 2017, 2018) adopted the atmosphere-ocean coupled model of Met Office's Unified Model with the United Kingdom Chemistry and Aerosols (UKCA) model, and found when neglecting ozone feedback effect, it leads to ~20% increased global warming, which is attributed to changes in longwave radiative feedbacks associated with circulation-driven decreases in tropical lower stratospheric ozone and related stratospheric water vapor and cirrus cloud changes. They also demonstrated neglecting ozone feedback results in a significant

increase in the number of extreme ENSO events (Nowack et al. 2017), due to the modification of the Walker circulation. This implies that the interactive-ozone not only impacts global climate but also regional climate. Using the Community Earth System Model (CESM) in response to an abrupt quadrupling of CO2, Chiodo and Polvani (2017) found that including interactive ozone significantly reduces (by 20%) the response of the SH midlatitude jet to 4xCO2, which is attributed to a change of the meridional temperature gradient near the tropopause. Using the Goddard Earth Observing System Model in two sets of transient simulations of 1960–2010, Li et al. (2016) compared the simulations with and without interactive stratospheric chemistry, and found that interactive chemistry causes stronger Antarctic lower stratosphere cooling and circumpolar westerly acceleration during November–January and through the stratosphere–troposphere coupling, this correlates with significantly stronger wind stress, leading to stronger ocean warming and enhanced Antarctic sea ice decrease. The prescribed ozone approach is also commonly used to explore the impacts of the Antarctic ozone hole on SH climate, which is further shown that SH responses to ozone depletion and recovery are underestimated when a zonal-mean ozone field is imposed instead of an interactive ozone calculation (Waugh et al. 2009a).

While the interactive-ozone has been shown to be of great importance in response to CO2 forcing or other external forcings (e.g., volcanic eruptions and the Antarctic ozone hole), it is still unclear whether the ozone feedback is important under present-climate conditions. In this chapter, based on the next-generation chemistry-climate model ICON-ART, I'll examine the impacts of interactive-ozone on atmospheric circulations and dynamical mechanisms. This chapter is organized as follows. Section 6.2 describes interactive-ozone in ICON-ART and experimental design. The impacts of interactive-ozone on the circulations in the Southern Hemisphere (SH) and Northern Hemisphere (NH) are presented in Section 6.3 and Section 6.4, respectively. The summary and conclusions are given in Section 6.5.

6.2 Interactive-ozone simulations with ICON-ART

6.2.1 Interactive-ozone

Due to high computational cost of the full gas phase chemistry, simplified chemistry schemes have been developed. Here, I briefly introduce the ozone parameterization that has been

implemented in ICON-ART (Schröter et al. 2018). The description is based on McLinden et al. (2000). The total ozone mixing ratio tendency ($\frac{d\xi}{dt}$) is approximated by the first order Taylor expansion with respect to the local ozone mixing ratio (ξ), temperature (T) and column ozone (c), which is referred to as linearized ozone (Linoz) scheme. The following equation describes the approximation:

$$\frac{d\xi}{dt} = (P-L)^0 + \frac{\partial(P-L)}{\partial\xi}|_0(\xi-\xi^0) + \frac{\partial(P-L)}{\partial T}|_0(T-T^0)$$

$$+\frac{\partial(P-L)}{\partial c_{o_3}}|_0\left(c_{o_3}-c_{o_3}^0\right) - \frac{1}{\tau_{psc}}\xi,$$

where P and L are ozone production and loss term; τ_{psc} is a constant lifetime of ozone loss by the chlorine activation within the PSC regions; and the superscript/subscript 0 stands for reference values.

This equation shows that the ozone mixing ratio tendency ($\frac{d\xi}{dt}$) depends on production and loss term ($P-L$), local temperature perturbation ($T-T^0$), local column ozone perturbation ($c_{o_3}-c_{o_3}^0$) and chemical losses approximated by the exponential decrease of ozone within PSC regions ($-\frac{1}{\tau_{psc}}\xi$), which is not included in the regular linearized ozone parameterization (see Schröter et al. (2018) for more details). There are also other parameterizations which are similar to Linoz, i.e., Cariolle scheme and Monge-Sanz scheme (Flemming et al. 2017) that will not be considered here. Using machine learning, Nowack et al. (2018a) build a temperature-based ozone parameterization that solely relies on temperature. The advantages and shortcomings of different ozone parameterizations are out of the scope of this thesis.

6.2.2 Non-interactive-ozone (fixed ozone climatology)

In contrast to interactive-ozone, non-interactive-ozone in ICON-ART uses monthly climatological ozone that is derived from GEMS (Global and regional Earth-system Monitoring using Satellite) and an in-situ data climatology (Hollingsworth et al. 2008). The original climatological ozone is presented at pressure levels with 31 layers. When the ICON-ART radiation scheme is called, the monthly climatological ozone is interpolated to the ICON-ART model levels (here 47 layers), and is also linearly interpolated by two monthly mean

values to the model timestep. The temporal interpolation is similar to that of the bimonthly sea surface temperatures (SSTs) interpolation.

6.2.3 Experimental setup

In order to assess the impacts of interactive-ozone on global and regional climate. Two simulations are conducted,

(1) (fully)-interactive-ozone (FIO3): ozone is calculated by the Linoz scheme and is then used in radiation scheme to get the radiative heating rate. Ozone and atmospheric flows are dynamically consistent;

(2) non-interactive-ozone (NIO3): ozone is derived from climatological ozone of FIO3 (50-year average) and is used in the radiation scheme. Ozone chemistry and transport is still calculated in NIO3. In this study, the prescribed climatological ozone is represented at 85 pressure layers instead of the default 31 pressure layers, thus diminishing ozone differences due to vertical interpolation.

In NIO3 run, there are two different ozone fields in NIO3 that will be used later (see Table 6.1). Because FIO3 uses simplified ozone chemistry (Linoz scheme) for radiative calculation, therefore the two ozone fields are the same.

Table 6.1 – Definition of two ozone fields (ozone_Int and ozone_Linoz) in NIO3

ozone fields	Description
ozone_Linoz	This ozone is calculated by Linoz scheme.
ozone_Int	This ozone is derived from FIO3 climatological ozone after temporal and vertical interpolation and used for radiative calculation.

The two simulations use a timeslice integration strategy (see Chapter 3) with trace gases and boundary conditions of the year 2000 and an integration time of 52 years. The timeslice integration uses a fixed SSTs climatology (inter-annually invariant) in order to better display the atmospheric internal variabilities. Because NIO3 uses 3-D climatological ozone, this is different from zonal mean ozone which is commonly used in other non-interactive-ozone

simulations. Therefore, the ozone asymmetries are still represented in NIO3 but the ozone interannual variations are missing.

6.3 Impacts of interactive-ozone on the SH

I compare the 50-year mean state (the first two years are ignored) of FIO3 with NIO3. To highlight the role of interactive-ozone, the differences in the mean state between FIO3 and NIO3 are presented as FIO3 minus NIO3.

6.3.1 Ozone climatology in ICON-ART with a comparison to ERA-I

The ozone climatology from FIO3 is compared to that of ERA-Interim data (ERA-I), which is found to be a consistent representation of observations (Dragani 2011). The monthly and zonal mean total column ozone (TCO) climatology for FIO3 and ERA-I are shown in Figure 6.2. In the ERA-I climatology, the tropics show the smallest seasonal variation and the lowest TCO values (200–300 DU). Both the NH and SH extra-tropics show strong seasonal variations. In the NH, the TCO peaks during later winter and spring (~350 DU); in the SH, the TCO reaches minimum in the high latitudes during September and October (TCO < 200 DU), which is generally referred to as Antarctic ozone hole. The larger ozone abundance in the Arctic during spring is due to stronger planetary wave forcing (stronger BDC). In the Antarctic, due to relative weaker planetary wave forcing, there is a very strong Antarctic polar vortex, as depicted as a strong TCO gradient between the high- and mid-latitudes. By November or December, the Antarctic polar vortex gradually breaks up, then the TCO values return to over 250 DU.

Compared to ERA-I, the TCO seasonal cycle in the Arctic and Antarctic is well represented in FIO3. However, the model simulated much less TCO at both the SH and NH pole. At the NH pole, the modelled TCO approaches ~300 DU during early winter and ~350 DU during late winter and spring, which is smaller than that in ERA-I by ~50 DU. At the SH pole, the ozone hole period (below 200 DU) is substantially increased from ~August to December, as compared to that in ERA-I from ~September to November, suggesting that the modelled Antarctic polar vortex persists longer and breaks up later. As a quick reminder, in Chapter 4, the model assessment showed that there are cold biases in the Antarctic lower stratosphere during austral

spring (see Chapter 4, Figure 4.6) (due to a lack of non-orographic gravity wave drag). Therefore, I believe that the lower-than-normal TCO in the Antarctic is highly correlated to the cold biases in the model. So, bearing in mind that the comparison between FIO3 and NIO3 is under a relative strong Antarctic polar vortex.

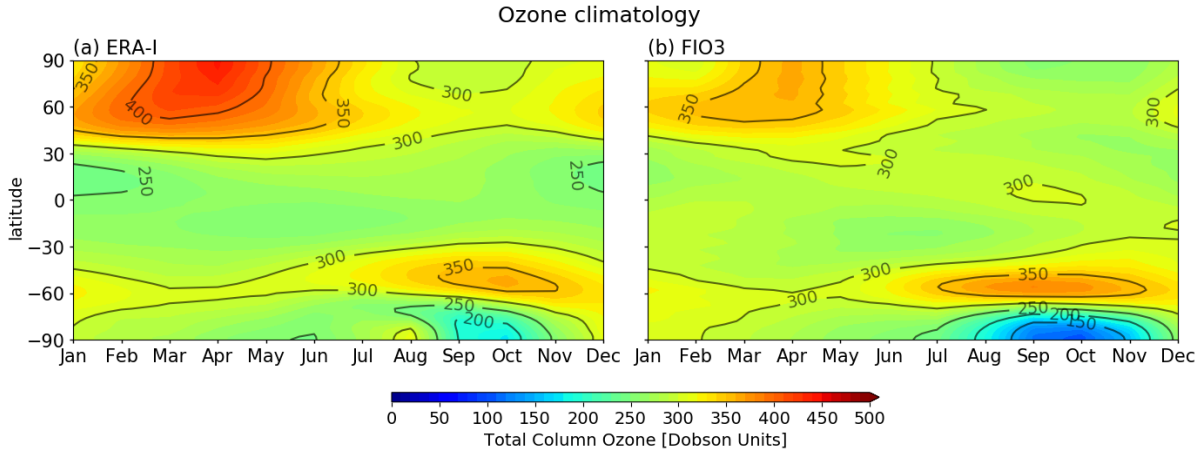

Figure 6.2– Monthly and zonal mean ozone climatology in Dobson units (DU) for (a) ERA-I and (b) FIO3. The ozone climatology of ERA-I is for the period 1979–2000.

6.3.2 Annual mean differences between FIO3 and NIO3

Figure 6.3 shows annual and zonal mean differences in ozone mixing ratio (OMR, ozone_Linoz), temperature, water vapor and temperature change due to shortwave radiation (temp_rsw). With interactive ozone chemistry, the OMR in FIO3 is significantly decreased in the troposphere (Figure 6.3a), whereas generally increased in the stratosphere. Here, I omit the discussion of the tropospheric ozone because the tropospheric ozone is poorly represented in this simple chemistry (Linoz) scheme (there are neither sinks nor sources for the tropospheric ozone). The annual mean temperature differences (Figure 6.3b) show a dipole anomaly in the Antarctic stratosphere with a significant warming (> 1 K) in the upper stratosphere (from ~30–1 hPa) and significant cooling (< –1 K) in the lower stratosphere (from ~200–50 hPa). In the tropics, the FIO3 has significant warming (> 0.4 K) above ~100 hPa and cooling (< –0.4 K) in the upper troposphere and lower stratosphere (UTLS). The temperature decrease in the UTLS region coincides with a significant water vapor decrease by about 2% in FIO3 (Figure 6.3c).

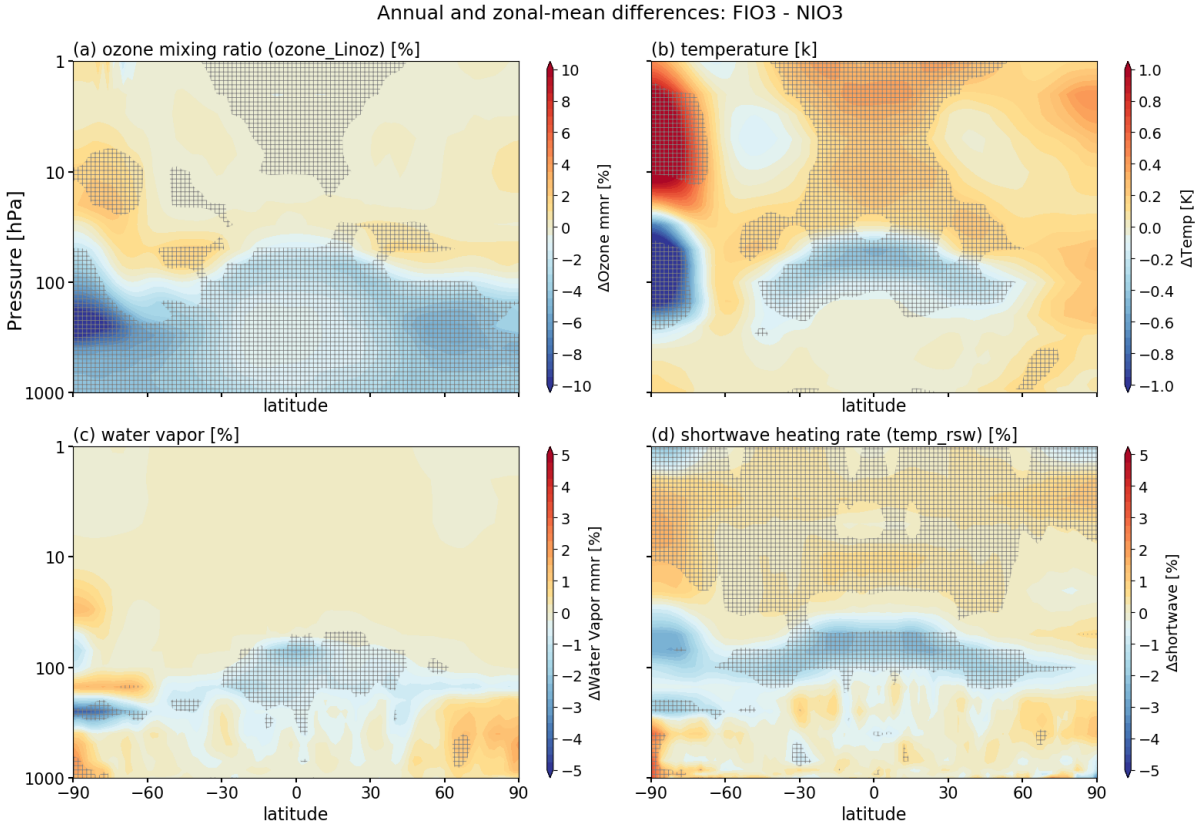

Figure 6.3– Annual and zonal mean differences in (a) ozone mixing ratio (OMR), (b) temperature, (c) water vapor, (d) shortwave heating rate (temp_rsw) (K/day). (a), (c) and (d) are shown in percentage differences as labelled (%). Note that ozone_Linoz of NIO3 is used for ozone differences calculation (see Table 6.1). Stippling denotes the differences significant at the 95% confidence level.

Radiative forcing is one of the major causes for the temperature differences. ICON-ART outputs the temperature change due to shortwave heating (temp_rsw). As shown in Figure 6.3d, compared to NIO3, FIO3 has a significant decrease of temp_rsw in the UTLS region (~4 %), particularly in the tropical UTLS, and a slight increase of temp_rsw in the upper stratosphere. Clearly, the temp_rsw differences are very consistent with the cooling in the tropical UTLS region as well as the temperature dipole anomaly in the Antarctic stratosphere (Figure 6.3b).

As stratospheric ozone is an important absorber of shortwave radiation, I examine the differences in the ozone fields used for the radiative calculation. Figure 6.4 shows the annual mean ozone percentage differences (ozone_Int). Note that ozone_Int is the interpolated ozone which is derived from the FIO3 climatology and used for the radiative calculation in NIO3. It is found that FIO3 has a ~8% decrease of ozone in the UTLS region and the Antarctic lower stratosphere, and that there is a small increase of ozone (< 2%) in the upper stratosphere. The

decrease of ozone in the UTLS region is linked to less shortwave radiation absorption (Figure 6.3d), leading to a colder UTLS (Figure 6.3b). The cooling in the Antarctic lower stratosphere is also attributed to the decrease of ozone in FIO3, but the dynamical heating rate is also important, which is discussed later. The ozone discrepancies (decrease or increase) are mainly due to the miss-match of pressure fields between NIO3 and FIO3. Because the OMR has very steep gradients in the UTLS region (Figure 6.4, green contours), the vertical interpolation acts to smooth the ozone gradients and make high stratospheric ozone values shift downward. It is found that there is strong sensitivity of radiative forcing to ozone (and water vapor) in the UTLS region (Riese et al. 2012). Such ozone discrepancies and associated water vapor changes amplify in abrupt quadrupled CO2 forcing scenario and results in ~20% global surface warming when neglecting the ozone feedback (Nowack et al. 2015). The impact on global surface temperature is very weak under present-day climate conditions (not shown, also see Figure 1 in Nowack et al. (2015)).

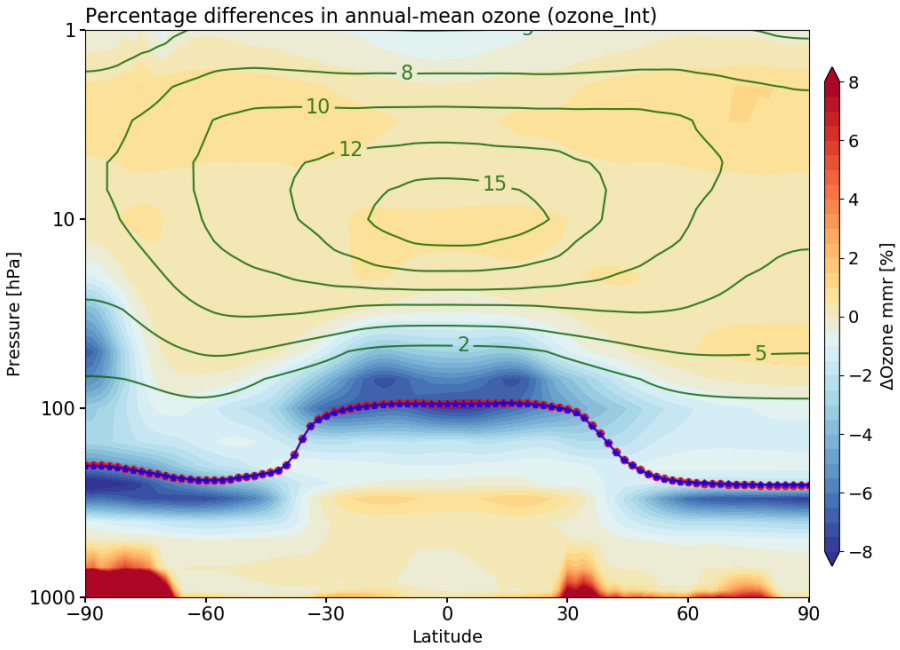

Figure 6.4– Percentage differences in ozone (ozone_Int) between FIO3 and NIO3 (a quick reminder that ozone_Int is linearly interpolated from the climatological ozone of FIO3). Green contours show the FIO3 climatology. Red and blue line denotes the thermal tropopause (according to the World Meteorological Organization definition) for FIO (red) and NIO3 (blue), respectively.

6.3.3 Monthly-mean temperature differences between FIO3 and NIO3

In response to interactive-ozone, the temperature dipole in the Antarctic stratosphere is evident (Figure 6.3b). Here, the influence of interactive-ozone on the Antarctic stratosphere are further investigated from the perspective of the annual cycle and dynamical interactions.

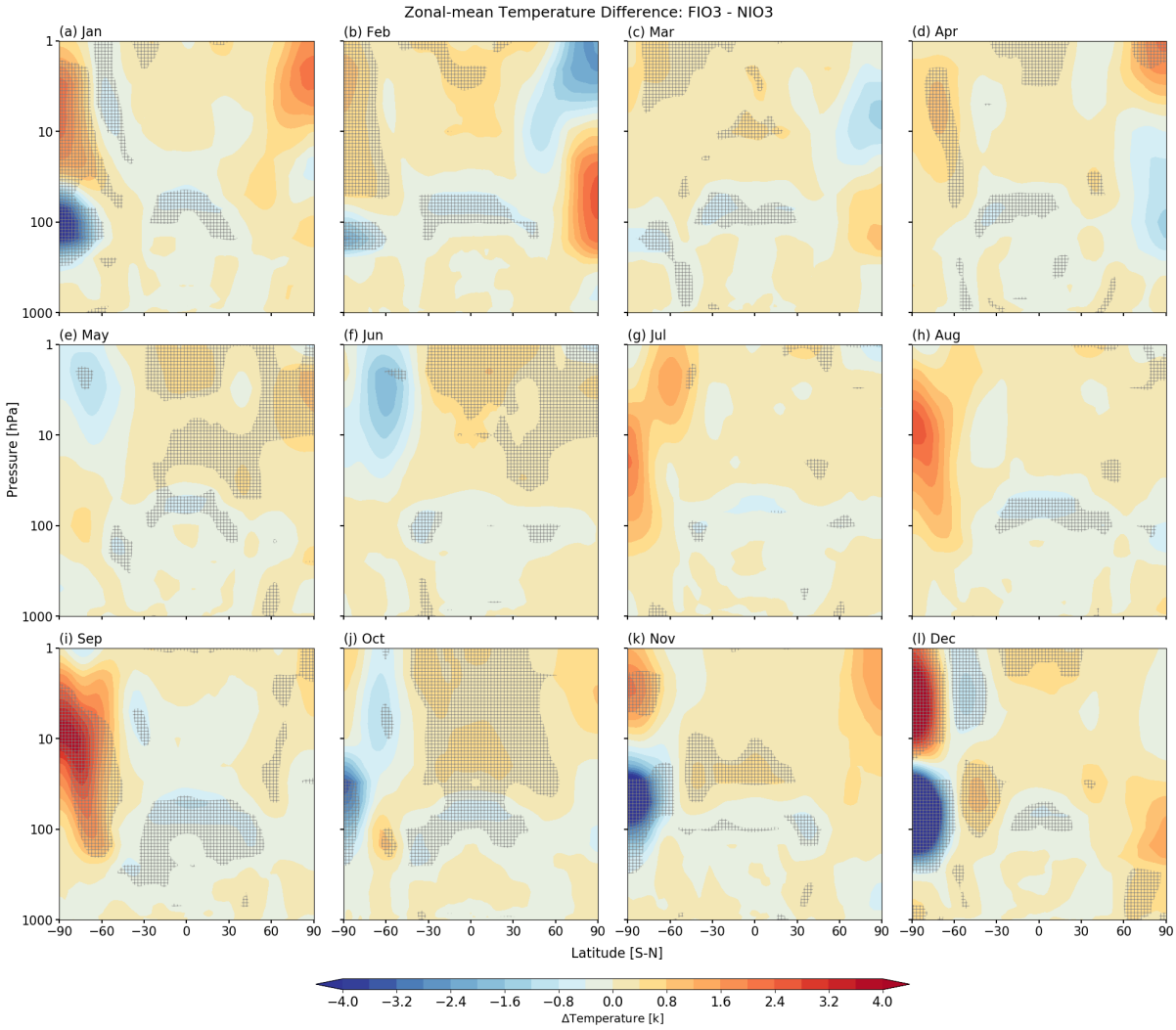

Figure 6.5– Differences in monthly and zonal mean temperature (ZMT) from January to December. Stippling denotes differences significant at the 95% confidence level.

Figure 6.5 shows monthly and zonal mean temperature (ZMT) differences from January to December. Compared with NIO3, the entire Antarctic stratosphere is substantially warmer in FIO3 from June–August, particularly in September. Then, the lower stratosphere gets colder in October, followed by an intensified cooling from November to December as well as a strong warming in the upper stratosphere. This pattern gradually weakens from January to February.

With stratospheric ozone chemistry, the Arctic stratosphere is slightly warmer during February and March, but the differences are not significant. In the tropical stratosphere, the ZTM differences are roughly analogous to the annual mean.

6.3.4 Ozone differences due to temporal interpolation

Figure 6.6 shows time-height cross-sections of the differences in ozone_Linoz and ozone_Int, respectively. Figure 6.6a displays the ozone differences after temporal and vertical interpolation of NIO3, and Figure 6.6b displays what are the differences in simulated ozone as a result of the different ozone representation (NIO3 vs. FIO3). Compared to NIO3, FIO3 has above ~6% decrease of OMR in the lower stratosphere (below 30 hPa) during austral spring (September–November) (Figure 6.6a). The maximum ozone decreasing peaks in October (~12%). In the UTLS region, there is also about 6% ozone decrease all year-round. This is similar to Figure 6.4 (annual mean), which is explained by the vertical interpolation in NIO3. Except for austral spring, a slightly increase of OMR is found in the lower and upper stratosphere. Several studies (e.g., Sassi et al. 2005; Neely et al. 2014) have revealed that this ozone discrepancies in the Antarctic lower stratosphere are mainly due to the temporal interpolation in NIO3. Here similar to Sassi et al. (2005), the daily and monthly OMR at 50 hPa and 88º S for both NIO3 (ozone_Int) and FIO3 are shown in Figure 6.7. It is clear that the monthly mean of daily OMR in NIO3 tends to smooth the extreme values, and after the temporal interpolation, the daily OMR becomes slightly larger during austral spring (September–December) and slightly smaller during the other months. Therefore, it appears that the temporal interpolation in NIO3 leads to an underestimate of the magnitude of the extreme (maximum/minimum) monthly ozone values in FIO3, resulting in large ozone discrepancies in October (~12%, Figure 6.6a) when ozone reaches its minimum (Li et al. 2016). Because stratospheric ozone is an important absorber of shortwave radiation, the impacts of ozone discrepancies on the stratospheric circulation as well as the tropospheric circulation are analysed in the following.

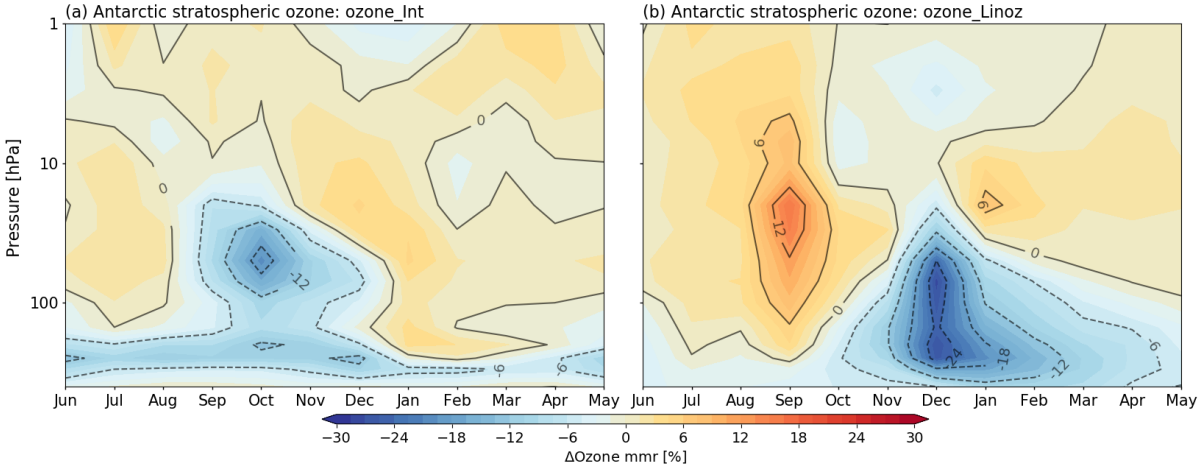

Figure 6.6– Time-height cross-sections for ozone percentage differences in the Antarctic stratosphere (average of 70º S–90º S): (a) ozone in FIO3 minus ozone_Int in NIO3 (interpolated ozone); (b) ozone in FIO3 minus ozone_Linoz in NIO3 (interactive ozone chemistry). See Table 6.1 for definition of ozone_Int and ozone_Linoz.

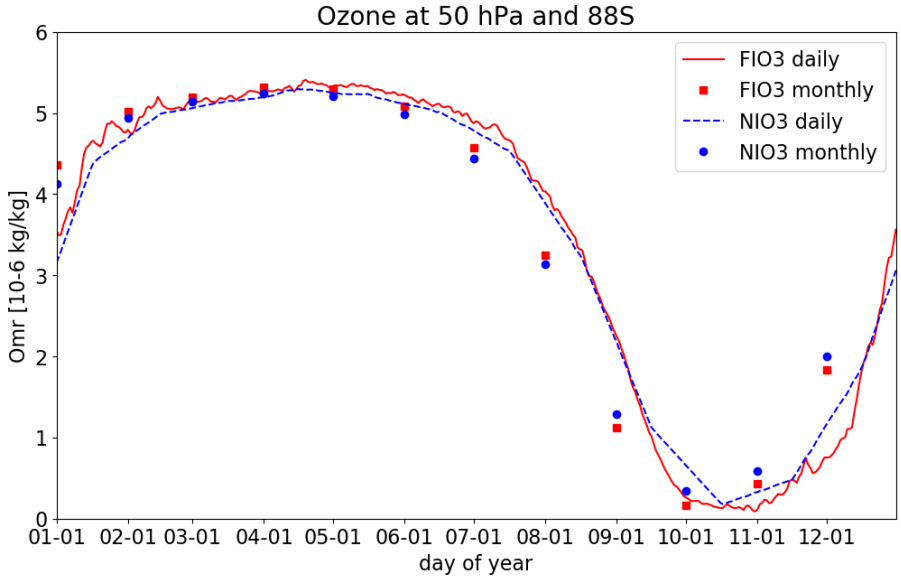

Figure 6.7– Evolution of zonal mean ozone mixing ratio (OMR) at 50 hPa and 88º S: daily OMR of FIO3 (red) and daily OMR of NIO3 (blue). Monthly-mean of daily OMR is denoted as red-squares for FIO3, and the monthly- mean of daily OMR (ozone_Int) is denoted as blue-circle for NIO3. The daily OMR of NIO3 (blue) is linearly interpolated values of the monthly mean of FIO3 (red-squares). This plot is similar to Sassi et al. (2005).

The ozone_Int in NIO3 is used for the radiative heating rate calculation; ozone_Linoz is derived from the Linoz scheme and adjusting to its surroundings. It doesn't have a feedback to atmospheric circulations. In Figure 6.6b, when ozone is calculated interactively, Antarctic stratospheric ozone (ozone_Linoz) shows a substantial OMR increase (~9%) from August–September, while OMR decreases (>12%) below ~10 hPa from November–March with the

largest deviation in December (>24%). Compared to the differences in ozone_Int (Figure 6.6a vs. Figure 6.6b), the maximum ozone decrease in ozone_Linoz is nearly doubled (~12% vs. ~24%) and delayed by ~2 months (October vs. December), implying that the ozone differences in ozone_Int (due to interpolation) could induce circulation changes and further feedback onto the differences in modelled atmospheric ozone.

6.3.5 Antarctic stratospheric temperature and heating rates

The underestimated ozone (ozone_Int) in NIO3 affects the simulation of the Antarctic stratospheric temperature. Differences in the Antarctic stratospheric temperature (poleward of 70º S) is shown in Figure 6.8a. Compared to NIO3, FIO3 has a significant warming from June–September (particularly in September), which is followed by a temperature dipole anomaly from October–March with a significant warming in the upper stratosphere and a significant cooling in the lower stratosphere (200–50 hPa). This temperature dipole peaks in December with a magnitude (<–4 K in the lower stratospheric and >2 K in the upper stratosphere). As ozone_Linoz is positively correlated with local temperature (first order Taylor expansion), the Antarctic stratospheric temperature response to interactive-ozone resembles closely the differences in ozone_Linoz (in Figure 6.6b vs. Figure 6.8a). However, these temperature differences do not closely match the differences in ozone_Int. Cooling in the lower stratosphere is from October–March while the ozone decrease is from September–December, suggesting that the ozone discrepancies in ozone_Int significantly modify the Antarctic stratospheric circulation. This is also found in Neely et al. (2014), where they suggest to use the daily instead of monthly ozone climatology to reduce the biases due to monthly-mean ozone interpolation in the non-interactive-ozone run.

Here, I'm interested in what is the dynamical and radiative forcing that contribute to the temperature differences in Figure 6.8a. Here, the temperature differences are decomposed into a dynamical (e.g., advection or residual circulation) and a diabatic component (e.g., radiative heating rate). The temperature differences from temp_rsw in percentage, temp_rsw and dynamical heating rate (temp_dyn) are presented in Figure 6.8b–d, respectively. The dynamical heating rate is calculated following Martineau et al. (2018) (also see Appendix A). Firstly, associated with the ozone decrease (ozone_Int) in FIO3 (Figure 6.6a), the temp_rsw is decreased by ~10%, leading to a radiative cooling in the lower stratosphere (200–50 hPa) from October–December (Figure 6.8a). Secondly, both temp_rsw and temp_dyn contribute to the

Antarctic temperature dipole from October–December, but temp_dyn is the dominant force for a warmer stratosphere during austral winter (June–September). Thirdly, in the lower stratosphere, the persistent cooling from January to February is not consistent with the dynamical heating or the shortwave heating rate, which is linked to a delayed polar vortex break up that is simulated in FIO3 (examined later). By comparing model simulations with and without an Antarctic ozone hole in the coupled chemistry climate model UM-UKCA, Keeble et al. (2014) found similar Antarctic temperature dipole response (< –12 K in the lower stratosphere and > 6 K in the upper stratosphere), and they found that temp_rsw contributes to lower stratospheric cooling while temp_dyn contributes to upper stratospheric warming. Note that the lower stratospheric cooling in FIO3 is nearly half of the Antarctic ozone hole effect (–6 K vs. –12 K), implying that neglecting the interactive-ozone effect could significantly underestimate circulation responses to the Antarctic ozone hole.

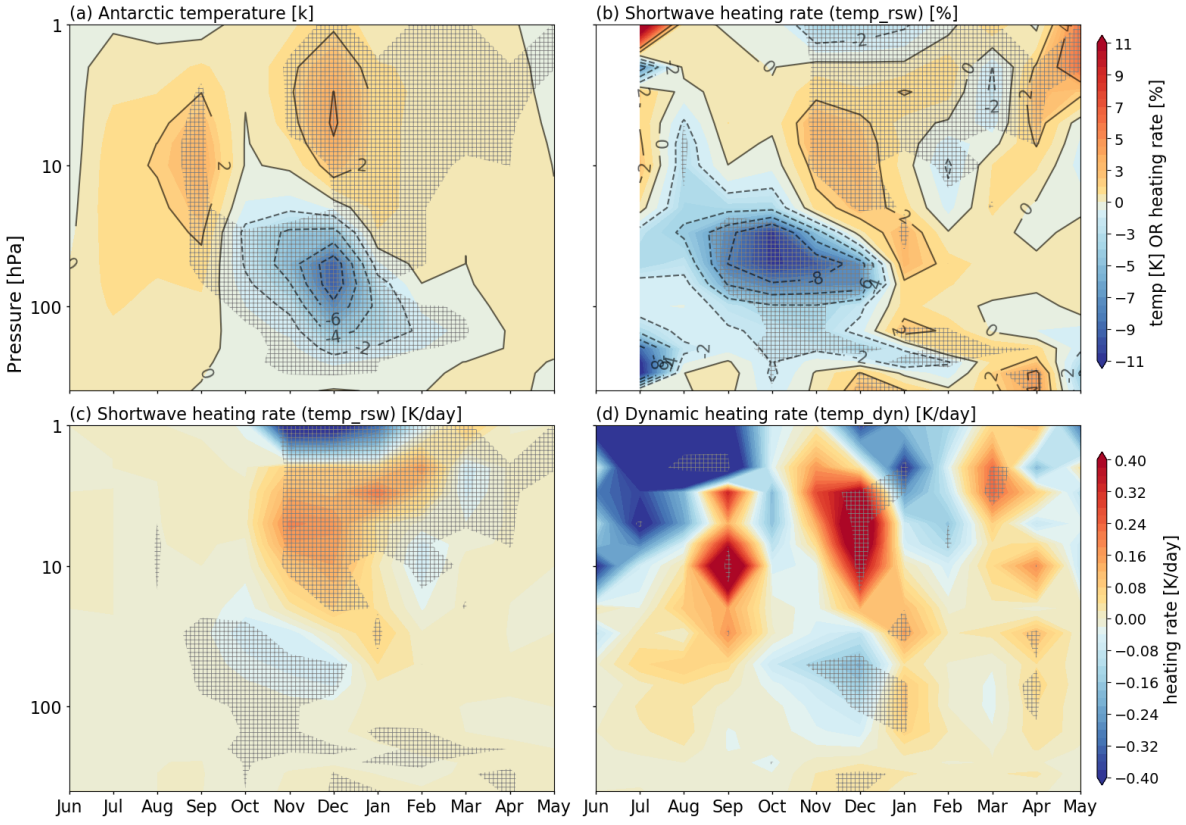

Figure 6.8– Time-height cross-sections of differences in (a) Antarctic stratospheric temperature (K), (b) shortwave heating rate (%), (c) shortwave heating rate (K/day) and (d) dynamical heating rate (K/day). (b) and (c) are shown in percentage differences as labelled (%). Stippling denotes differences significant at the 90% confidence level.

6.3.6 Polar night jet and planetary waves

The cooling in the Antarctic lower stratosphere shown in Figure 6.8a leads to a stronger polar night jet (Figure 6.9a) through thermal wind balance, further affecting planetary wave propagation. In the following, the polar night jet and planetary waves are examined.

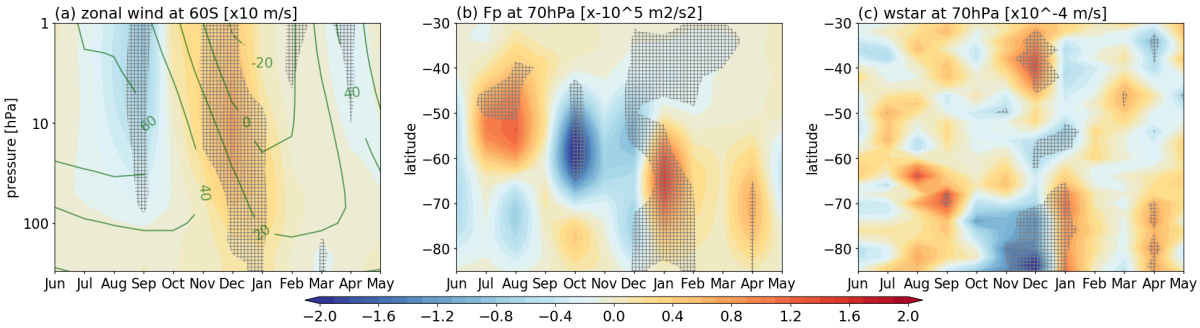

Figure 6.9– (a) Differences in the polar night jet (zonal wind at 60 ºS) in time-height cross-section and the polar night jet climatology of FIO3 overlaid green contours. Time-latitude cross-sections of differences in (b) vertical component of EP flux, Fp at 70 hPa difference and (c) residual vertical velocity, $\overline{w^*}$ at 70 hPa differences (c). Stippling denotes differences significant at the 90% confidence level. The differences in zonal wind at 60 ºS, Fp at 70 hPa and $\overline{w^*}$ at 70 hPa are scaled and labelled in the figure title.

The vertical component of EP flux (Fp) at 70 hPa (hereafter referred to as Fp70) measures planetary wave activities that propagate from the troposphere into the stratosphere. In order for the sign to be consistent in the NH, the original Fp70 is multiplied by –1 so that positive (negative) values indicate upward (downward) propagation. Differences in monthly mean Fp70 are shown in Figure 6.9b. Compared to NIO3, the Fp70 in FIO3 shows a slight increase in austral winter (JJA) and a substantial decrease from October–December (maximum in October), and is followed by a substantial increase from January–February. Because planetary wave forcing is one of the major components of temp_dyn in the stratosphere, the increase or decrease of Fp70 is consistent with the differences in temp_dyn (Figure 6.8d). As expected, such a consistency exists also for the residual vertical velocity ($\overline{w^*}$) (the residual circulation is largely driven by upward planetary wave propagation and subsequent wave breaking (Andrews et al. 1987)). A stronger (weaker) wave forcing during October–December (January–February) is linked to an increase (decrease) of downwelling in Figure 6.9c ($\overline{w^*}$ at 70 hPa). A comparison between wave forcing (Fp70) and the polar night jet (zonal wind at 60 ºS), however, doesn't exactly match (Figure 6.9a vs. Figure 6.9b). A stronger polar night jet in FIO3 is linked to a decrease of wave forcing during October–December, but is linked to an increase of wave

forcing during January–February. Similarly, there is also a negative correlation between temp_dyn and Antarctic stratospheric temperature during January–February (Figure 6.8a vs. Figure 6.8d).

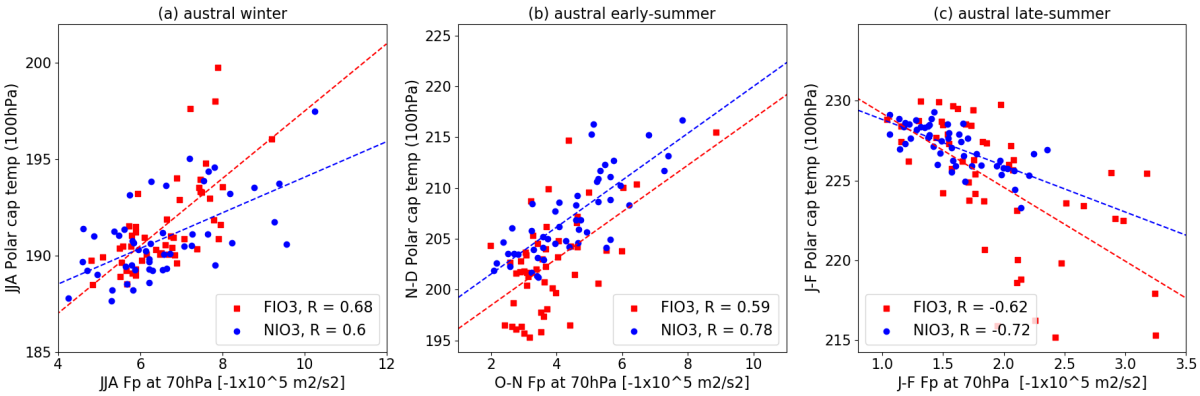

Figure 6.10– Scatterplot between upward wave propagation (Fp70) and Antarctic temperature at 100 hPa: (a) JJA mean Fp70 and JJA mean polar cap temperature; (b) October–November (O–N) mean Fp70 and November–December (N–D) mean polar cap temperature; (c) January–February (J–F) mean Fp70 and January–February (J–F) mean polar cap temperature.

To further examine the interactions between the polar vortex and planetary waves, Figure 6.10 shows a scatterplot of Fp70 and polar cap temperature at 100 hPa in NIO3 (blue) and FIO3 (red). During austral winter, the polar vortex is very cold, which is correlated with planetary wave forcing (Fp70) (R = 0.68 in FIO3 and R = 0.6 in NIO3) (Figure 6.10a). In Figure 6.10a, the Fp70 leads the polar cap temperature by approximately one month (O–N vs. N–D). Obviously, the wave forcing is positively correlated with the polar cap temperature in the lower stratosphere for both runs (Figure 6.10a, correlation coefficients $R > \sim 0.6$). The stronger wave forcing during austral spring predicts a warmer polar vortex during early austral winter. Therefore, a lower Fp during austral spring in FIO3 is related to a colder polar vortex during austral early winter (November–December). This is consistent with Salby et al (2012), where it is shown that the year-to-year Antarctic ozone variation during September–November are highly correlated with a meridional heat flux at 70 hPa (proportional to Fp70) during August–September. Note that in FIO3, the correlation between wave forcing and temperature is smaller (0.59 vs. 0.78). This positive correlation indicates a positive feedback between the polar cap vortex and PWs (Figure 6.1). However, in Figure 6.10c, the Fp70 is anti-correlated with polar cap temperature for both runs with correlation coefficients $R < -0.6$, indicating a significant negative dynamical feedback. Depending on the strength of the background polar night jet,

there are either positive or negative interactions between PWs and the zonal mean flow (Figure 6.1). This negative feedback has also been illustrated in previous studies (e.g., Manzini et al. 2003; Lin et al. 2017; Haase and Matthes 2018).

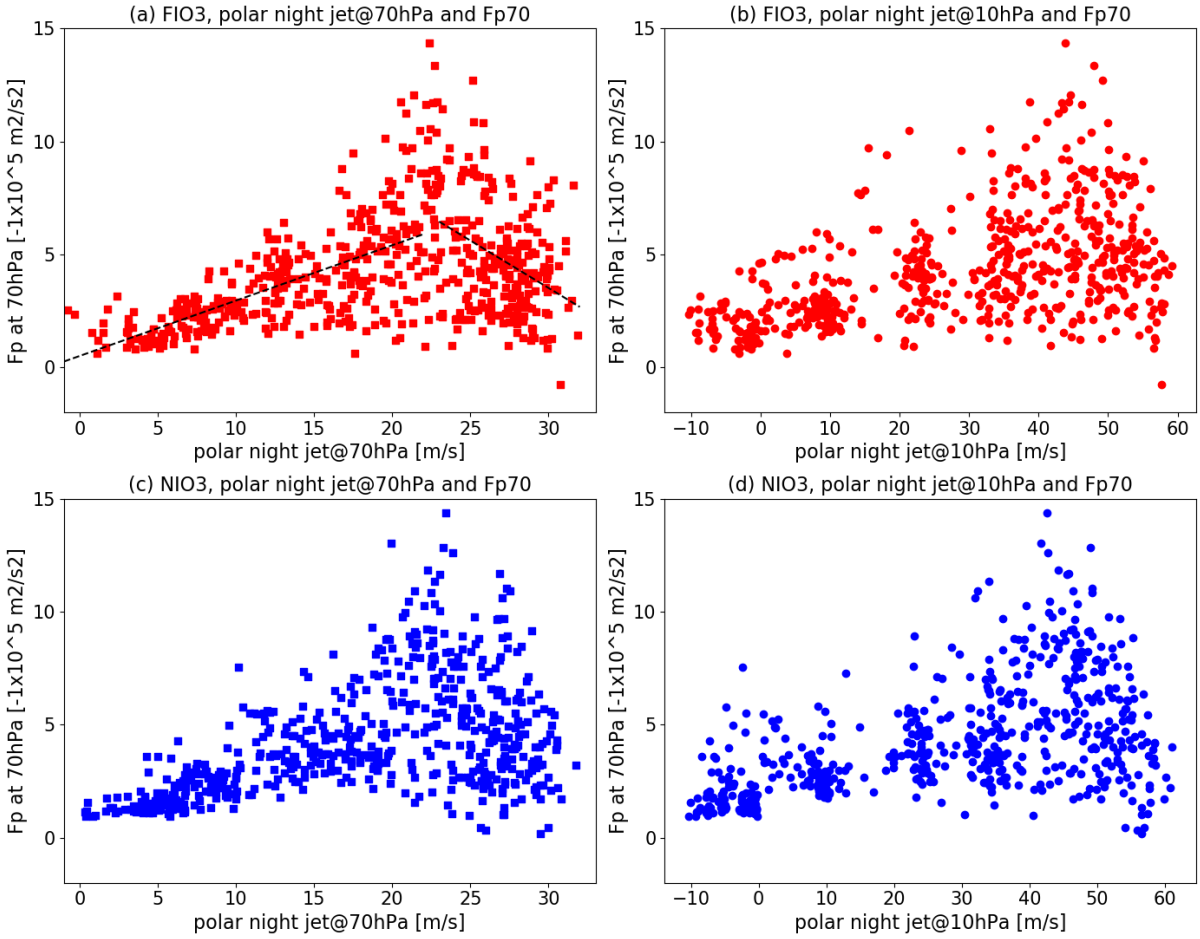

Figure 6.11– Scatterplot of monthly polar night jet and Fp at 70 hPa (Fp70): (a) polar night jet at 70 hPa and Fp70 in FIO3, (b) polar night jet at 10 hPa and Fp70 in FIO3, (c) polar night jet at 70 hPa and Fp70 in NIO3 and (d) polar night jet at 10 hPa and Fp70 in NIO3. Black lines in (a) show the least-square linear fit. Upward wave propagation depends on the strength of polar night jet.

The dependence of upward wave propagation into the stratosphere on westerly jet is illustrated in Figure 6.11, which shows the scatterplot of monthly Fp70 and polar night jet at 70 hPa and 10 hPa. Clearly, we see when the polar night jet is below a threshold value, e.g., ~22 m/s in Figure 11a, the upward wave propagation is enhanced along with the increase of westerly wind; when the polar night jet is above a threshold value, the upward wave propagation is suppressed along with the increase of westerly wind. This phenomenon is explained by the Charney-Drazin theory (Charney and Drazin 1961).

6.3.7 Timing of polar vortex breakup and planetary waves

Antarctic vortex breakup is characterized by a weakening of the polar night jet and a transition from austral winter westerlies to austral summer easterlies. In general, this is also referred to as final stratospheric warming event. The final breakup date plays an important role for the polar ozone concentration as well as tropospheric circulations (e.g., Sheshadri et al. 2013).

Figure 6.12 shows the annual cycle of zonal mean zonal wind at 60° S for FIO3 and NIO3 (the zero-wind contours are marked by pink). Because the model has cold biases in the Antarctic stratosphere (Chapter 4, and Figure 6.2), the average breakup date in NIO3 or FIO3 is around December which is later than the date in common observations (September to November) (Hurwitz et al. 2010). By comparing the two simulations, the zero-wind contour of NIO3 precedes that of FIO3, suggesting a delayed polar vortex breakup for the interactive-ozone run.

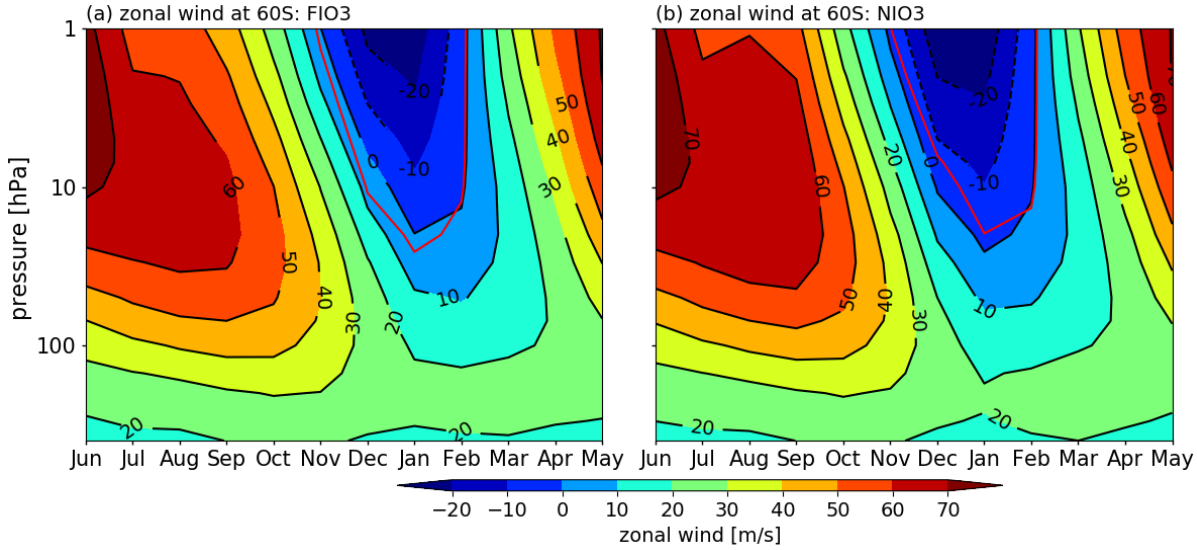

Figure 6.12– Annual cycle of zonal mean zonal wind at 60° S: (a) FIO3 and (b) NIO3. Pink lines denote zero-wind contours: (a) NIO3 and (b) FIO3.

Planetary wave activities entering the stratosphere have been shown to precede the polar stratospheric variability by about 1~2 month (Figure 6.10a). Here, the relationship between planetary wave activities and the polar vortex breakup date is examined. The polar vortex breakup date is defined as the transition from westerlies to easterlies at 60° S and 10 hPa. The scatterplot between the polar vortex breakup date and Fp70 for FIO3 and NIO3 are shown in Figure 6.13. On average, the polar vortex breakup date occurs on 24 December in FIO3 and 12 December in NIO3, which means the transition to easterlies at 60° S and 10 hPa is delayed by

11–12 days in FIO3. From Figure 6.12a, it is evident that the planetary wave forcing is anti-correlated with the breakup date. The correlation between Fp70 and breakup date is slightly stronger in NIO3 that in FIO3 (red-dots vs. blue-dots, –6.3 vs. –4.4). Because of the delayed breakup in FIO3, I shifted the October–November (O–N) mean Fp70 by 1 month and plotted the November–December (N–D) mean Fp70 over the breakup date in Figure 6.13b. Then, the correlation becomes stronger for FIO3 (R = –6.6 vs. –5.9). Therefore, the planetary wave forcing strongly modulates the polar vortex breakup date, which is consistent with Hurwitz et al. (2010). When ozone is interactively calculated, planetary waves entering the stratosphere during October–December is significantly reduced, leading to a delayed polar vortex breakup. Although planetary waves are generally not able to propagate in the summer hemisphere, due to a very late polar vortex breakup, the westerly jet still persists in the lower stratosphere during ~January–February.

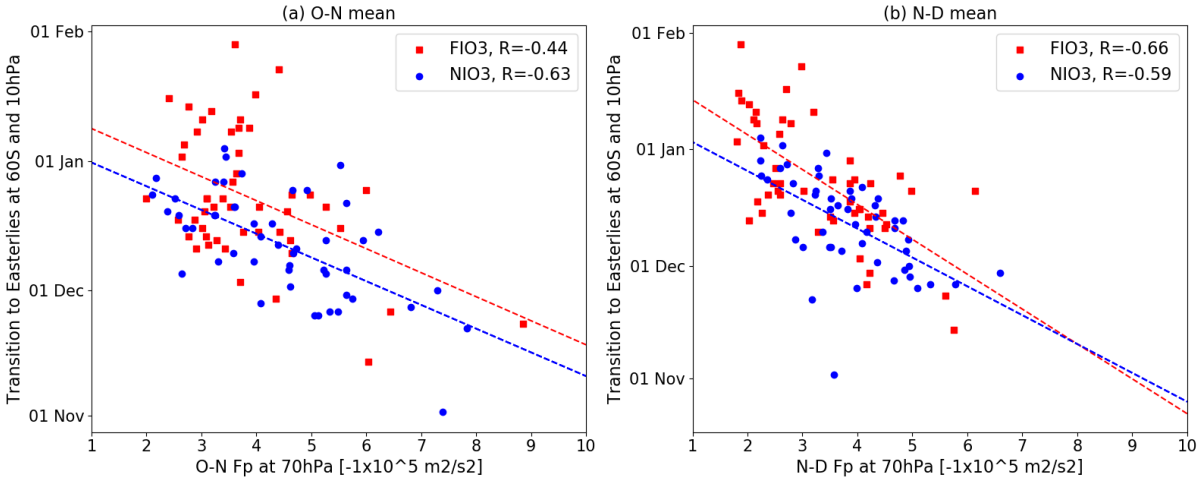

Figure 6.13– Scatterplot between the date of the transition to easterlies at 60° S and 10 hPa and monthly-mean Fp70 (averaged over 40–80° S): (a) O–N mean Fp70; (b) N–D mean Fp70. The blue dots are for NIO3 and red squares are for FIO3, and the blue or red line shows the linear fit. The correlation coefficients R for FIO3 and NIO3 are shown in the figure legend.

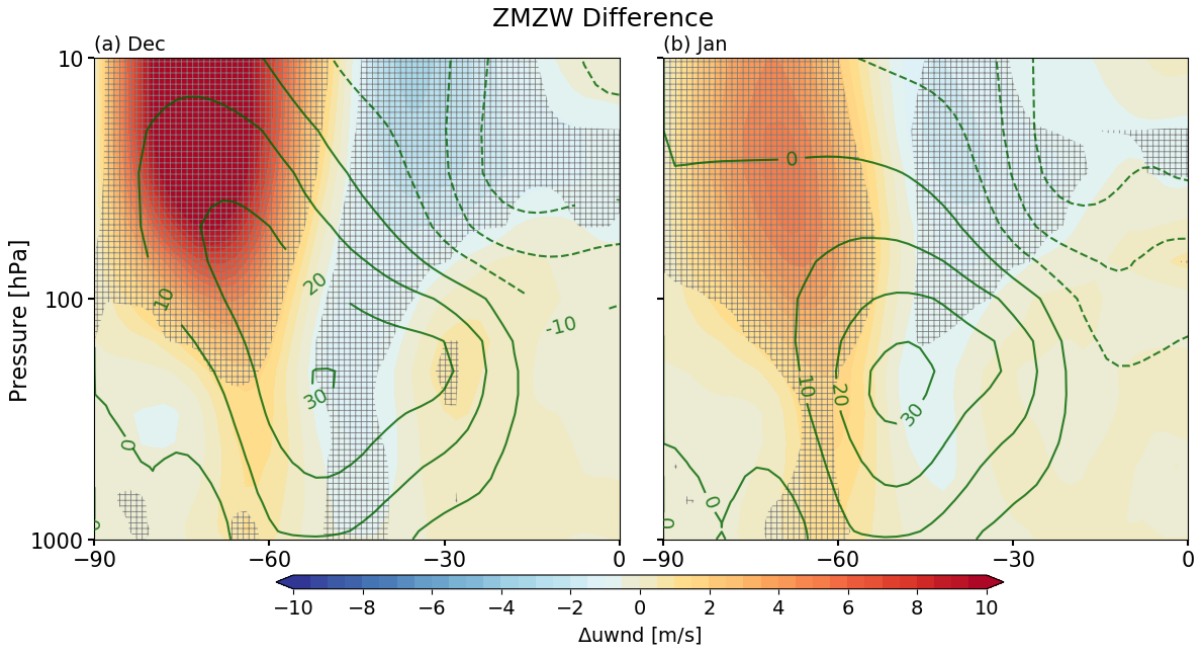

Figure 6.14– Zonal mean zonal wind (ZMZW) differences between FIO3 and NIO3 in (a) December and (b) January. Green contours show the climatological ZMZW of NIO3. Stippling denotes differences significant at the 95% confidence level.

6.3.8 Impacts on the tropospheric circulations

The SH polar stratospheric changes associated with interactive-ozone are descended further down in the atmosphere, leading to significant changes in the tropospheric circulation. Figure 6.14 shows the zonal mean zonal wind (ZMZW) differences between FIO3 and NIO3 in December and January. Compared to NIO3, there is a stronger polar night jet in FIO3 during both months in the polar stratosphere. In the troposphere, accordingly, there is a significant weakening (strengthening) of westerlies at the southern (northern) flank of the mid-latitude jet maximum in December (January), which clearly demonstrates a poleward shift of the mid-latitude jet. Figure 6.15 shows the Antarctic temperature differences at 100 hPa, 500 hPa and 850 hPa with sea level pressure (SLP) differences overlaid. It is found that the polar vortex is significantly colder using interactive-ozone, which is consistent with the strengthening of the polar night jet (Figure 6.14). With interactive-ozone, FIO3 has a significant cooling over Antarctic Peninsula at the surface (or near). The sea level pressure differences display a dipole pattern with negative differences at high latitudes and positive differences at mid-latitudes. The SLP responses to interactive-ozone largely resemble the positive phase Southern Annular Mode (SAM). Numerous studies (see Scientific Assessment of Ozone Depletion: 2018, chapter

5) have shown a significant positive trend of SAM (particularly during austral summer) in recent decades, which is associated with a poleward shift of the tropospheric jet, and the Antarctic ozone hole is suggested to be the dominant driver (Perlwitz et al. 2008). Therefore, the SH circulation responses to interactive-ozone are equivalent to the response to the Antarctic ozone hole during austral spring. The results imply that the SH responses to the Antarctic ozone hole are underestimated when neglecting the effect of interactive-ozone, which is consistent with Waugh et al. (2009b).

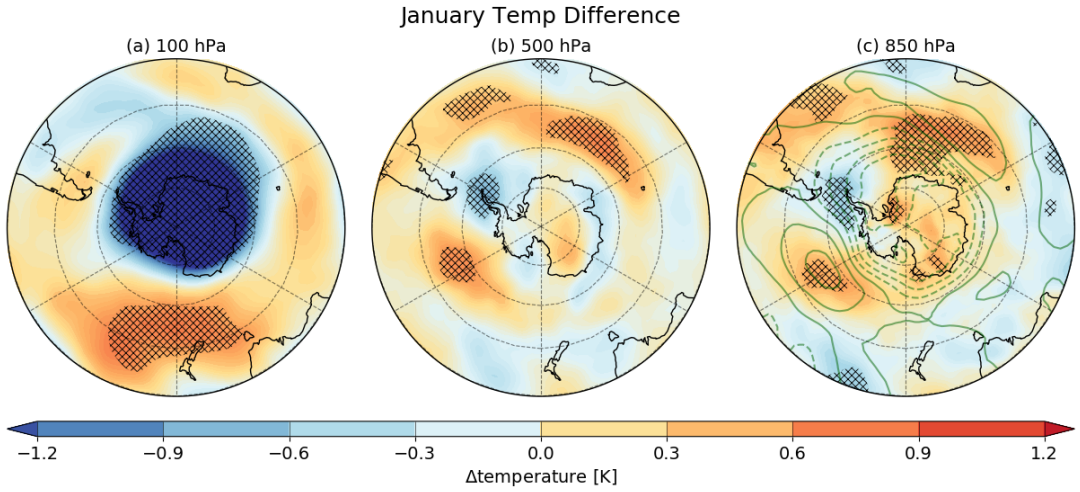

Figure 6.15– Stereographic plots of January Antarctic temperature differences at: (a) 100 hPa, (b) 500 hPa and (c) 850 hPa. Green contours in (c) are the differences in sea level pressure. Stippling denotes differences significant at the 95% confidence level.

6.4 Impacts of interactive-ozone on the NH

6.4.1 Mean state differences

For the NH, a significant signal hasn't been found in zonal mean fields (e.g., Figure 6.4). This is partly due to large internal variability over the NH. However, in the horizonal plane, the interactive-ozone does have significant influences. Figure 6.16 (a–d) shows geopotential height (GPH) differences at 200 hPa from September–December. In September, there are wave-like anomalies with positive GPH anomalies in Alaska, the eastern Asia and the eastern United States. In November, there are significant negative anomalies in the south of Greenland, and the signal is further intensified during December. This anomaly pattern from November–December resembles the negative North Atlantic Oscillation (NAO-like) pattern.

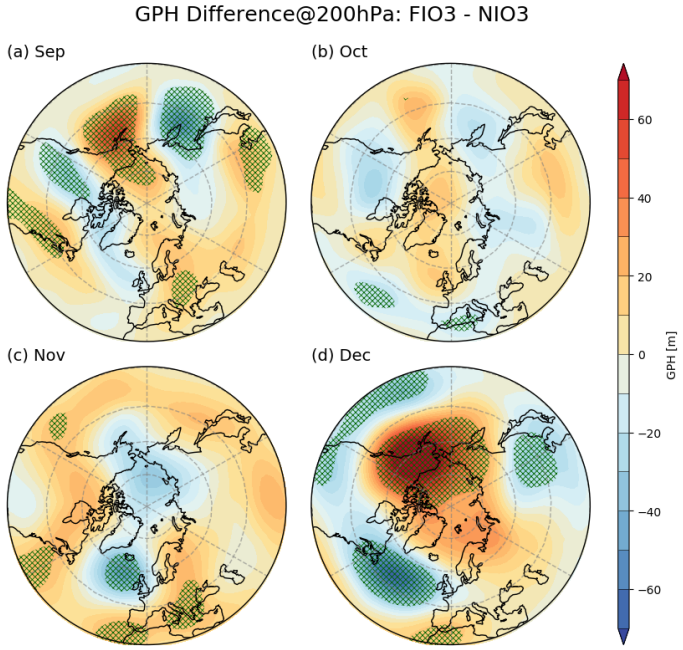

Figure 6.16– Stereographic plots of geopotential height (GPH) differences at 200 hPa for (a) September, (b) October, (c) November and (d) December.

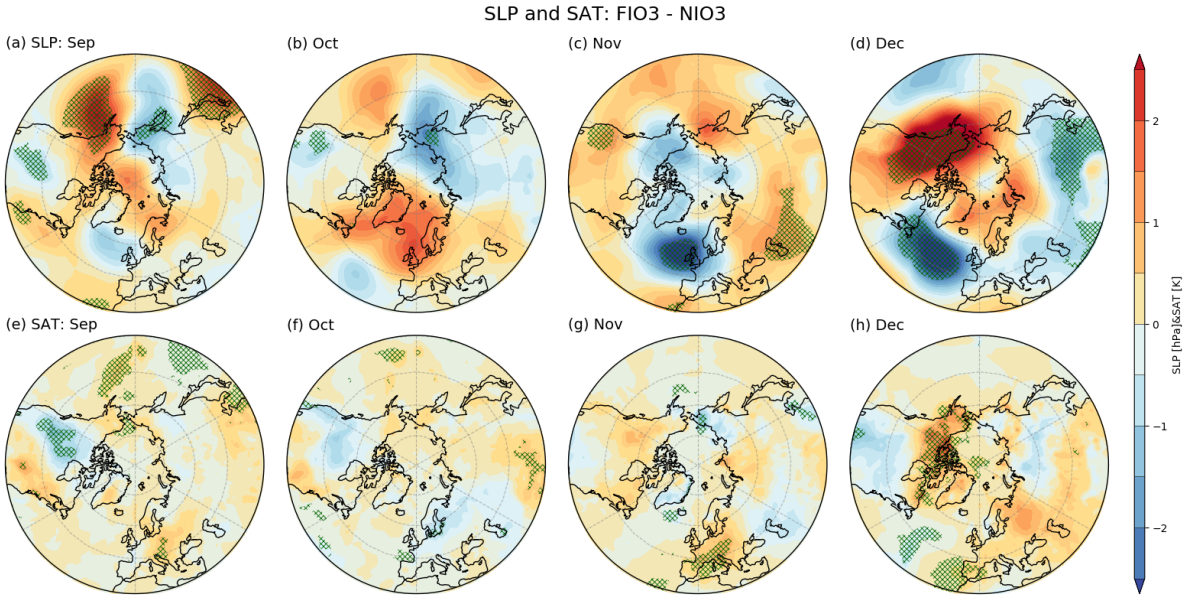

Figure 6.17– Stereographic plots of sea level pressure (SLP) and surface air temperature (SAT) differences for (a) September, (b) October, (c) November and (d) December. Stippling denotes differences significant at the 95% confidence level.

At the surface, the SLP and surface air temperature (SAT) differences are shown in Figure 6.17 (a–d). Generally, the SLP differences are consistent with the GPH differences at 200 hPa, suggesting the barotropic structure. As a consequence, there are significant cold anomalies over

western United States during September and warming anomalies over southern Europe during November and December.

6.4.2 ENSO teleconnection

El Nino and Southern Oscillation (ENSO) can drive large-scale atmospheric Rossby waves that propagate poleward along the great circle (Hoskins and Karoly 1981). Over the NH, it excites a Pacific/North American (PNA) pattern (Hoskins and Karoly 1981); over the SH, it excites a Pacific/South American (PSA) pattern (Karoly 1989). The NIO3 uses the climatological ozone in radiation scheme, where the ozone does not have interannual variability. An important question is whether the noninteractive-ozone representation might also impact the ENSO teleconnection. In this study, the ENSO teleconnection pattern is examined in NIO3 and FIO3.

Here, the Southern Oscillation index (SOI) is defined as the SLP difference between Tahiti and Darwin, Australia,

$$\mathrm{SOI} = \mathrm{SLP}_{\mathrm{Tahiti}} - \mathrm{SLP}_{\mathrm{Darwin}}.$$

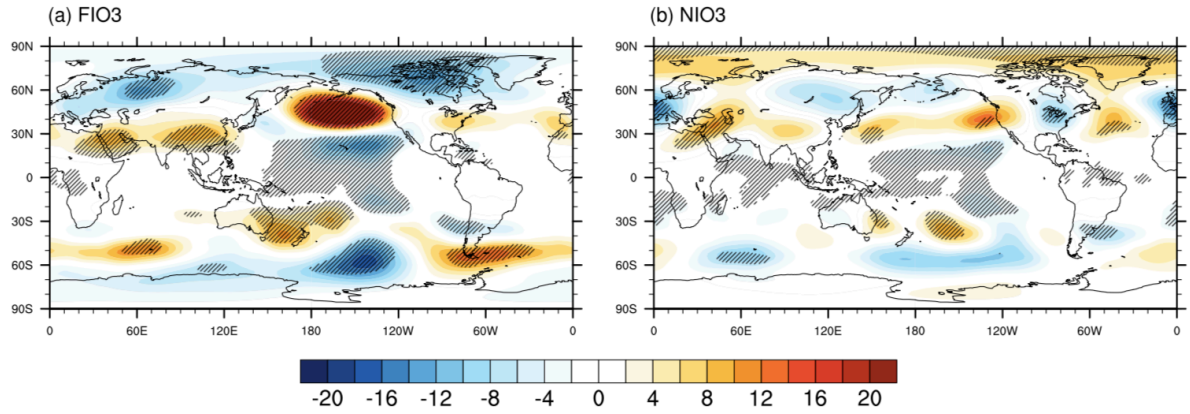

Figure 6.18– The ENSO teleconnection is represented as the GPH at 200 hPa regressed onto the Southern Oscillation index (SOI) for (a) FIO3 and (b) NIO3. Stippling denotes statistical significance at the 95% level.

Figure 6.18 shows the regression maps between January–March mean Southern Oscillation index and GPH at 200 hPa. For FIO3, both the PNA and PSA patterns are clearly represented with significant height anomalies over the tropical Pacific, Northern Pacific, Northwestern Canada, and the Southern Pacific and Amundsen Sea. This is known as a typical ENSO teleconnection pattern. However, for NIO3, both the PNA and PSA patterns disappear or are not obvious, especially at high latitudes. This indicates when neglecting interactive ozone,

particularly the interannual variability of ozone, in radiation scheme, the ENSO teleconnection patterns (PNA and PSA) are suppressed.

6.5 Summary and conclusions

In this chapter, I have investigated the role of interactive-ozone for the global and regional circulations, particularly for the SH climate by using the chemistry-climate model ICON-ART. I designed two experiments: 1) (fully)-interactive-ozone (FIO3) and 2) non-interactive-ozone (NIO3). In FIO3, ozone is calculated interactively with a simple stratospheric chemistry; while in NIO3, the ozone is derived from the climatology of FIO3, which is by definition annually invariant. Both runs were integrated for 52 years with repeating boundary conditions of the year 2000.

The seasonal cycle of the ozone climatology in FIO3 is compared to ERA-I at first. As presented in Chapter 4, there are cold-pole biases in the Antarctic stratosphere, which are partly due to a lack of gravity wave drag. Accordingly, the climatological total column ozone (TCO) in FIO3 is biased with very low TCO during austral spring (Figure 6.2).

The ozone chemistry and dynamics are coupled by nature. The interactive-ozone enables the ozone field to adjust to the flow change simultaneously, and to feedback on the dynamics by modifying the temperature structure (flow-consistent). In NIO3, however, the ozone used in the radiation scheme is the climatological ozone (derived from FIO3) through temporal and vertical interpolation and thus the ozone is mostly flow-inconsistent. Because the temporal and vertical interpolation of NIO3 act to smooth extreme values of the monthly-mean ozone climatology, this creates significant ozone discrepancies between FIO3 and NIO3,

(1) vertical interpolation tends to smooth the strong vertical ozone gradients in the upper troposphere and lower stratosphere (UTLS) region, resulting in an increase of ozone mixing ratio (OMR) with a ~5% increase at polar latitudes and a ~8% at low latitudes, respectively (Figure 6.4);

(2) temporal interpolation tends to smooth the gradients in ozone seasonal cycle, resulting in ~8% OMR increase in the lower Antarctic stratosphere during austral spring (when there is lowest TCO) (Figure 6.5a);

(3) note that because the annually invariant ozone is used, the ozone interannual variability is also missing in NIO3.

Because stratospheric ozone is a key absorber of solar radiation, the ozone discrepancies feedback on the atmospheric dynamics by modifying the local energy balance. By comparing the differences between the flow-consistent and flow-inconsistent ozone representation, i.e., FIO3 and NIO3, significant impacts of interactive-ozone on regional and global circulations are revealed.

In the tropics, decreased ozone is found in the UTLS region for the interactive-ozone run (due to vertical interpolation). As a result, less solar radiation is been absorbed in FIO3, leading to a significant cooling in the UTLS region with a magnitude of about 0.4 K (Figure 6.3b). The colder UTLS is accompanied by a significant decrease of water vapor (Figure 6.3c).

Because a more significant effect is observed in the SH than the NH, the impacts on the mean state and dynamical mechanisms are explored in detail, which are illustrated in Figure 6.19. Firstly, during austral winter (June-August), interactive-ozone is associated with a warmer Antarctic stratosphere. Even though there is a slight increase of ozone in FIO3, the increase of the dynamical heating rate mainly accounts for the warmer Antarctic stratosphere (no availability of sunlight during austral winter). Secondly, during October–December, FIO3 shows a large ozone decrease (particularly in October) in the Antarctic lower stratosphere (temporal interpolation in NIO3). This leads to significant radiative cooling in the Antarctic lower stratosphere. The dynamical heat rate also contributed to the colder Antarctic lower stratosphere, as a result of a stronger polar night jet. Upward propagation of planetary waves into the stratosphere and subsequent breaking provides eddy momentum, heat flux and largely drives the BDC. It is found that there is a decrease of wave forcing, which is positively correlated to a stronger polar cap temperature. Thirdly, during January–February, as there is decreased wave forcing during early austral summer, the polar vortex breakup date is delayed in the interactive-ozone run. This is linked to the persistent colder stratosphere at the same time. However, due to the weaker polar night jet during the polar vortex breakup, wave forcing is anti-correlated with polar cap temperature, i.e., the increase of dowelling limits the cooling in the lower stratosphere. The signals in the stratosphere propagate downward, leading to a poleward shift of the tropospheric mid-latitude jet and to a negative SLP anomaly at the high latitudes. These tropospheric responses largely resemble a positive phase of SAM, which is

similar to the tropospheric response to the Antarctic ozone hole. This suggests that the SH responses to the Antarctic ozone hole would be underestimated when the interactive-ozone is neglected.

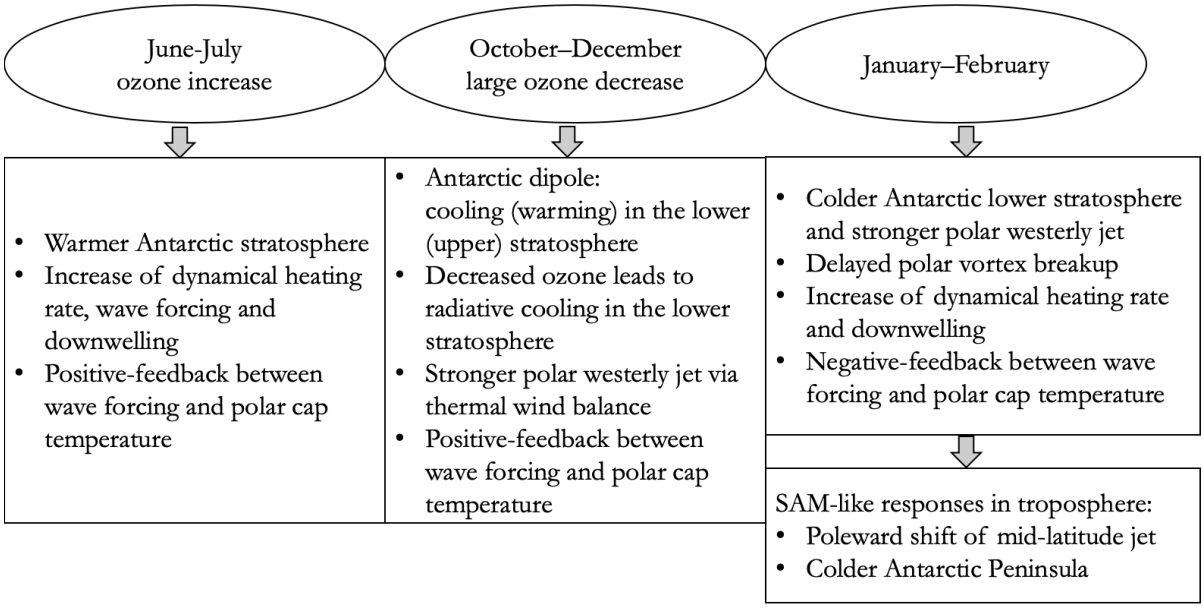

Figure 6.19– Schematic diagram illustrating the impacts and dynamical mechanism for interactive-ozone on the SH climate.

In the NH, significant differences are only found in the horizontal plane and not in zonally averaged meteorological fields. On the mean states, the differences between FIO3 and NIO3 resemble a negative NAO-like pattern during November–December, with a weakening of the Azores high and warming over southern Europe. For the teleconnection pattern, it is found that without interactive-ozone, the PNA (and also the PSA) that is dynamically related to ENSO is poorly represented. I believe that the lack of interannual ozone variability in NIO3 would be the reason. An additional experiment with interannual ozone variability in the noninteractive-ozone run instead of annually invariant ozone (NIO3) would verify this hypothesis.

Chapter 7 Conclusions and outlook

7.1 Conclusions

With the advancement of computers, we develop and apply atmospheric models of ever-increasing complexity (such that we incorporate a wide range of physical processes). This thesis examines several physical processes in the stratosphere that are often poorly represented in current atmospheric models and displays their complex interactions within the atmospheric system.

This thesis is based on the next generation weather/climate model ICON-ART with a grid resolution of ~160 km and 47 vertical levels. By analysing a series of ICON-ART long-term simulations, it shows that the default model poorly represents the QBO and stratospheric ozone, leading to substantial impacts on the tropospheric circulation. In the following, the main results are summarized.

7.1.1 Model bias and correction

Since atmospheric models use parameterizations of the unresolved physical processes, some model bias is often unavoidable. I start with model bias characterization and rectification. In Chapter 4, the climatology and variability of ICON-ART longterm simulations (AMIP-type) are validated against ERA-Interim data. The modelled stratospheric mean states exhibit substantial biases: (1) SH polar winter cold biases; (2) NH polar winter warm biases, and (3) no stratospheric QBO-like oscillation. The NH polar winter warm biases have been found to be related to extensive subgrid-scale orographic (SSO) gravity wave drag, which is parameterized following Lott and Miller (1997). To correct the biases, the SSO drag above 40 km in the model has been switched off. This results in a substantial improvement of the

simulations of the polar night jet, the polar vortex and planetary waves. Due to the coupling between the stratosphere and troposphere, the correction of NH polar stratospheric biases also leads to a better simulation of the NH troposphere and surface climate.

The QBO simulation remains a challenge for climate models, especially when coarser resolutions are applied (Butchart et al. 2018). The missing QBO-like oscillation in the tropical stratosphere is rectified by zonal wind relaxation. The same relaxation method is applied in Chapter 5 to investigate the interactions between the tropical wind regimes and the polar stratosphere. The lack of a QBO-like oscillation in ICON-ART is diagnosed to be due to the parameterized non-orographic gravity wave drag (NONGWD) that seems too small. It is also found that the SH polar winter cold biases are sensitive to the amplitude of NONGWD.

7.1.2 Interactions between the tropical wind regimes and the polar stratosphere

In Chapter 5, dynamical interactions between equatorial zonal winds (QBO and SAO) and the polar stratosphere were investigated through a series of model simulations. This chapter started with an assessment of the HT relationship in ERA-Interim and in ICON-QBO (QBO relaxation run). In general, the ICON-QBO largely reproduced the HT relationship compared to ERA-Interim. But the modelled HT relationship is weaker and less significant than that in ERA-Interim.

Based on timeslice integration, a series of idealized experiments were conducted to examine the sensitivity of the polar stratosphere to the QBO phases and the vertical range of equatorial zonal winds. In the idealized experiments, the equatorial zonal wind in the model is relaxed towards the specified perpetual wQBO or eQBO wind profiles over the height range of 14 to 40 km (h40) or 14 to 65 km (h65). By comparing the two relaxation depths, it is found that the high relaxation depth (h65) runs have a strong westerly anomaly in the equatorial upper stratosphere, which corresponds to a significant strengthening of the polar night jet and a cooling of the polar vortex. The stronger polar vortex in high relaxation depth runs is directly linked to an equatorward shift of the subtropical zero-wind line in the upper stratosphere, allowing more planetary waves to propagate equatorward, and as a result, there is a significant EPFD anomaly in the upper polar stratosphere (above 10 hPa). The results show that the manner in which the equatorial zonal wind in the upper stratosphere is simulated strongly

influences the model biases in the polar stratosphere. By comparing the relaxation QBO phases (wQBO vs. eQBO), the evolution of the HT relationship is most significant during early winter (November–December) in the pair of low-top relaxation runs (eQBO vs. wQBO with relaxation range = h40), and in mid-late winter (January–February) in the pair of high-top relaxation runs (eQBO vs. wQBO with relaxation range = h65). Therefore, the HT relationship is delayed when the influence from the upper stratosphere is included. The results further substantiate previous studies (Pascoe et al. 2005), where it was shown that the QBO in the lower equatorial stratosphere influences early winter polar variability, whereas the QBO and SAO in the upper equatorial stratosphere together influence midwinter polar variability.

7.1.3 Interactive ozone

In Chapter 6, I examined the role of interactive-ozone on the global and regional circulations, particularly on the SH climate through a comparison of two experiments: 1) (fully)-interactive-ozone (FIO3) and 2) non-interactive-ozone (NIO3). In FIO3, the modelled ozone is able to feedback onto the radiation and in NIO3, the ozone uses the climatological ozone (annually invariant) of FIO3 for the radiative calculation.

The seasonal cycle of the ozone climatology in FIO3 is compared to ERA-Interim at first. The climatological total column ozone (TCO) in FIO3 is biased with very low TCO during austral spring, when the TCO reaches a minimum. Because a bimonthly ozone interpolation in NIO3 acts to smoothen the gradients in the ozone seasonal cycle, the austral springtime ozone minimum is underestimated in the Antarctic lower stratosphere (~8% increase). As a consequence, the FIO3 has a substantial radiative cooling in the Antarctic lower stratosphere and in austral spring (also December). The colder pole is accompanied by a stronger polar night jet (thermal wind balance). This leads to a suppression of upward planetary wave propagation. The decreased planetary wave activities in FIO3 therefore corresponds to a delayed polar vortex breakup. It is found that the wave forcing is dependent on the background polar night jet, as pointed out by e.g., Haase and Matthes (2018). Before the polar vortex breakup, the wave forcing is positively correlated with polar cap temperature, and therefore enhances the radiative cooling arising from ozone decrease in FIO3. After the polar vortex breakup, the wave forcing is negatively correlated with polar cap temperature, and therefore counteracts the lower stratospheric cooling. Due to the stratosphere-troposphere coupling, there are SAM-like responses in the SH troposphere, with a poleward shift of the mid-latitude jet and a negative

SLP anomaly at high latitudes, when ozone is calculated interactively. Therefore, it suggests that the SH responses to the Antarctic ozone hole would be largely underestimated when neglecting the interactive-ozone effect.

7.2 Outlook

As shown above, the representation of the stratosphere is still deficient in the current version of ICON-ART. Future work includes to continue assessing and developing ICON-ART.

Firstly, it would be interesting to further investigate the sensitivity of the middle atmosphere to the parameterized gravity wave drag (SSO gravity wave drag and NONGWD) in a systematic way. In Chapter 4, it is already demonstrated that the NH polar stratosphere is sensitive to SSO gravity wave drag. As the stratosphere contributes to the predictability of tropospheric weather regimes in the aftermath of strong or weak vortex events (Baldwin and Dunkerton 2001), a next step would be to look at how the NH SSWs and stratosphere-troposphere coupling are affected by SSO gravity wave drag. To let ICON-ART simulate QBO-like oscillation spontaneously, further tuning of NONGWD is required. Likewise, it is shown that the increase of the NONGWD strength would substantially weaken the SH polar night jet. Recent studies (Polichtchouk et al. 2017; Shepherd et al. 2018; Polichtchouk et al. 2018) pointed out that the NONGWD not only affects polar stratosphere mean states, but also the stratosphere-troposphere coupling. Therefore, an important guide of parameter tuning is to reduce the mean state biases and better represent stratosphere-troposphere coupling processes. Chapter 5 indicates that the tropical zonal winds in the upper stratosphere influenced by NONGWD also influence the polar stratosphere significantly. An interesting question is how much the polar stratosphere is affected by the NONGWD in the extra-tropics, when the influence from the tropics is excluded.

Secondly, here the model simulations are compared against ERA-Interim. It is important to compare the model simulations to more than one reanalysis product, e.g., MERRA2, because of the uncertainties of reanalysis data. We see that the model simulated lower than normal TCO in the Antarctic with respect to ERA-Interim. A next step would be to use satellite observations and limb sounding data to rectify model simulations on ozone or other trace gases.

Thirdly, this thesis focused on stratospheric processes for the long-term integrations. It would be interesting to use seasonal integrations and explore how stratospheric processes affect predictability on surface weather. For instance, what are the impacts of interactive ozone on the simulation of SSW events (polar vortex displacement or split) and their coupling to surface weather, as questions which so far, have not been examined.

References

Albers, J. R., and T. R. Nathan, 2011: Pathways for Communicating the Effects of Stratospheric Ozone to the Polar Vortex: Role of Zonally Asymmetric Ozone. *J. Atmos. Sci.*, **69**, 785–801, doi:10.1175/JAS-D-11-0126.1. https://doi.org/10.1175/JAS-D-11-0126.1.

Alexander, M. J., and Coauthors, 2010: Recent developments in gravity-wave effects in climatemodels and the global distribution of gravity-wavemomentum flux from observations and models. *Q. J. R. Meteorol. Soc.*, **136**, 1103–1124, doi:10.1002/qj.637.

Andrews, D. G., J. R. Holton, and C. B. Leovy, 1987: *Middle atmosphere dynamics*. Academic Press, 489 pp.

Anstey, J. A., and T. G. Shepherd, 2014a: High-latitude influence of the quasi-biennial oscillation. *Q. J. R. Meteorol. Soc.*, **140**, 1–21, doi:10.1002/qj.2132. http://doi.wiley.com/10.1002/qj.2132.

——, and ——, 2014b: High-latitude influence of the quasi-biennial oscillation. *Q. J. R. Meteorol. Soc.*, **140**, 1–21, doi:10.1002/qj.2132. http://doi.wiley.com/10.1002/qj.2132.

——, ——, and J. F. Scinocca, 2010: Influence of the Quasi-Biennial Oscillation on the Extratropical Winter Stratosphere in an Atmospheric General Circulation Model and in Reanalysis Data. *J. Atmos. Sci.*, **67**, 1402–1419, doi:10.1175/2009JAS3292.1. http://journals.ametsoc.org/doi/abs/10.1175/2009JAS3292.1.

Baldwin, M. P., and T. J. Dunkerton, 2001: Stratospheric harbingers of anomalous weather regimes. *Science*, **294**, 581–584, doi:10.1126/science.1063315. http://www.ncbi.nlm.nih.gov/pubmed/11641495.

Baldwin, M. P., and Coauthors, 2001: The quasi-biennial oscillation. *Rev. Geophys.*, **39**, 179–229, doi:10.1029/1999RG000073. http://doi.wiley.com/10.1029/1999RG000073.

Booker, J. R., and F. P. Bretherton, 1967: The critical layer for internal gravity waves in a shear flow. *J. Fluid Mech.*, **27**, 513, doi:10.1017/S0022112067000515. http://www.journals.cambridge.org/abstract_S0022112067000515.

Butchart, N., 2014: The Brewer-Dobson circulation. *Rev. Geophys.*, **52**, 157–184, doi:10.1002/2013RG000448. http://doi.wiley.com/10.1002/2013RG000448.

——, and Coauthors, 2018: Overview of experiment design and comparison of models participating in phase 1 of the SPARC Quasi-Biennial Oscillation initiative (QBOi). *Geosci. Model Dev.*, **11**, 1009–1032, doi:10.5194/gmd-11-1009-2018.

https://www.geosci-model-dev.net/11/1009/2018/.

Charney, J. G., and P. G. Drazin, 1961: Propagation of planetary-scale disturbances from the lower into the upper atmosphere. *J. Geophys. Res.*, **66**, 83–109.

Chiodo, G., and L. M. Polvani, 2017a: Geophysical Research Letters Reduced Southern Hemispheric circulation response to quadrupled CO 2 due to stratospheric ozone feedback. *Geophys. Res. Lett.*, **44**, 465–474, doi:10.1002/2016GL071011. http://www.columbia.edu/~lmp/paps/chiodo+polvani-GRL-2017.pdf.

——, and L. M. Polvani, 2017b: Reduced Southern Hemispheric circulation response to quadrupled CO2due to stratospheric ozone feedback. *Geophys. Res. Lett.*, **44**, 465–474, doi:10.1002/2016GL071011.

Crook, J. A., N. P. Gillett, and S. P. E. Keeley, 2008: Sensitivity of Southern Hemisphere climate to zonal asymmetry in ozone. *Geophys. Res. Lett.*, **35**, n/a-n/a, doi:10.1029/2007GL032698. http://doi.wiley.com/10.1029/2007GL032698.

Crueger, T., and Coauthors, 2018: ICON-A, The Atmosphere Component of the ICON Earth System Model: II. Model Evaluation. *J. Adv. Model. Earth Syst.*, **10**, 1638–1662, doi:10.1029/2017MS001233. http://doi.wiley.com/10.1029/2017MS001233.

Dee, D. P., and Coauthors, 2011: The ERA-Interim reanalysis: Configuration and performance of the data assimilation system. *Q. J. R. Meteorol. Soc.*, doi:10.1002/qj.828.

Dragani, R., 2011: On the quality of the era-interim ozone reanalyses: Comparisons with satellite data. *Q. J. R. Meteorol. Soc.*, **137**, 1312–1326, doi:10.1002/qj.821.

Dragani, R., and Coauthors, 2018: Atmospheric Composition priority developments for Numerical Weather Prediction.

Dunkerton, T. J., and M. P. Baldwin, 1991: Quasi-biennial Modulation of Planetary-Wave Fluxes in the Northern Hemisphere Winter. *J. Atmos. Sci.*, **48**, 1043–1061, doi:10.1175/1520-0469(1991)048<1043:QBMOPW>2.0.CO;2. https://doi.org/10.1175/1520-0469(1991)048%3C1043:QBMOPW%3E2.0.CO.

Eyring, V., and Coauthors, 2006: Assessment of temperature, trace species, and ozone in chemistry-climate model simulations of the recent past. *J. Geophys. Res.*, **111**, D22308, doi:10.1029/2006JD007327. http://doi.wiley.com/10.1029/2006JD007327.

——, and Coauthors, 2013: Long-term ozone changes and associated climate impacts in CMIP5 simulations. *J. Geophys. Res. Atmos.*, **118**, 5029–5060, doi:10.1002/jgrd.50316. http://doi.wiley.com/10.1002/jgrd.50316.

Flemming, J., and Coauthors, 2017: The CAMS interim Reanalysis of Carbon Monoxide, Ozone and Aerosol for 2003-2015. *Atmos. Chem. Phys.*, **17**, 1945–1983, doi:10.5194/acp-17-1945-2017.

Gallagher, B. D., J. Horwitz, J. Perez, R. Preece, F. Imaging, J. Burch, M. Schulz, and H. S. Eds, - *The Stratosphere_ Dynamics, Transport, and Chemistry (2010, American*

Geophysical Union).

Garcia, R. R., D. R. Marsh, D. E. Kinnison, B. A. Boville, and F. Sassi, 2007: Simulation of secular trends in the middle atmosphere, 1950–2003. *J. Geophys. Res.*, **112**, D09301, doi:10.1029/2006JD007485. http://doi.wiley.com/10.1029/2006JD007485.

Garfinkel, C., and D. L. Hartmann, 2011: The Influence of the Quasi-Biennial Oscillation on the Troposphere in Wintertime in a Hierarchy of Models, Part I: Simplified Dry GCMs. *J. Atmos. Sci.*, **68**, 1273–1289, doi:10.1175/2011JAS3665.1. http://journals.ametsoc.org/doi/abs/10.1175/2011JAS3665.1.

Garfinkel, C. I., T. A. Shaw, D. L. Hartmann, and D. W. Waugh, 2012: Does the Holton–Tan Mechanism Explain How the Quasi-Biennial Oscillation Modulates the Arctic Polar Vortex? *J. Atmos. Sci.*, **69**, 1713–1733, doi:10.1175/JAS-D-11-0209.1. http://journals.ametsoc.org/doi/abs/10.1175/JAS-D-11-0209.1.

Geller, M. A., and Coauthors, 2013: A comparison between gravity wave momentum fluxes in observations and climate models. *J. Clim.*, **26**, 6383–6405, doi:10.1175/JCLI-D-12-00545.1.

Gillett, N. P., J. F. Scinocca, D. A. Plummer, and M. C. Reader, 2009: Sensitivity of climate to dynamically-consistent zonal asymmetries in ozone. *Geophys. Res. Lett.*, **36**, L10809, doi:10.1029/2009GL037246. http://doi.wiley.com/10.1029/2009GL037246.

Giorgetta, M. A., and Coauthors, 2018: ICON-A, the Atmosphere Component of the ICON Earth System Model: I. Model Description. *J. Adv. Model. Earth Syst.*, **10**, 1613–1637, doi:10.1029/2017MS001242. http://doi.wiley.com/10.1029/2017MS001242.

Gray, L. J., 2003: The influence of the equatorial upper stratosphere on stratospheric sudden warmings. *Geophys. Res. Lett.*, **30**, 30–33, doi:10.1029/2002GL016430.

Gray, L. J., E. F. Drysdale, B. N. Lawrence, and T. J. Dunkerton, 2001a: Model studies of the interannual variability of the northern-hemisphere stratospheric winter circulation: The role of the quasi-biennial oscillation. *Q. J. R. Meteorol. Soc.*, **127**, 1413–1432.

——, S. J. Phipps, T. J. Dunkerton, M. P. Baldwin, E. F. Drysdale, and M. R. Allen, 2001b: A data study of the influence of the equatorial upper stratosphere on northern-hemisphere stratospheric sudden warmings. *Q. J. R. Meteorol. Soc.*, **127**, 1985–2003.

Gray, L. J., S. Crooks, C. Pascoe, S. Sparrow, and M. Palmer, 2004: Solar and QBO Influences on the Timing of Stratospheric Sudden Warmings. *J. Atmos. Sci.*, **61**, 2777–2796, doi:10.1175/JAS-3297.1. http://journals.ametsoc.org/doi/abs/10.1175/JAS-3297.1.

Haase, S., and K. Matthes, 2018: The importance of interactive chemistry for stratosphere–troposphere–coupling. *Atmos. Chem. Phys. Discuss.*, 1–27, doi:10.5194/acp-2018-1052.

——, ——, M. Latif, and N. E. Omrani, 2018: The importance of a properly represented stratosphere for Northern Hemisphere surface variability in the atmosphere and the ocean. *J. Clim.*, **31**, 8481–8497, doi:10.1175/JCLI-D-17-0520.1.

Hamilton, K., 1998: Effects of an Imposed Quasi-Biennial Oscillation in a Comprehensive

Troposphere–Stratosphere–Mesosphere General Circulation Model. *J. Atmos. Sci.*, **55**, 2393–2418, doi:10.1175/1520-0469(1998)055<2393:EOAIQB>2.0.CO;2. https://doi.org/10.1175/1520-0469(1998)055%3C2393:EOAIQB%3E2.0.CO.

Hansen, F., K. Matthes, and L. J. Gray, 2013: Sensitivity of stratospheric dynamics and chemistry to QBO nudging width in the chemistry-climate model WACCM. *J. Geophys. Res. Atmos.*, **118**, 10,464-10,474, doi:10.1002/jgrd.50812. http://doi.wiley.com/10.1002/jgrd.50812.

Hardiman, S. C., N. Butchart, S. M. Osprey, L. J. Gray, A. C. Bushell, and T. J. Hinton, 2010: The Climatology of the Middle Atmosphere in a Vertically Extended Version of the Met Officeś Climate Model. Part I: Mean State. *J. Atmos. Sci.*, **67(5)**, 1509–1525, doi:10.1175/2009JAS3337.1.

Haynes, P. H., M. E. McIntyre, T. G. Shepherd, C. J. Marks, and K. P. Shine, 1991: On the "Downward Control" of Extratropical Diabatic Circulations by Eddy-Induced Mean Zonal Forces. *J. Atmos. Sci.*, **48**, 651–678, doi:10.1175/1520-0469(1991)048<0651:OTCOED>2.0.CO;2. https://doi.org/10.1175/1520-0469(1991)048%3C0651:OTCOED%3E2.0.CO.

Hendon, H. H., and M. C. Wheeler, 2008: Some Space–Time Spectral Analyses of Tropical Convection and Planetary-Scale Waves. *J. Atmos. Sci.*, **65**, 2936–2948, doi:10.1175/2008JAS2675.1. http://journals.ametsoc.org/doi/abs/10.1175/2008JAS2675.1.

Hines, C. O., 1997a: Doppler-spread parameterization of gravity-wave momentum deposition in the middle atmosphere. Part 2: Broad and quasi monochromatic spectra, and implementation. *J. Atmos. Solar-Terrestrial Phys.*, **59**, 387–400.

——, 1997b: Doppler-spread parameterization of gravity-wave momentum deposition in the middle atmosphere. Part 1: Basic formulation. *J. Atmos. Solar-Terrestrial Phys.*, **59**, 371–386.

Hollingsworth, A., and Coauthors, 2008: TOWARD A MONITORING AND FORECASTING SYSTEM FOR ATMOSPHERIC COMPOSITION. *Bull. Am. Meteorol. Soc.*, **89**, 1147–1164, doi:10.1175/2008BAMS2355.1. https://doi.org/10.1175/2008BAMS2355.1.

Holton, J. R., and R. S. Lindzen, 1972: An Updated Theory for the Quasi-Biennial Cycle of the Tropical Stratosphere. *J. Atmos. Sci.*, **29**, 1076–1080, doi:10.1175/1520-0469(1972)029<1076:AUTFTQ>2.0.CO;2. http://journals.ametsoc.org/doi/abs/10.1175/1520-0469%281972%29029%3C1076%3AAUTFTQ%3E2.0.CO%3B2.

——, and H.-C. Tan, 1980: The Influence of the Equatorial Quasi-Biennial Oscillation on the Global Circulation at 50 mb. *J. Atmos. Sci.*, **37**, 2200–2208, doi:10.1175/1520-0469(1980)037<2200:TIOTEQ>2.0.CO;2. http://journals.ametsoc.org/doi/abs/10.1175/1520-0469%281980%29037%3C2200%3ATIOTEQ%3E2.0.CO%3B2.

Holton, J. R., and H.-C. Tan, 1982: The quasi-biennial oscillation in the Northern Hemisphere lower stratosphere. *J. Meteorol. Soc. Japan. Ser. II*, **60**, 140–148.

Hoskins, B. J., and D. J. Karoly, 1981: The Steady Linear Response of a Spherical Atmosphere to Thermal and Orographic Forcing. *J. Atmos. Sci.*, **38**, 1179–1196, doi:10.1175/1520-0469(1981)038<1179:TSLROA>2.0.CO;2. https://doi.org/10.1175/1520-0469(1981)038%3C1179:TSLROA%3E2.0.CO.

Hu, Y., and K. K. Tung, 2002: Tropospheric and equatorial influences on planetary-wave amplitude in the stratosphere. *Geophys. Res. Lett.*, **29**, doi:10.1029/2001GL013762.

Hurwitz, M. M., P. A. Newman, F. Li, L. D. Oman, O. Morgenstern, P. Braesicke, and J. A. Pyle, 2010: Assessment of the breakup of the Antarctic polar vortex in two new chemistry-climate models. *J. Geophys. Res.*, **115**, D07105, doi:10.1029/2009JD012788. http://doi.wiley.com/10.1029/2009JD012788.

——, P. Braesicke, and J. A. Pyle, 2011: Sensitivity of the mid-winter Arctic stratosphere to QBO width in a simplified chemistry-climate model. *Atmos. Sci. Lett.*, **12**, 268–272, doi:10.1002/asl.330. http://doi.wiley.com/10.1002/asl.330.

Karoly, D. J., 1989: Southern Hemisphere Circulation Features Associated with El Niño-Southern Oscillation Events. *J. Clim.*, **2**, 1239–1252, doi:10.1175/1520-0442(1989)002<1239:SHCFAW>2.0.CO;2. https://doi.org/10.1175/1520-0442(1989)002%3C1239:SHCFAW%3E2.0.CO.

Kawatani, Y., S. Watanabe, K. Sato, T. J. Dunkerton, S. Miyahara, and M. Takahashi, 2010: The Roles of Equatorial Trapped Waves and Internal Inertia–Gravity Waves in Driving the Quasi-Biennial Oscillation. Part I: Zonal Mean Wave Forcing. *J. Atmos. Sci.*, **67**, 981–997, doi:10.1175/2009JAS3223.1. http://journals.ametsoc.org/doi/abs/10.1175/2009JAS3222.1.

Keeble, J., P. Braesicke, N. L. Abraham, H. K. Roscoe, and J. A. Pyle, 2014: The impact of polar stratospheric ozone loss on southern Hemisphere stratospheric circulation and climate. *Atmos. Chem. Phys.*, **14**, 13705–13717, doi:10.5194/acp-14-13705-2014.

Kidston, J., A. A. Scaife, S. C. Hardiman, D. M. Mitchell, N. Butchart, M. P. Baldwin, and L. J. Gray, 2015: Stratospheric influence on tropospheric jet streams, storm tracks and surface weather. *Nat. Geosci.*, **8**, 433–440, doi:10.1038/ngeo2424. http://www.nature.com/articles/ngeo2424.

Kiladis, G. N., M. C. Wheeler, P. T. Haertel, K. H. Straub, and P. E. Roundy, 2009: Convectively coupled equatorial waves. *Rev. Geophys.*, **47**, 1–42, doi:10.1029/2008RG000266.

Kim, Y. H., and H. Y. Chun, 2015: Momentum forcing of the quasi-biennial oscillation by equatorial waves in recent reanalyses. *Atmos. Chem. Phys.*, **15**, 6577–6587, doi:10.5194/acp-15-6577-2015. http://www.atmos-chem-phys.net/15/6577/2015/.

Labitzke, K., 1987: Sunspots, the QBO, and the stratospheric temperature in the north polar region. *Geophys. Res. Lett.*, **14**, 535–537, doi:10.1029/GL014i005p00535. http://doi.wiley.com/10.1029/GL014i005p00535.

——, M. Kunze, and S. Brönnimann, 2006: Sunspots, the QBO and the stratosphere in the North Polar Region 20 years later. *Meteorol. Zeitschrift*, **15**, 355–363, doi:10.1127/0941-2948/2006/0136. http://dx.doi.org/10.1127/0941-2948/2006/0136.

Li, F., Y. V. Vikhliaev, P. A. Newman, S. Pawson, J. Perlwitz, D. W. Waugh, and A. R. Douglass, 2016: Impacts of interactive stratospheric chemistry on Antarctic and Southern Ocean climate change in the Goddard Earth Observing System, version 5 (GEOS-5). *J. Clim.*, **29**, 3199–3218, doi:10.1175/JCLI-D-15-0572.1.

Lin, P., D. Paynter, L. Polvani, G. J. P. Correa, Y. Ming, and V. Ramaswamy, 2017a: Dependence of model-simulated response to ozone depletion on stratospheric polar vortex climatology. *Geophys. Res. Lett.*, **44**, 6391–6398, doi:10.1002/2017GL073862. http://doi.wiley.com/10.1002/2017GL073862.

——, ——, ——, ——, ——, and ——, 2017b: Dependence of model-simulated response to ozone depletion on stratospheric polar vortex climatology. *Geophys. Res. Lett.*, **44**, 6391–6398, doi:10.1002/2017GL073862. http://doi.wiley.com/10.1002/2017GL073862.

Lindzen, R. S., 1987: On the Development of the Theory of the QBO. *Bull. Am. Meteorol. Soc.*, **68**, 329–337, doi:10.1175/1520-0477(1987)068<0329:OTDOTT>2.0.CO;2. https://doi.org/10.1175/1520-0477(1987)068%3C0329:OTDOTT%3E2.0.CO.

Lindzen, R. S., and J. R. Holton, 1968: A Theory of the Quasi-Biennial Oscillation. *J. Atmos. Sci.*, **25**, 1095–1107, doi:10.1175/1520-0469(1968)025<1095:ATOTQB>2.0.CO;2. http://journals.ametsoc.org/doi/abs/10.1175/1520-0469%281968%29025%3C1095%3AATOTQB%3E2.0.CO%3B2.

Liu, Y., C. Lu, Y. Wang, and E. Kyrölä, 2011: The quasi-biennial and semi-annual oscillation features of tropical O3, NO2, and NO3 revealed by GOMOS satellite observations for 2002–2008. *Chinese Sci. Bull.*, **56**, 1921–1929, doi:10.1007/s11434-011-4519-7. http://link.springer.com/10.1007/s11434-011-4519-7.

Lott, F., and M. J. Miller, 1997: A new subgrid-scale orographic drag parametrization: Its formulation and testing. *Q. J. R. Meteorol. Soc.*, **123**, 101–127.

Lott, F., and Coauthors, 2014: Kelvin and rossby-gravity wave packets in the lower stratosphere of some high-top CMIP5 models. *J. Geophys. Res.*, **119**, 2156–2173, doi:10.1002/2013JD020797. http://doi.wiley.com/10.1002/2013JD020797.

Lu, H., M. P. Baldwin, L. J. Gray, and M. J. Jarvis, 2008: Decadal-scale changes in the effect of the QBO on the northern stratospheric polar vortex. *J. Geophys. Res.*, **113**, D10114, doi:10.1029/2007JD009647. http://doi.wiley.com/10.1029/2007JD009647.

——, T. J. Bracegirdle, T. Phillips, A. Bushell, and L. Gray, 2014: Mechanisms for the Holton-Tan relationship and its decadal variation. *J. Geophys. Res.*, **119**, 2811–2830, doi:10.1002/2013JD021352. http://doi.wiley.com/10.1002/2013JD021352.

Manzini, E., B. Steil, C. Brühl, M. A. Giorgetta, and K. Krüger, 2003a: A new interactive chemistry-climate model: 2. Sensitivity of the middle atmosphere to ozone depletion and

increase in greenhouse gases and implications for recent stratospheric cooling. *J. Geophys. Res.*, **108**, 4429, doi:10.1029/2002JD002977. http://doi.wiley.com/10.1029/2002JD002977.

——, ——, ——, ——, and ——, 2003b: A new interactive chemistry-climate model: 2. Sensitivity of the middle atmosphere to ozone depletion and increase in greenhouse gases and implications for recent stratospheric cooling. *J. Geophys. Res.*, **108**, 4429, doi:10.1029/2002JD002977. http://doi.wiley.com/10.1029/2002JD002977.

Martineau, P., S. Son, M. Taguchi, and A. H. Butler, 2017: A comparison of the momentum budget in reanalysis datasets during sudden stratospheric warming events. *Atmos. Chem. Phys. Discuss.*, 1–31, doi:10.5194/acp-2017-837. https://www.atmos-chem-phys-discuss.net/acp-2017-837/.

——, J. S. Wright, N. Zhu, and M. Fujiwara, 2018: Zonal-mean data set of global atmospheric reanalyses on pressure levels. *Earth Syst. Sci. Data*, **10**, 1925–1941, doi:10.5194/essd-10-1925-2018.

Matsuno, T., 1966: Quasi-Geostrophic Motions in the Equatorial Area. *J. Meteorol. Soc. Japan. Ser. II*, **44**, 25–43, doi:10.2151/jmsj1965.44.1_25. https://www.jstage.jst.go.jp/article/jmsj1965/44/1/44_1_25/_article.

Matthes, K., D. R. Marsh, R. R. Garcia, D. E. Kinnison, F. Sassi, and S. Walters, 2010: Role of the QBO in modulating the influence of the 11 year solar cycle on the atmosphere using constant forcings. *J. Geophys. Res. Atmos.*, **115**, D18110, doi:10.1029/2009JD013020. http://doi.wiley.com/10.1029/2009JD013020.

Mauritsen, T., and G. Svensson, 2007: Observations of Stably Stratified Shear-Driven Atmospheric Turbulence at Low and High Richardson Numbers. *J. Atmos. Sci.*, **64**, 645–655, doi:10.1175/JAS3856.1. http://journals.ametsoc.org/doi/abs/10.1175/JAS3856.1.

McLandress, C., T. G. Shepherd, S. Polavarapu, and S. R. Beagley, 2011: Is Missing Orographic Gravity Wave Drag near 60°S the Cause of the Stratospheric Zonal Wind Biases in Chemistry–Climate Models? *J. Atmos. Sci.*, **69**, 802–818, doi:10.1175/JAS-D-11-0159.1. https://doi.org/10.1175/JAS-D-11-0159.1.

McLinden, C. A., S. C. Olsen, B. Hannegan, O. Wild, M. J. Prather, and J. Sundet, 2000: Stratospheric ozone in 3-D models: A simple chemistry and the cross-tropopause flux. *J. Geophys. Res. Atmos.*, **105**, 14653–14665, doi:10.1029/2000JD900124. http://doi.wiley.com/10.1029/2000JD900124.

Müller, W. A., and Coauthors, 2018: A Higher-resolution Version of the Max Planck Institute Earth System Model (MPI-ESM1.2-HR). *J. Adv. Model. Earth Syst.*, **10**, 1383–1413, doi:10.1029/2017MS001217. http://doi.wiley.com/10.1029/2017MS001217.

Neely, R. R., D. R. Marsh, K. L. Smith, S. M. Davis, and L. M. Polvani, 2014: Biases in southern hemisphere climate trends induced by coarsely specifying the temporal resolution of stratospheric ozone. *Geophys. Res. Lett.*, **41**, 8602–8610, doi:10.1002/2014GL061627. http://doi.wiley.com/10.1002/2014GL061627.

Nordeng, T.-E., 1994: Extended versions of the convective parametrization scheme at ECMWF

and their impact on the mean and transient activity of the model in the tropics. *ECMWF Tech. Memo*.

North, G. R., J. A. Pyle, and F. Zhang, 2014: *Encyclopedia of atmospheric sciences*. Elsevier,.

Nowack, P., P. Braesicke, J. Haigh, N. L. Abraham, J. Pyle, and A. Voulgarakis, 2018a: Using machine learning to build temperature-based ozone parameterizations for climate sensitivity simulations. *Environ. Res. Lett.*, **13**, doi:10.1088/1748-9326/aae2be.

Nowack, P. J., N. Luke Abraham, A. C. Maycock, P. Braesicke, J. M. Gregory, M. M. Joshi, A. Osprey, and J. A. Pyle, 2015: A large ozone-circulation feedback and its implications for global warming assessments. *Nat. Clim. Chang.*, **5**, 41–45, doi:10.1038/nclimate2451.

——, P. Braesicke, N. Luke Abraham, and J. A. Pyle, 2017: On the role of ozone feedback in the ENSO amplitude response under global warming. *Geophys. Res. Lett.*, **44**, 3858–3866, doi:10.1002/2016GL072418.

——, N. L. Abraham, P. Braesicke, and J. A. Pyle, 2018b: The Impact of Stratospheric Ozone Feedbacks on Climate Sensitivity Estimates. *J. Geophys. Res. Atmos.*, **123**, 4630–4641, doi:10.1002/2017JD027943.

Ohfuchi, W., and K. Hamilton, 2010: High resolution numerical modelling of the atmosphere and ocean.

Palmer, T. N., G. J. Shutts, and R. Swinbank, 1986: Alleviation of a systematic westerly bias in general circulation and numerical weather prediction models through an orographic gravity wave drag parametrization. *Q. J. R. Meteorol. Soc.*, **112**, 1001–1039, doi:10.1002/qj.49711247406. http://doi.wiley.com/10.1002/qj.49711247406.

Pascoe, C. L., L. J. Gray, S. A. Crooks, M. N. Juckes, and M. P. Baldwin, 2005: The quasi-biennial oscillation: Analysis using ERA-40 data. *J. Geophys. Res. D Atmos.*, **110**, 1–13, doi:10.1029/2004JD004941.

——, L. J. Gray, and A. A. Scaife, 2006: A GCM study of the influence of equatorial winds on the timing of sudden stratospheric warmings. *Geophys. Res. Lett.*, **33**, 33–36, doi:10.1029/2005GL024715.

Perlwitz, J., S. Pawson, R. L. Fogt, J. E. Nielsen, and W. D. Neff, 2008: Impact of stratospheric ozone hole recovery on Antarctic climate. *Geophys. Res. Lett.*, **35**, L08714, doi:10.1029/2008GL033317. http://doi.wiley.com/10.1029/2008GL033317.

Peters, D. H. W., A. Schneidereit, M. Bügelmayer, C. Zülicke, and I. Kirchner, 2015: Atmospheric circulation changes in response to an observed stratospheric zonal ozone anomaly. *Atmos. - Ocean*, **53**, 74–88, doi:10.1080/07055900.2013.878833. http://dx.doi.org/10.1080/07055900.2013.878833.

Pincus, R., and B. Stevens, 2013: Paths to accuracy for radiation parameterizations in atmospheric models. *J. Adv. Model. Earth Syst.*, **5**, 225–233, doi:10.1002/jame.20027.

Plumb, R. A., and A. D. McEwan, 1978: The Instability of a Forced Standing Wave in a

Viscous Stratified Fluid: A Laboratory Analogue of .the Quasi-Biennial Oscillation. *J. Atmos. Sci.*, **35**, 1827–1839, doi:10.1175/1520-0469(1978)035<1827:TIOAFS>2.0.CO;2. https://doi.org/10.1175/1520-0469(1978)035%3C1827:TIOAFS%3E2.0.CO.

Polichtchouk, I., R. J. Hogan, T. G. Shepherd, P. Bechtold, T. Stockdale, S. Malardel, S. Lock, and L. Magnusson, 2017: What influences the middle atmosphere circulation in the IFS? *ECMWF Tech. Memo.*, **809**.

——, T. G. Shepherd, and N. J. Byrne, 2018: Impact of Parametrized Nonorographic Gravity Wave Drag on Stratosphere-Troposphere Coupling in the Northern and Southern Hemispheres. *Geophys. Res. Lett.*, **45**, 8612–8618, doi:10.1029/2018GL078981.

Pyle, J. A., P. Braesicke, and G. Zeng, 2005: Dynamical variability in the modelling of chemistry-climate interactions. *Faraday Discuss.*, **130**, 27–39, doi:10.1039/b417947c.

Rae, C. D., J. Keeble, P. Hitchcock, and J. A. Pyle, 2019: Prescribing Zonally Asymmetric Ozone Climatologies in Climate Models: Performance Compared to a Chemistry-Climate Model. *J. Adv. Model. Earth Syst.*, 2018MS001478, doi:10.1029/2018MS001478. https://onlinelibrary.wiley.com/doi/abs/10.1029/2018MS001478.

Randel, W. J., and F. Wu, 1999: Cooling of the Arctic and Antarctic Polar Stratospheres due to Ozone Depletion. *J. Clim.*, **12**, 1467–1479, doi:10.1175/1520-0442(1999)012<1467:COTAAA>2.0.CO;2. https://doi.org/10.1175/1520-0442(1999)012%3C1467:COTAAA%3E2.0.CO.

Rieger, D., and Coauthors, 2015: ICON-ART 1.0 - A new online-coupled model system from the global to regional scale. *Geosci. Model Dev.*, **8**, 1659–1676, doi:10.5194/gmd-8-1659-2015.

Riese, M., F. Ploeger, A. Rap, B. Vogel, P. Konopka, M. Dameris, and P. Forster, 2012: Impact of uncertainties in atmospheric mixing on simulated UTLS composition and related radiative effects. *J. Geophys. Res. Atmos.*, **117**, 1–10, doi:10.1029/2012JD017751.

Salby, M. L., 2012: *Physics of the Atmosphere and Climate*. Cambridge University Press.

——, E. A. Titova, and L. Deschamps, 2012: Changes of the Antarctic ozone hole: Controlling mechanisms, seasonal predictability, and evolution. *J. Geophys. Res. Atmos.*, **117**, 1–11, doi:10.1029/2011JD016285.

Sassi, F., B. A. Boville, D. Kinnison, and R. R. Garcia, 2005: The effects of interactive ozone chemistry on simulations of the middle atmosphere. *Geophys. Res. Lett.*, **32**, 1–5, doi:10.1029/2004GL022131.

Scaife, A. A., N. Butchart, C. D. Warner, D. Stainforth, W. Norton, and J. Austin, 2000: Realistic quasi-biennial oscillations in a simulation of the global climate. *Geophys. Res. Lett.*, **27**, 3481–3484, doi:10.1029/2000GL011625. http://doi.wiley.com/10.1029/2000GL011625.

Schröter, J., and Coauthors, 2018: ICON-ART 2.1 - A flexible tracer framework and its application for composition studies in numerical weather forecasting and climate

simulations. *Geosci. Model Dev. Discuss.*, 1–37, doi:10.5194/gmd-2017-286. https://www.geosci-model-dev-discuss.net/gmd-2017-286/.

Shepherd, T. G., I. Polichtchouk, R. J. Hogan, and A. J. Simmons, 2018: Report on Stratosphere Task Force. *ECMWF Tech. Memo.*, **824**.

Sheshadri, A., R. A. Plumb, and D. I. V Domeisen, 2013: Can the Delay in Antarctic Polar Vortex Breakup Explain Recent Trends in Surface Westerlies? *J. Atmos. Sci.*, **71**, 566–573, doi:10.1175/JAS-D-12-0343.1. https://doi.org/10.1175/JAS-D-12-0343.1.

Son, S.-W., N. F. Tandon, L. M. Polvani, and D. W. Waugh, 2009: Ozone hole and Southern Hemisphere climate change. *Geophys. Res. Lett.*, **36**, n/a-n/a, doi:10.1029/2009GL038671. http://doi.wiley.com/10.1029/2009GL038671.

Stevens, B., and Coauthors, 2013: Atmospheric component of the MPI-M earth system model: ECHAM6. *J. Adv. Model. Earth Syst.*, **5**, 146–172, doi:10.1002/jame.20015.

Thompson, D. W. J., and J. M. Wallace, 2000: Annular Modes in the Extratropical Circulation. Part I: Month-to-Month Variability. *J. Clim.*, **13**, 1000–1016, doi:10.1175/1520-0442(2000)013<1000:AMITEC>2.0.CO;2. https://doi.org/10.1175/1520-0442(2000)013%3C1000:AMITEC%3E2.0.CO.

Thompson, D. W. J., S. Solomon, P. J. Kushner, M. H. England, K. M. Grise, and D. J. Karoly, 2011: Signatures of the Antarctic ozone hole in Southern Hemisphere surface climate change. *Nat. Geosci.*, **4**, 741–749, doi:10.1038/ngeo1296. http://dx.doi.org/10.1038/ngeo1296.

Tung, K.-K., Y. L. Yung, X. Jiang, L. Kuai, and R.-L. Shia, 2008: Nonstationary Synchronization of Equatorial QBO with SAO in Observations and a Model. *J. Atmos. Sci.*, **66**, 1654–1664, doi:10.1175/2008jas2857.1.

Wan, H., and Coauthors, 2013: The ICON-1.2 hydrostatic atmospheric dynamical core on triangular grids – Part 1: Formulation and performance of the baseline version. *Geosci. Model Dev.*, **6**, 735–763, doi:10.5194/gmd-6-735-2013. https://www.geosci-model-dev.net/6/735/2013/.

Waugh, D. W., L. Oman, P. A. Newman, R. S. Stolarski, S. Pawson, J. E. Nielsen, and J. Perlwitz, 2009a: Effect of zonal asymmetries in stratospheric ozone on simulated Southern Hemisphere climate trends. *Geophys. Res. Lett.*, **36**, L18701, doi:10.1029/2009gl040419. http://doi.wiley.com/10.1029/2009GL040419.

——, ——, ——, ——, ——, ——, and ——, 2009b: Effect of zonal asymmetries in stratospheric ozone on simulated Southern Hemisphere climate trends. *Geophys. Res. Lett.*, **36**, L18701, doi:10.1029/2009GL040419. http://doi.wiley.com/10.1029/2009GL040419.

Waugh, D. W., A. H. Sobel, and L. M. Polvani, 2016: What Is the Polar Vortex and How Does It Influence Weather? *Bull. Am. Meteorol. Soc.*, **98**, 37–44, doi:10.1175/BAMS-D-15-00212.1. https://doi.org/10.1175/BAMS-D-15-00212.1.

Wells, H., 2015: Forecasting Research Technical Report 600: The 5A Orographic Drag Scheme: Design and Testing. 60.

WMO (World Meteorological Organization), Scientific Assessment of Ozone Depletion: 2018, Global Ozone Research and Monitoring Project — Report No. 58, 588 pp., Geneva, Switzerland, 2018.

Yamashita, Y., H. Akiyoshi, and M. Takahashi, 2011: Dynamical response in the Northern Hemisphere midlatitude and high-latitude winter to the QBO simulated by CCSR/NIES CCM. *J. Geophys. Res. Atmos.*, **116**, 1–9, doi:10.1029/2010JD015016.

Zängl, G., D. Reinert, P. Rípodas, and M. Baldauf, 2015: The ICON (ICOsahedral Non-hydrostatic) modelling framework of DWD and MPI-M: Description of the non-hydrostatic dynamical core. *Q. J. R. Meteorol. Soc.*, **141**, 563–579, doi:10.1002/qj.2378.

Zhang, J., W. Tian, F. Xie, W. Sang, D. Guo, M. Chipperfield, W. Feng, and D. Hu, 2019: Zonally asymmetric trends of winter total column ozone in the northern middle latitudes. *Clim. Dyn.*, **52**, 4483–4500, doi:10.1007/s00382-018-4393-y. https://doi.org/10.1007/s00382-018-4393-y.

Appendix A Diagnostics

TEM equation and dynamical heating rate are introduced.

A.1 Transformed Eulerian Mean (TEM)

The TEM equation is commonly used to diagnose wave-mean-flow interaction in the middle atmosphere. According to Andrews et al. (1987), in log-pressure coordinate, the TEM equation is expressed as

$$\frac{\partial \bar{u}}{\partial t} = \bar{v}^* \left[f - \frac{1}{a cos\phi} \frac{\partial (\bar{u} cos\phi)}{\partial \phi} \right] - \bar{w}^* \frac{\partial \bar{u}}{\partial z} + \frac{1}{\rho_0 a cos\phi} \nabla \cdot F + \bar{X} \, . \quad \text{(A1)}$$

The overbar indicates the zonal-mean; ρ_0, f and a are air density, the Coriolis parameter and Earth's radius; z and ϕ are log-pressure height and meridional radian. As shown in (A1), the zonal wind tendency is decomposed into four terms. The first and second terms represents the acceleration associated with the residual mean circulation $(\bar{v}^*, \bar{w}^*)$, where the vector $(\bar{v}^*, \bar{w}^*)$ is defined by

$$\bar{v}^* = \bar{v} - \frac{1}{\rho_0} \frac{\partial}{\partial z} \left[\frac{\rho_0 \overline{v'\theta'}}{\partial \bar{\theta} / \partial z} \right],$$

$$\bar{w}^* = \bar{w} + \frac{1}{a cos\phi} \frac{\partial}{\partial \phi} \left[\frac{cos\phi \overline{v'\theta'}}{\partial \bar{\theta} / \partial z} \right].$$

Here, $\bar{v}$, $\bar{w}$ and $\bar{\theta}$ are zonal mean meridional wind, vertical wind and potential temperature; the notation prime indicates zonal derivation; $\overline{v'\theta'}$ represents eddy heat transport.

In equation (A1), the third term $\nabla \cdot F$ is the Eliassen-Palm (EP) flux divergence, which is expressed as

$$\nabla \cdot F = \frac{1}{a\cos\phi}\frac{\partial(F_\phi \cos\phi)}{\partial\phi} + \frac{\partial Fz}{\partial z}\,.$$

And the EP flux vector is defined by

$$F_\phi = \rho_0 a\cos\phi\left(\frac{\overline{v'\theta'}}{\partial\bar{\theta}/\partial z}\frac{\partial\bar{u}}{\partial z} - \overline{u'v'}\right),$$

$$F_z = \rho_0 a\cos\phi\left[\frac{\overline{v\prime\theta\prime}}{\partial\bar{\theta}/\partial z}\left(f - \frac{1}{a\cos\phi}\frac{\partial(\bar{u}\cos\phi)}{\partial\phi}\right) - \overline{u'w'}\right],$$

where $\overline{u'v'}$ and $\overline{u'w'}$ are meridional and vertical eddy momentum transport. Because it is proved that the vector F describes the propagation of wave activity (e.g., Andrews et al. (1987)), negative values of $\nabla \cdot F$ represent a westward drag on the mean flow as a result of wave absorption by the mean flow. The last term $\bar{X}$ represents the residual, such as small-scale gravity wave drag.

The quasi-geostrophic (QG) version of the TEM is also commonly used, which suffices to diagnose large scale wave-mean-flow interaction at extra-tropics (Martineau et al. 2017). Under QG approximation, the TEM equation is formulated as

$$\frac{\partial\bar{u}}{\partial t} = f\bar{v}^* + \frac{1}{\rho_0 a\cos\phi}\nabla \cdot F_{QG} + \bar{X}\,,$$

where the EP flux vector is simplified to

$$F_{QG} = [F_\phi, F_p] = \rho_0 a\cos\phi\left[-\overline{u'v'}, \frac{\overline{v\prime\theta\prime}}{\partial\bar{\theta}/\partial z}f\right].$$

A.2 Dynamical heating rate

According to Martineau et al. (2018), zonal mean temperature tendency in pressure coordinate is written as

$$\frac{\partial\bar{\theta}}{\partial t} + \frac{\bar{v}}{a}\frac{\partial\bar{\theta}}{\partial\phi} + \bar{\omega}\frac{\partial\bar{\theta}}{\partial p} + \frac{1}{a\cos\phi}\frac{\partial(\overline{v\prime\theta\prime}\cos\phi)}{\partial\phi} + \frac{\partial(\overline{\omega\prime\theta\prime})}{\partial p} + \bar{X} = \overline{\frac{\theta}{C_p T}\dot{Q}}\,,$$

where $\overline{\frac{\theta}{C_p T}\dot{Q}}$ is the diabatic heating rate (such as longwave and shortwave radiation), $\bar{X}$ is the residual, ω is the vertical velocity in pressure coordinate ($\omega = \frac{dp}{dt}$). The dynamical heating rate in this thesis is defined by

$$temp\_dyn = \frac{\bar{v}}{a}\frac{\partial\bar{\theta}}{\partial\phi} + \bar{\omega}\frac{\partial\bar{\theta}}{\partial p} + \frac{1}{a\cos\phi}\frac{\partial(\overline{v\prime\theta\prime}\cos\phi)}{\partial\phi} + \frac{\partial(\overline{\omega\prime\theta\prime})}{\partial p}. \quad \text{(A2)}$$

In equation (A2), the dynamical heating rate ($temp\_dyn$) includes mean meridional heat transport (first and second terms), and eddy heat transport (third and fourth terms).

A.3 Conversions

(1) Potential temperature and temperature:

$$\theta = T\left(\frac{p_0}{p}\right)^{R_d/C_p},$$

where T and p are temperature and pressure; R_d, C_p and p_0 are the gas constant for dry air (287), the specific heat (1004) and reference pressure (1000 hPa).

(2) Vertical velocity in log-pressure coordinate and pressure coordinate:

$$w = -\frac{H}{p}\omega ,$$

where H is scale height (= 7 km).

Appendix B Equatorial wave spectral analysis

Based on shallow water equations, I'll introduce equatorial waves and how to apply spectral analysis.

B.1 Equatorial wave theory

Equatorial waves, which propagate vertically from troposphere into the stratosphere, are one of the essential ingredients in forcing the QBO. The theoretical equatorial waves are obtained from shallow water equations (Matsuno 1966). The shallow water equations are formulated,

$$\frac{\partial u}{\partial t} - fv + g\frac{\partial h}{\partial x} = 0.$$

$$\frac{\partial v}{\partial t} + fu + g\frac{\partial h}{\partial y} = 0.$$

$$\frac{\partial h}{\partial t} + ghe\left(\frac{\partial u}{\partial x} + \frac{\partial v}{\partial y}\right) = 0.$$

Here, u and v are the zonal and meridional wind; h, he, g and f are the geopotential height, the equivalent depth, magnitude of gravity and Coriolis parameter, which is approximated by $f = \beta y$ ($\beta = \frac{df}{dy}$, variation of the f with latitude). Assuming zonally propagation wave solutions

$$\begin{pmatrix} u \\ v \\ h \end{pmatrix} = \begin{pmatrix} \hat{u}(y) \\ \hat{v}(y) \\ \hat{h}(y) \end{pmatrix} \exp[i(kx - \omega t)],$$

where k is the zonal wave number and ω is the wave frequency, and substituting this equation into the shallow water equations, this yields,

$$\frac{d\hat{v}^2}{dy^2} + \left(\frac{\omega^2}{ghe} - k^2 - \frac{k}{\omega}\beta - \frac{\beta^2 y^2}{ghe}\right)\hat{v} = 0.$$

In order to have solutions for the above second-order differential equation, it must satisfy

$$\frac{\sqrt{ghe}}{\beta}\left(\frac{\omega^2}{ghe} - k^2 - \frac{k}{\omega}\beta\right) = 2m + 1; m = 0, 1, 2, \ldots$$

This equation gives the dispersion relationships for equatorial waves, relating wave number and wave frequency. The dispersion curves for equatorial waves are displayed in Figure B1. The gravity waves, Kelvin wave ($m = -1$), Yanai wave (mixed Rossby gravity wave, $m = 0$) and planetary waves are labelled in the figure.

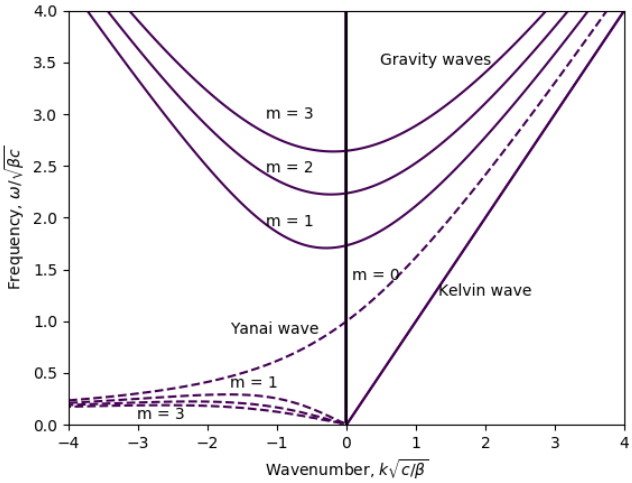

Fig. B.1 Dispersion curves for equatorial waves for $m = 0, 1, 2, 3$, as a function of non-dimensional wavenumber and wave frequency. The curve for eastward propagating Kelvin wave (needs to set $m = -1$).

B.2 Application of equatorial wave theory

To detect different equatorial wave modes in reanalysis and model data, 2 Dimensional (2-D) Fourier Transform is applied. Here, both the power spectra and coherence spectra are computed to better describe wave features. Following the spectral analysis (Hendon and Wheeler 2008; Kiladis et al. 2009), the time-longitude domain of the fields, e.g., $v(t_n, x_m)$ and $u(t_n, x_m)$ at

one latitude, is mapped to wave frequency and wave number domain, where the t_n and x_m indicate N equally spaced time points and M equally spaced points along a latitude. The 2-D Fourier transforms for the $u(t_n, x_m)$ and $v(t_n, x_m)$ are

$$\mathrm{U}(\omega, \mathrm{k}) = \frac{1}{\mathrm{N}} \sum_{n=1}^{N} \frac{1}{M} \sum_{m=1}^{M} u(t_n, x_m) \exp[-i(\omega t_n - k x_m)],$$

$$\mathrm{V}(\omega, \mathrm{k}) = \frac{1}{\mathrm{N}} \sum_{n=1}^{N} \frac{1}{M} \sum_{m=1}^{M} v(t_n, x_m) \exp[-i(\omega t_n - k x_m)].$$

Here the ω and k are wave number and frequency. Then, the spectral power could be derived as

$$\mathrm{Upower}(\omega, \mathrm{k}) = U(\omega, k) * conjugate(U(\omega, k)),$$

$$\mathrm{Vpower}(\omega, \mathrm{k}) = V(\omega, k) * conjugate(V(\omega, k)).$$

Then, the cross spectra of $\overline{u'v'}$ is formulated as

$$\mathrm{UV}(\omega, \mathrm{k}) = Real[U(\omega, k) * conjugate(V(\omega, k)].$$

Acknowledgements

I would like to express great thanks to my supervisor, Prof. Dr. Peter Braesicke, for allowing me to work in KIT-IMK-ASF. I appreciate his expert suggestions on research topics and thesis structures, and also support for my three-month extension. He is quite open-minded and his door is always open for me whenever I am in trouble.

Thank you Jennifer Schröter for her help on ICON-ART. She is very patient and always replies to my questions in detail. Her code development of the Linoz scheme also made my research possible.

In addition, many thanks to Tobias Kerzenmacher who read and corrected my thesis one chapter by one chapter. Without his help this dissertation would not be possible. Thanks to Johannes Eckstein and Christopher Diekmann for sharing the Python scripts. I would thank to officemates of IMK-ASF for countless supports and cares.

Thank you to my flatmates, Chengwu Yang, Donghui Cheng and Wensheng Yan for sharing their wisdom about life and academic research. I'll always remember many nights of beers and football games. Life would be quite boring if they were not around.

Thanks to the Chinese Scholarship Council (CSC) for funding my research in KIT and Steinbuch Centre for Computing (SCC) for providing high computational resources (IC2, FH2 and UC1).

Finally, I would like to thank my parents. They brought me to this world and encouraged me to overcome difficulties one by one. Life is always hard, but I'll *calm down and carry on* for they are supporting me always.